Chemical modification of two-dimensional materials

Chemische Modifikation von zwei-dimensionalen Materialien

Der Naturwissenschaftlichen Fakultät

der Friedrich-Alexander-Universität Erlangen-Nürnberg

zur

Erlangung des Doktorgrades Dr. rer. nat.

vorgelegt von

Florian Späth

aus Furth im Wald

Als Dissertation genehmigt von der Naturwissenschaftlichen Fakultät der Friedrich-Alexander-Universität Erlangen-Nürnberg

Tag der mündlichen Prüfung: 30.10.2018

Vorsitzender des Pormotionsorgans:	**Prof. Dr. Georg Kreimer**
Gutachter:	**Prof. Dr. Hans-Peter Steinrück**
	Prof. Dr. Andreas Görling

Content

1 Introduction

The electronic devices, which we currently use, will be very different from the ones we use in the future. Higher computing power, lower power consumption as well as flexible displays and electronics are projected. To achieve this change to flexible and more efficient devices, they will likely be produced from two-dimensional (2D) materials, as, e.g., flexible and transparent electrodes, instead of e.g. the brittle indium tin oxide[1,2]. The use of novel 2D materials might also allow for a higher power density or faster charging batteries in future devices. Nowadays, 2D materials are studied on a fundamental basis towards their growth and their basic chemical and physical properties, yielding results that were not possible with 3D bulk materials[2–4]. The intense research on the new class of 2D materials was sparked by the discovery of graphene by Geim and Novoselev[5], which was awarded with the Nobel-prize for physics. The research into graphene[6] led to a myriad of new physical properties. These were previously only predicted by theory, and the synthesis of free standing 2D materials was proposed to be impossible[7,8]. The case of graphene has shown that these materials are not instable, but rather inert and mechanically highly durable[9–12], with highly interesting properties such as high electron mobilities and half-integer quantum hall effect[7,13]. The successful fundamental research on graphene led to a massive effort into the study of further 2D materials. One example is hexagonal boron-nitride (h-BN): just as graphite, bulk h-BN was already widely used as lubricant; it is a stacked bulk crystal, but non-conductive and temperature stable[14,15]. The research effort into this material, so-called “white graphene”[16], especially into the 2D nature of h-BN is increasing and is part of possible 2D materials to allow for future devices.

Today, around 700 2D materials have already been synthesized or predicted to be stable by ab-initio calculations[17,18]. However, their functionalization, in order to tune the properties of a 2D material is still challenging[9]. The reason for this is twofold: 2D materials, especially graphene and h-BN, are large 2D crystals with π-systems extending over the whole lattice and cannot be brought into solution in their pristine, i.e. often desired form[9]. This is due to the large π-systems that favors π-π stacking, leading to strong van der Walls interactions, and due to their immense size. Harsh methods have to be applied to bring, e.g. graphene into solution, starting from the breakup of large flakes into smaller ones, and subsequently the treatment according to e.g. the Hummers' method[19].

However, the need to functionalize 2D Materials is manifold. For wet-chemistry, it is required to bring the 2D materials in solution for further reactions and for tuning of the properties, towards desired features. Functionalization, mostly with oxygen containing functional groups is a starting point for further reactions. Graphene is a zero-bandgap semi-metal[20]. However, if it were to be used in semiconducting applications, as a replacement for silicon, a band-gap needs to be opened, so that transistors based on graphene can be built, which show lower power consumption. Chemical functionalization or the introduction of defects offers the possibility to tune the bandgap and the carrier concentration of a 2D material. Notably, also other interesting properties can be engineered by chemical functionalization of 2D materials: tuning the sensitivity for the detection of gas molecules[21], or even the type of molecule, for gas-separation[22] and magnetic moieties for spintronic applications[23]. Also the possibilities, which arise from specifically introduced defects, are intriguing as they allow for the fabrication of graphene nano-ribbons[24,25], gas-separation, and even for isotope separation[26–28]. Moreover, attachment of defined chemical anchoring groups allows for changing of the adhesion properties on a surface and tuning the interaction with other chemicals or electronic contacts becomes a possibility.

In the following, a short overview over current functionalization achievements is presented: For graphene, already numerous examples exist in literature. For a wet chemical approach, one can distinguish between the applied starting materials. When using graphite, one can intercalate graphite with alkali metals. Thereby, one increases the interlayer distance, forming a graphite intercalation compound, and dopes the graphene layers, facilitating a reaction. This intercalation compound, dissolved in 1,2-dimethoxyethane and reacted with 1-iodohexane, results in alkylated graphene layers[29].

Such graphite intercalation compounds can also react, e.g. with diazonium salts, producing also functionalized graphene layers[30]. However, a major drawback of these reactions is the low degree of functionalization achieved, not exceeding 2%. Another possibility that starts from graphite is the so called Hummers' method[19]. Hummers' method introduces many different oxygen functionalities to graphite, e.g. ester, epoxy or acid groups. This leads to a solution of the exfoliated, but oxidized, single layers of graphene, so called graphene oxide, although the flake size is strongly reduced. Graphene oxide lost the π-conjugated backbone of graphene, and thus many of the interesting properties of graphene[19]. It is possible to subsequently also defunctionalize graphene oxide[31] in an aqueous workup. However, the small size of the flakes remains, while functional groups introduced via Hummers' method desorb. Moreover, the edges of the flakes will always remain defects. Also loss of carbon may occur, depending on the workup procedure[31–33].

When using with graphene oxide as a starting material, numerous different ways of functionalization have already been reported, as the present oxygen functional groups can readily be used to further functionalize this material: Graphene oxide functionalized with poly(3-hexylthiophene) bonded to the carboxylic groups of graphene oxide was used in solar cells[34]. Amines also readily react with the oxygen groups in graphene oxide, allowing for nitrogen-containing functional groups[35]. An interesting functionalization offers cross-linking of the high-surface area graphene oxide sheets. This results in the formation of aerogels. These light-weight, highly porous foams are promising candidates for gas adsorption[36]. A problem of this class of functionalization is that the oxygen functional groups of graphene oxide can only be tediously removed, without the removal of the added functional groups.

When using reduced graphene oxide as a starting material for functionalization, the large number of reactive defects results in a rich chemistry. Functionalization with aryl diazonium salts is reported, with a wide range of end-groups[37]. Functionalization, which allows for carbine chemistry and thus addition of metal complexes enables the production of photoactive graphene[38].

For h-BN, the wet-chemical functionalization is not well studied. However, it was demonstrated that, like for graphene and graphene oxide, defects are centers of reactivity. This was shown when h-BN with different defect concentrations was reacted with octadecylamine. Here, the more defects h-BN has, the higher the yield of reacted h-BN[39].

Lastly, a short overview of supported graphene and h-BN functionalization, i.e. reactions of the 2D material without the use of solvents, is given. This also serves to provide an insight to the state of the art of the research in the topic of this thesis. For graphene, particularly the fluorination is well investigated. Different fluorination methods are available. One is to expose graphene/h-BN to XeF_2, or reactive ion etching, with e.g. SF_6 as fluorination agent[40,41]. For single-sided fluorinated graphene a maximum fluorine coverage of C_4F is expected on Cu(111)[40]. In contrast, for free-standing graphene, a CF stoichiometry is reported[40]. Besides fluorination also hydrogenation was studied. Here atomic hydrogen and hydrogen plasma are routinely used[42,43]. For free-standing graphene a CH stoichiometry was observed, while C_2H was found on Ni(111)[42] and C_4H on graphene on Au(111)[44]. Lastly, also the functionalization on substrates in vacuum with larger molecules has already been achieved for graphene. The functionalization with 4-nitrophenyl diazonium tetrafluoroborate was shown. Here, an amorphous adlayer is formed on graphene, which can be desorbed using a STM tip, paving the way for nanostructured functionalization[45]. Moreover, the functionalization of graphene with amino- and cyano-group containing molecules was achieved. Just as hydrogen atoms are radicals and thus readily react, radicals from acetonitrile ($\bullet CH_2CN$) formed by homolytic scission lead to the attachment to graphene, in this case to the Moiré pattern of graphene on Ru(0001)[46,47]. Para-aminophenol molecules react selectively with intentionally created single atom vacancies in graphene[48]. Lastly, the methylation of graphene on SiC(0001) using a two-step process should be mentioned. Graphene was first chlorinated with molecular chlorine, and subsequently methylated via a Grignard reaction using methylmagnesiumbromide (CH_3MgBr)[49].

The general advantage of functionalization of 2D materials without the use of a solvent is that no impurities are adsorbed during transfer or little defects are introduced. A major drawback is that the production and functionalization methods often are not applicable to gram-scale fabrication, or result in little functionalization.

In this work, a different approach that circumvents the challenge to bring the 2D material in solution is chosen. The 2D material is directly prepared on a suitable catalyst that is a transition metal single crystal. Thus a route is chosen that chemists call "one pot" approach. This means that the 2D material remains on the same substrate for all reaction-, functionalization- modification- and all characterization-steps. The pristine substrate is the starting point for the preparation of the 2D material in this thesis. Novel functionalization and intercalation methods are developed to achieve the modification of the system graphene adsorbed on a Ni(111) crystal and h-BN adsorbed on a Ni(111) crystal. Moreover, the thermal stability of the chemical functionalization is probed and testing towards the applicability for real devices.

In the following, in Chapter 2.1 the physical properties of graphene and hexagonal boron-nitride on different substrates, but especially Ni(111), will be discussed. This includes the preparation of both 2D materials and a discussion of the band structure of free standing graphene and graphene and h-BN adsorbed on Ni(111). Moreover, the need for an ultra-high vacuum approach is eluded, both for the functionalization route chosen and the spectroscopic methods. Next, in Chapter 2.2, a short introduction to a synchrotron facility is given, as highly brilliant soft X-rays are used through this thesis. Subsequently, Photoelectron spectroscopy and near edge X-ray absorption fine structure (NEXAFS) are explained in detail, followed by temperature programmed desorption spectrometry and the basic principles of a super-sonic molecular beam. Lastly in Chapter 2.7, the experimental setups are shortly described.

In this thesis, the functionalization of graphene and h-BN with small molecules and radical atomic species on Ni(111) was studied. The following chapters are written such that they can be read independently.

In Chapter 3, the interaction of nitrogen-doped graphene with atomic hydrogen is eluded. For doped graphene, it is observed that hydrogen binds to the carbon back-bone of graphene as if it were pristine. It exhibits a hydrogen coverage-dependent desorption mechanism, resulting in two desorption maxima, for high hydrogen coverages and for low hydrogen coverages. Depending on the nature of the nitrogen species in the graphene lattice distinctively different reaction mechanisms are observed.

In Chapter 4, the interaction of atomic hydrogen with h-BN is investigated. h-BN binds hydrogen at small exposures, and intercalates hydrogen at high exposures, thus showing a different reactivity compared to graphene, where intercalation was not observed.

In next chapters, the reactivity of h-BN towards molecular oxygen was investigated. The results are separately shown in the two Chapters 5 and 6, for low and high substrate temperatures, respectively, as the occurring reactions are strongly, depending on the substrate temperature. It is observed that not the exposure but rather the substrate temperature plays a critical role for the reaction pathway. For the substrate at room temperature, a bonding of molecular oxygen to the h-BN back-bone is found. For higher substrate temperatures of ~ 440 K, mainly the intercalation of h-BN with atomic oxygen is observed, while for even higher substrate temperatures of 600 K oxidation is found. For oxidation, different boron oxide species are found.

In Chapter 7 the co-adsorption of atomic hydrogen and molecular oxygen on h-BN is investigated. This became only possible due to the deep insights into the h-BN adsorption systems gained in the previous three chapters. Both adsorbates can react with the other during adsorption and desorb. This is a large step forward to band-gap tuning, exact doping and the use of 2D materials as potential metal-free catalysts.

In the Chapter 8, a more complicated functionalization is realized. Here h-BN and graphene are exposed to highly energetic methyliodine. A bonding of CH_3-groups and a subsequent thermally induced reaction is observed. For h-BN, the reaction-pathway is eluded in great detail.

As a last result, the intercalation of argon underneath graphene is studied in Chapter 9. This was made possible, by pre-implanting argon in the substrate before the growth of graphene. Argon intercalation leads to quasi-free-standing graphene usually realized through the intercalation of gold or other materials with a suited band structure.

In Chapter 10 and 11, the results of this thesis are shortly summarized in English and German, respectively.

2 Fundamentals techniques and setups

This chapter will introduce the fundamentals of the systems studied as well as the techniques and the setups used. Chapter 2.1 will discuss the growth and properties of the 2D materials graphene and h-BN in detail. The subsequent chapters will focus on the techniques and their principles. The basic operation principle of a modern 3rd generation synchrotron is explained briefly in Chapter 2.2, as the spectroscopic methods rely on tunable, highly intense soft X-ray radiation. Then, in Chapter 2.3 X-ray photoelectron spectroscopy, the main method used in this thesis, is described. Here, first the fundamental steps of the photoemission process are discussed, and subsequently the origin of binding energy shifts. In Chapter 2.4, the fundamentals of near edge X-ray fine structure spectroscopy are presented. In particular, the difference between absorption of σ* and π* orbitals is explained, and how NEXAFS is applied to gain insight into the interaction of a 2D material with its support. As a last spectrometric method, temperature programmed desorption is shortly explained in Chapter 2.5. In Chapter 2.6, the basic principle of a supersonic molecular beam (SSMB) is introduced that allows for tuning the kinetic energy of gas phase species. The SSMB was mainly applied to allow studying for activated adsorption processes and rapid growth of graphene. Lastly, in Chapter 2.7 the two experimental setups used in this thesis are described in detail.

2.1 Growth and properties of graphene and hexagonal boron-nitride on Ni(111).

Both graphene and hexagonal Boron-Nitride grown on transition metal substrates are well studied with surface science techniques and ab-initio calculations[6,50–52]. The growth of these 2D materials is generally accomplished by chemical vapor deposition[53]: On a hot metal substrate, an appropriate precursor containing the right type of atoms is dosed, either under vacuum conditions or under inert atmosphere. Depending on the transition metal, the atoms are then either dissolved into the bulk, or directly assemble on the surface to form the 2D material[54–58]. For graphene on Ni(111), both mechanisms seem to be present, depending on the carbon concentration in the bulk[58]. For graphene on Cu(111), only the decomposition on the surface is relevant, while on Pd(111) carbon segregation from the bulk is the growth mechanism[57,59]. A stick and ball scheme of graphene (left) and h-BN (right) is shown in Figure 2.1.

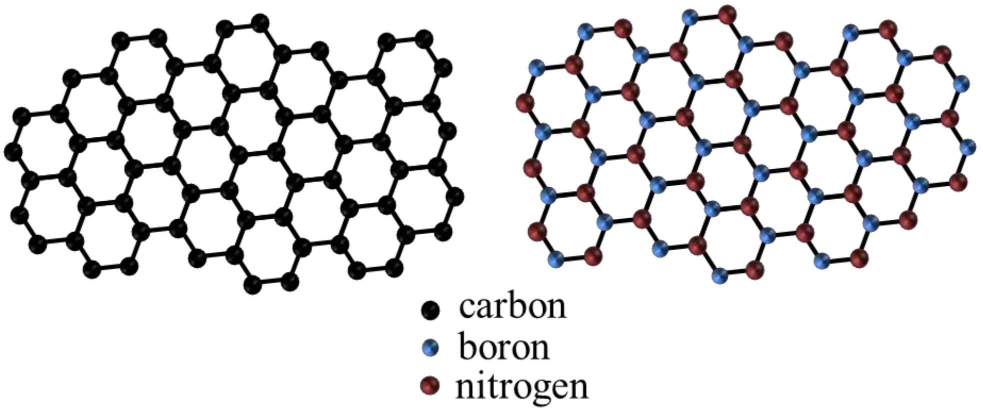

Figure 2.1 schematic stick and ball model of free standing graphene (left) and h-BN (right)

To grow both materials on Ni(111) either only carbon-containing precursors (e.g. propene or ethene) are used to obtain graphene, or precursors, which contain boron and nitrogen (ammonia borane or borazine) are used to obtain h-BN[50,52]. In both cases no dependence of the layer quality on the precursor chemical was observed. Generally, the precursor is exposed to the hot substrate. For graphene a substrate temperature of 900 K and a precursor pressure of $\sim 2*10^{-6}$ mbar are applied. Depending on the state of the crystal, exposures from 2000 to 30000 L are needed, showing the significance of dissolved carbon in the Ni(111) crystal. The preparation of h-BN requires higher substrate temperatures of 1050 K but lower pressures of only $\sim 5*10^{-9}$ mbar. The layers typically saturate after an exposure of ~20 L, pointing to the fact that dissolution of the precursor molecules is not important and a decomposition pathway is dominating. For both 2D materials, graphene and h-BN, the growth is self-terminating under these conditions, leading always to a single, closed layer, with a low defect density.

The interaction of the 2D material with the transition metal, which acts as the catalyst for their growth, influences the band-structure and the adsorption geometry[51,60–62]. This influence is well understood and investigated. Thus, further changes due to chemical modification of the 2D material can easily be distinguished. The change of the electronic structure (band structure) of the 2D material upon adsorption on a metal substrate is generally as following: A hybridization of the bands of the 2D material with the valence bands of the support occurs. Bands of the 2D material may shift in energy, as electrons are transferred from the substrate to the 2D material or vice versa.

In a simplified picture, strong hybridization, as found for graphene with Ni(111), and weak hybridization, as observed for graphene on Pt(111) and Cu(111), can be distinguished. The type of hybridization is dependent on the position of the d-band center of the support relative to the 2D material. For a position of the d-band center of the substrate from 0.6 to 1.8 eV, relative to the Fermi edge, strong hybridization with graphene is observed, while from 1.8 to 4.2 eV (Ag) weak hybridization is observed[57]. The former is understood as chemisorption and the latter as physisorption. This is also reflected in the adsorption distance of the 2D material. Chemisorption has a small adsorption distance of roughly 2 Å, while physisorption a large adsorption distance of roughly 3 Å for graphene[57]. An additional effect upon adsorption of the 2D material on a metallic surface is the so called pillow effect, which has the largest influence for chemisorbed 2D materials. The pillow effect results in a shift of the bands of the 2D material towards lower binding energies. Here the potential of the surface dipole is pushed away by the potential of the adsorbing 2D material, resulting in a band shift[63].

The second change, from its free-standing form, upon adsorption on the support can be a deviation from its flat character. On, e.g. Ir(111), Rh(111) and Ru(0001) a lattice mismatch between the 2D materials h-BN and graphene and the metal support exists. Due to this mismatch, a Moiré-pattern forms, which is best described by a regular valley and mountain landscape[64–70]. For h-BN on Rh(111), one even finds the formation of steep walls, which are best described as pores and wires. The valleys (pores) show strong interaction with the substrate, while the mountains (wires) show less interaction with the substrate.

For graphene, the adsorption geometry on Ni(111) was investigated in detail by Zhao et al. Two stable adsorption geometries were found both with photoelectron spectroscopy and density functional theory (DFT)[50]. In X-ray photoelectron spectroscopy (XPS), these two adsorption geometries are well-resolvable, as one single C 1s peak for the bridge-top geometry and two split C 1s peaks for the top-fcc geometry. A mixture of both is always observed, as the two geometries have nearly the same adsorption energy. For h-BN, a similar distribution is expected. The electronic structure of the two systems was already studied in detail with angle resolved photoelectron spectroscopy (ARPES)[51,60]. Here, the strong interaction between the 2D material and the substrate, and the resulting change in its band structure, is clearly observable for graphene. To understand the impact of the interaction, the band structure of graphene in its free-standing form, i.e. without support is discussed here briefly.

The band structure of graphene had been calculated already for the π-electrons using a tight binding ansatz by P. R. Wallace in 1947 by hand[20]. It was observed that so-called Dirac cones emerge at the K-points of the Brillouine zone. These Dirac-cones are a linear dispersion of the electronic band structure, from which graphene's high carrier mobility originates[71].

For free-standing graphene, the Dirac-cones result in the following properties: At the Fermi edge of the Brillouin zone no charge density is observed, making free-standing graphene a zero-gap semimetal, with the conduction and valence bands only touching at six single points in the first Brillouin zone. Moreover, as the bands have to be calculated with the 2D Dirac-equation, the electrons in the valence band close to the Dirac-point behave as massless fermions[72]. Due to this behavior, charge carriers may obtain velocities up to 185,000 $cm^2\ V^{-1}\ s^{-1}$, leading to so called ballistic transport[73,74]. This extraordinary high mobility is the reason, why graphene is still a strong contender for the replacement of silicon in semiconducting applications, as it would allow for much faster switching transistors, and thus substantially higher computing power. However, the lacking bandgap is still a problem[75].

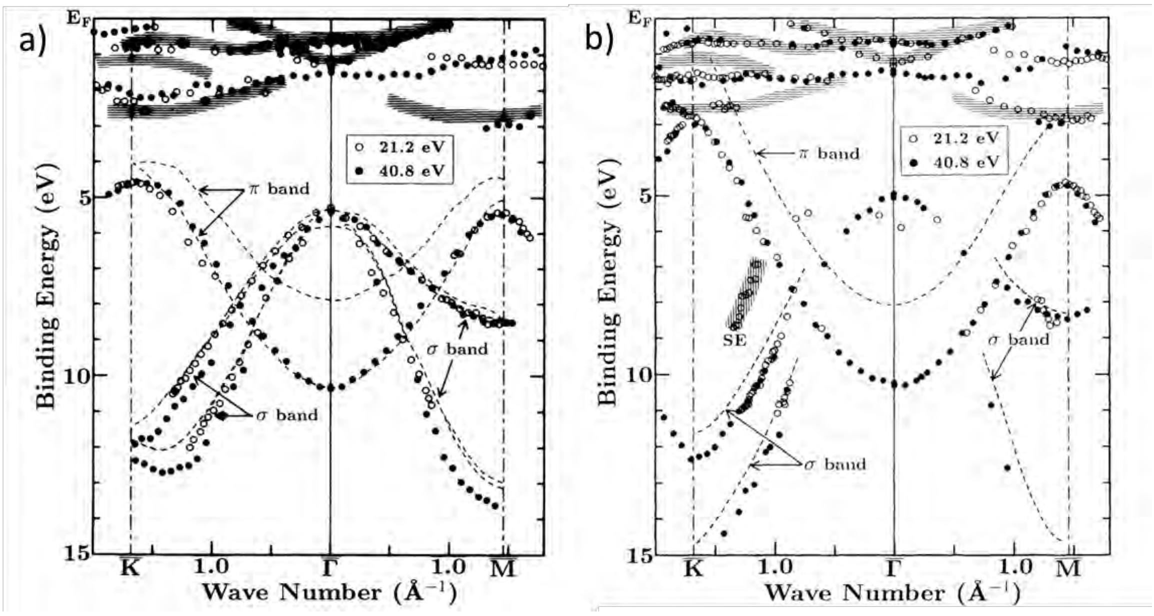

Figure 2.2 (a) Band structure of the h-BN/Ni(111) system. Solid and hollow dots represent the excitation energy. Dashed lines represent theoretical calculations. Shaded lines are the Ni 3d states. (b) Band structure of the graphene/Ni(111) system. Dashed lines represent the band structure of graphite [76]*.*

Once adsorbed on a Ni(111) surface, the band structure of both 2D materials changes drastically, as the valence bands hybridize with the Ni(111) valence states. ARPES measurements have shown this for graphene[62,77]. Upon adsorption of graphene on Ni(111), the hybridization leads to the formation of a band-gap and the linear dispersion at the K-point, i.e. the Dirac cone, is no longer present. This is shown in Figure 2.2b. The π-band of graphite is located at 8 eV at the Γ point and in the measurement it is found at lower binding energy by up to 2 eV. At the K-point, no linear dispersion is observed and the π-band hybridized with the Ni 3d states, resulting in an energy difference of nearly 3 eV. The σ-bands are also shifted towards lower binding energy by several eV.

Replacing carbon with boron and nitrogen, to from the isoelectronic and isostructural h-BN, yields a very different electronic structure. This means that the honeycomb structure is still present and the lattice constant is nearly identical[23,51], but due to the ionic character of the boron – nitrogen bond h-BN shows an indirect bandgap of ~6 eV as a bulk material[78]. Thus, also the band-dispersion for h-BN is much smaller than for graphene, due to the non-covalent character of the h-BN bonds, compared to the fully covalent carbon-carbon bond in graphene. For a free-standing 2D material, the charge carriers do not behave as massless Dirac fermions, but as electrons interacting with each other and the crystal, as described by the Schrödinger equation. h-BN has no bands close to the Ni(111) valence states and thus ARPES experiments show that the changes to its valence bands are more subtle than in the case of graphene[60]. The band-structure for h-BN adsorbed on Ni(111) is shown in Figure 2.2a. At the K-point an energy difference between the h-BN π-band and the Ni 3d states of about 2 eV (Ni 3d at 3 eV, h-BN at 5 eV) is observed, but a difference to the calculated band-structure shown with dashed lines is nevertheless found, and thus hybridization occurs. This is also evidenced by the formation of so-called interlayer states. These states are a hybridization of the empty π*-orbitals of h-BN and the Ni 3d valence bands[62]. Ultraviolet photoemission spectra recorded in a non-angular dependent way, also indicate that upon adsorption h-BN interactions with the Ni 3d bands[62].

To conclude, the adsorption of graphene and h-BN change their respective electronic structure, in obvious ways for graphene, and more subtle ways for h-BN. Thus also the chemical properties change quite drastically. On the one side, this can be exploited, as an activation of the 2D material facilitated by this strong support interaction. The 2D material may, upon functionalization saturate its free valence (a dangling bond) at the substrate atoms, and therefore interact even stronger with the support. The interaction with the support thus also dictates the degree of achievable functionalization. This was proven e.g. with graphene adsorbed on Ni(111) and on Au(111), where Ni(111) as substrate allows for a much higher degree of hydrogen bonding, as a stronger interaction is possible. While one atom of the unit cell binds to hydrogen, the second carbon atom in the unit cell binds to the surface, which is not observed for graphene on Au/Ni(111)[42,44]. On the other side, strong interaction with the substrate may hinder intercalation, i.e. the insertion of atoms or molecules between the 2D material and the substrate[79–81]. Thus the reaction pathway - intercalation or functionalization – is dependent on the 2D material - substrate interaction.

2.2 Synchrotron-based radiation.

As two of the three applied characterization methods rely on monochromatic, tunable soft X-ray radiation the fundamentals of synchrotron radiation are discussed shortly. A synchrotron is a particle accelerator facility, operated with electrons or positrons, which uses the principle that accelerated charged particles emit light[82]. Electrons are generated usually through thermal emission, They are subsequently accelerated by a microtron. Then, they are transferred into a booster ring. In the booster ring, they are accelerated up to the desired energies, in the GeV region (1.7 GeV for BESSY II). Subsequently, they are injected into the storage ring. In the storage ring, so called bending magnets are used to keep the charged particles on a polygonal trajectory, with insertion devices (wigglers and undulators) on the straight parts. A schematic view of BESSY II of the Helmholtz-Zentrum Berlin, where the photoemission data in this thesis was gathered, is shown in Figure 2.3.

In the booster ring, the strength of the magnetic field can be varied, so that the radius of the round trajectory is constant, while the kinetic energy of the electrons increases. This synchronous change in particle energy and magnetic field strength gave the synchrotron its name. Nowadays the name synchrotron is synonymous with a storage ring facility. Once the electrons are injected in the storage ring, their speed is kept constant, close to the speed of light, with the help of radio frequency cavities, to compensate for the energy they have lost as radiation. These losses are fractions of their energy and occur, at bending magnets, which induce a turn of the electrons keeping them on their polygonal trajectory and at so called wigglers and undulators[83], also called insertion devices (IDs). The resulting radiation from bending magnets is often used for experiments as a by-product of the synchrotron operation; however, the intensity of the radiation is low, compared to insertion devices. These IDs are periodically alternating poles of magnets in rows above and below the electrons path, deflecting the electrons onto sine-shaped trajectories. While passing each magnet of the insertion device, the electron is accelerated, and thus light is emitted. In the case of the undulator, the emitted light interferes constructively, leading to a further increase in emitted intensity. To vary the wavelength of the emitted light, the distance between the magnets above and below the electron containing vacuum is changed[84]. Insertion devices emit light in a narrow spectral range of several electron volts, with multiple higher harmonics. To select the desired wavelength and to obtain a better energy resolution, a monochromator is added downstream before the experiment.

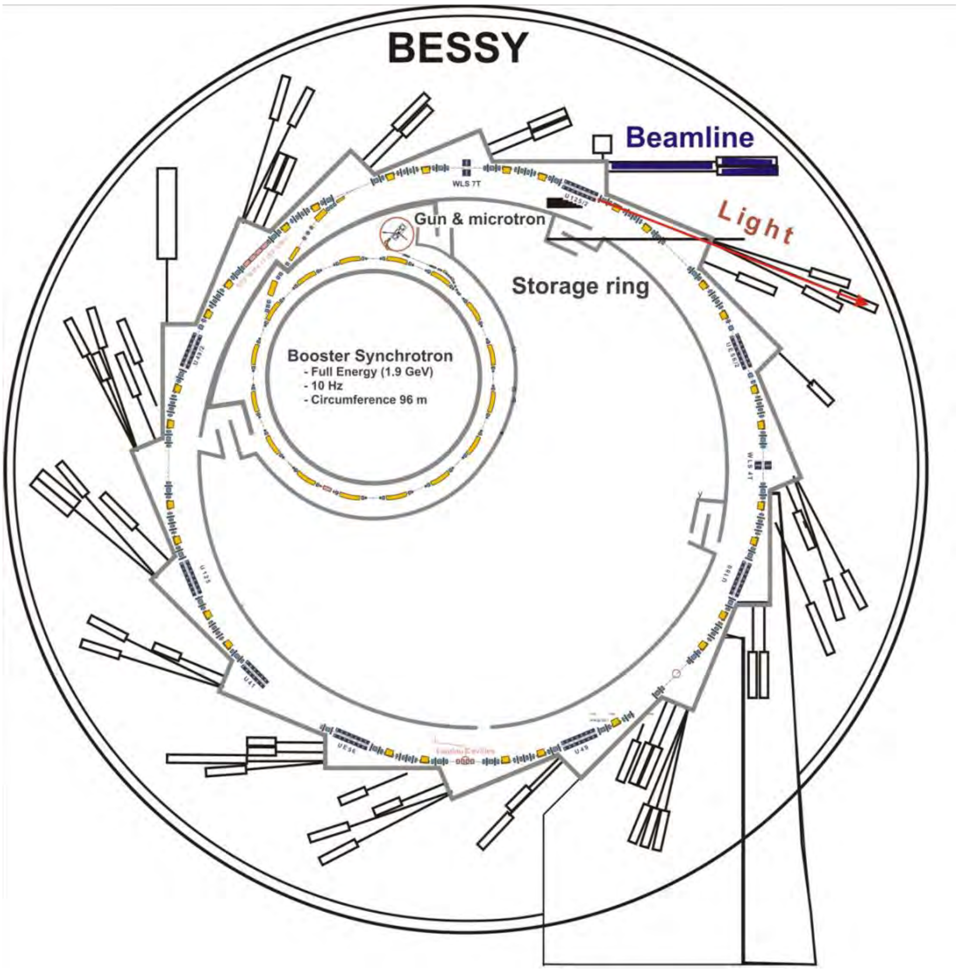

Figure 2.3 Schematic view of BESSY II[85].

2.3 Photoelectron spectroscopy

The main method used in this thesis is photoelectron spectroscopy, which is outlined in the flowing chapter. Besides some theoretical aspects, also data treatment is shortly discussed.

The emission of photoelectrons, when shining light of a sufficiently small wavelength, onto matter was fist observed by Hertz[86]. The phenomenon was further explained by

Einstein. For this description, he was awarded the Nobel Prize in 1921. For his efforts in developing XPS further, Kai Siegbahn was also awarded with a Nobel Prize in 1981. As a distinction between the used photoelectron spectroscopic methods, the wavelength of the light is used. This leads to the terms XPS (X-ray photoelectron spectroscopy) when using X-rays and UPS (ultraviolet photoelectron spectroscopy) when using ultra-violet radiation. UPS typically uses excitation energies from 2 to 100 eV to probe the valence states that are roughly 0 to 25 eV below the Fermi level. XPS is measured with a photon energies up to 2000 eV, probing the deeper lying core levels[87]. Above 2000 eV, the technique is called HXPES (hard X-ray photoelectron spectroscopy) and applied to probe bulk properties. These excitation energies and the probed energy levels however only serve as a general rule[88].

For UPS, synchrotron radiation, helium discharge lamps and frequency-multiplied lasers are commonly applied as light sources. For XPS, lab based X-ray anodes and synchrotrons are used.

UPS is applied to probe the valence band structure of a material, or the valence orbitals of an adsorbate system. If performed in an angle resolved fashion (angle resolved UPS or ARUPS) these experiments are the only possible way, to draw conclusions on the band structure. Furthermore, the adsorption geometry of molecules can be determined using symmetry selection rules[89].

XPS has become a wide-spread analysis method. It is element-specific and offers a high sensitivity for the chemical surrounding of the probed element, and is surface sensitive.

A typical XP spectrum of h-BN adsorbed on Ni(111) is shown in Figure 2.4. The amount of emitted electrons is given as intensity on the y-axis, in arbitrary units. On the x-axis the binding energy is given. As a convention, the lowest binding energy is on the right side. Besides XP peaks, also peaks originating from Auger processes may be observed. These are easily identified by changing the photon energy, as their kinetic energy is constant, while for XP peaks the binding energy is constant. In the following the photoemission is described in detail.

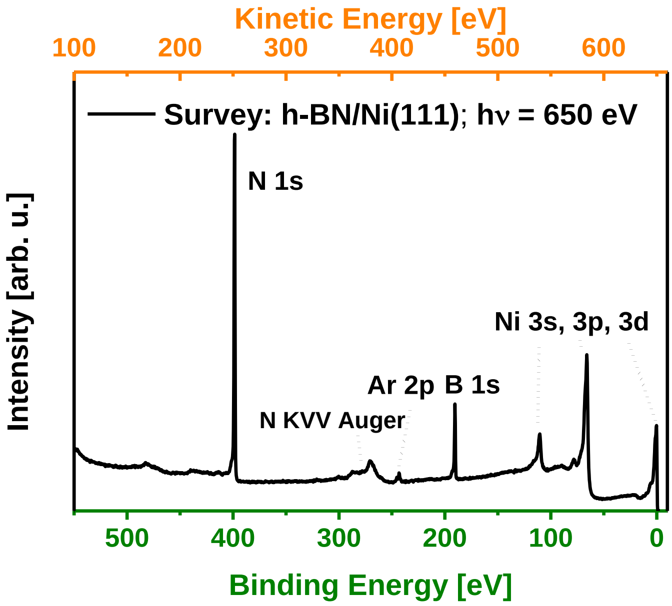

Figure 2.4 XP Spectrum of h-BN adsorbed on Ni(111), with minor amounts of argon intercalated. The observed XP and Auger peaks are denoted.

The elemental steps of XPS are the following: Upon irradiation of matter with photons of sufficient energy (i.e. X-rays) electrons are emitted from an atom. The electrons travel through the solid to the surface. During their path through matter the electrons may lose energy due to interactions. Thereby, they do not contribute the primary XPS peak anymore but become a part of the secondary electrons that are the background of the spectrum. These interactions with matter also lead to the surface sensitivity of photoemission spectroscopy. The surface sensitivity is dictated by the inelastic mean free path in the probed matter and their respective energy. A minimum of the mean free path is found in the range from 70 to 100 eV electron kinetic energy, and thus maximum surface sensitivity is observed in this energy range window[90]. From the surface the electrons escape into vacuum. Energy conservation upon photoexcitation has to be taken into account and the kinetic energy of the emitted electrons can thus be described in the following expression:

$$E_{kin} = h\nu - E_B - \Phi$$

$h\nu$ equals the energy of the incoming radiation. It equals the kinetic energy of the emitted electron (E_{kin}), reduced by the binding energy (E_B) of the electron in the atom and the work function (Φ) of the sample, which has to be overcome, in order to achieve emission into the vacuum. Now, the problem arises that the work function of a sample is unknown and would have to be determined separately. Furthermore, it may change with adsorption of e.g. molecules or metals onto the sample surface. Thus both E_{kin} and E_B are affected by the unknown variable Φ. For solid, conducting samples this is solved by electrically connecting the conducting sample and the electron analyzer. This leads to the alignment of their Fermi energies. Thus the work function changes to the known and constant work function of the analyzer Φ_A, and thus, E_B is measured. Thus the equation above changes to:

$$E_{kin} = h\nu - E_B - \Phi_A$$

During the emission of the electron, the core hole that the emitted electron leaves behind decays. The lifetime of the core hole affects the width of the energy of the emitted electron according to the uncertainty principle[91]. A schematic description of the photoemission process is given in Figure 2.5.

The element-specific binding energy of the photoemission is described with Moseley's law for the 1s core levels. However, many other, smaller effects may also influence the observed binding energy. These are generally summarized under the term chemical shift. The chemical shift consists of initial and final state effects. The initial state is present prior to irradiation, while the final state is present only after the photoemission process in the ionized atom[92].

Initial state effects are: a change of the charge density of a probed molecule through e.g. oxidation, thus removing electron density from the probed atom. In a simple picture, the more oxidized a probed atom becomes, i.e. the more electron deficient it becomes, the stronger its remaining electrons are bonded. The charges of the nucleus are less shielded, and thus the higher the binding energy of the electrons in that core level becomes. This initial state effect has a large influence on binding energy of up to ~8 eV[92]. Smaller shifts may arise, e.g. form different adsorption geometries[50].

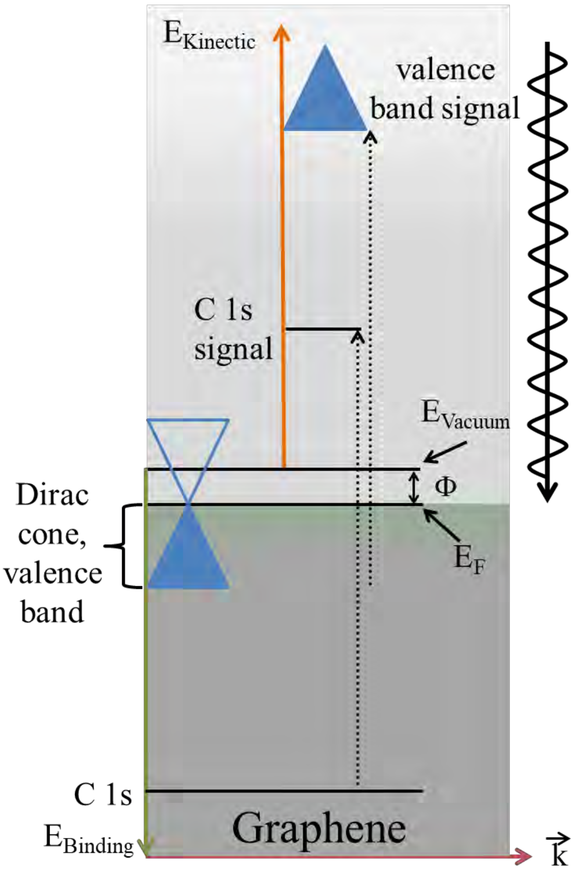

Figure 2.5 Schematic depiction of the energy scheme of the photoemission process. Graphene, only containing carbon, and displaying a Dirac cone at the Fermi-level is used as an example.

Typical examples for final states are the excitation of further electrons in higher shells upon emission of the photoelectron electrons. These losses are called shake up satellites, if the electron excites further electrons into excited states or if it excites other electrons into vacuum shake off satellite[91]. Besides these two effects also screening of the core hole left back by the photoelectron can change its kinetic energy. Large differences of several eV binding energy between organic molecules in direct contact with a metal substrate to the same molecules in the gas phase are observed. The core hole is well shielded for the adsorbed molecule, through the electrons of the substrate, resulting in a higher kinetic energy, and thus lower binding energy. For the molecule in the gas phase, the opposite is observed.

However, these above described effects are not easily discernable and often occur simultaneously. Thus, often reference measurements and data from multiple core levels and the establishment of models are needed for a successful characterization.

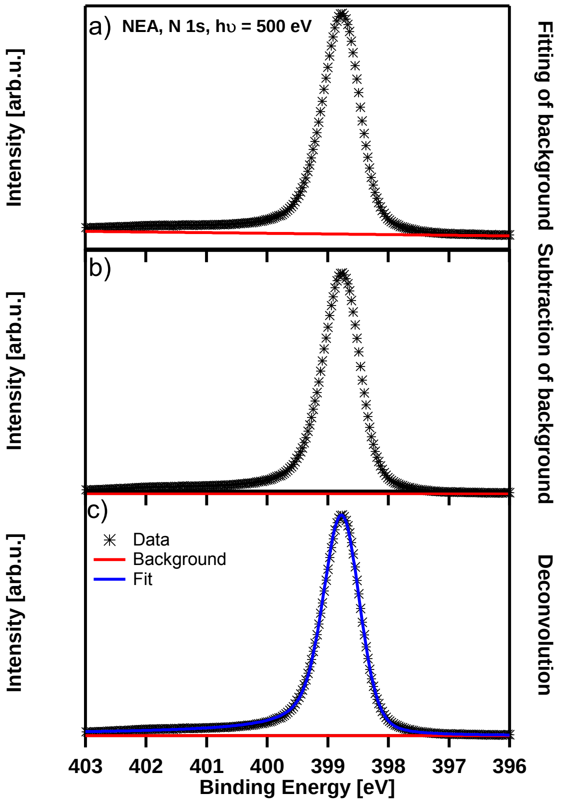

Figure 2.6 (a) XP-spectrum of h-BN in the N 1s core level. Black stars are the measured data points. Red line is the fitted background with a linear function. (b) the spectrum after subtraction of the background. (c) fitted spectrum, with the corresponding asymmetric peak.

In the following, the XP data treatment is discussed. First, some theoretical considerations are given, and then the applied methods are discussed.

To understand the background of a XP spectrum, one has to take into account that emitted primary electrons can further interact with matter. These interactions lead to energy losses. These inelastic losses lead to an increase in background intensity at the high binding energy side of a XP spectrum. To account for this background, various types of backgrounds can be subtracted, e.g. a linear background, or more sophisticated backgrounds, such as, Shirley[93] or Tougaard[94].

In this thesis, a linear background was used for the core levels of the 2D materials, i.e. B 1s, C 1s and N 1s, as shown in Figure 2.6. A Shirley background is used, e.g. for I 4d spectra. After subtraction of the background, the remaining XP-signal is deconvoluted.

For the deconvolution of an XP-signal, an appropriate function, depending on the peak shape is used. For symmetric peaks, a Voigt function may be applied. This is a convolution of a Gaussian function, accounting for the linewidth due to the analyzer resolution and the monochromaticity of the exciting light and a Lorentzian line profile accounting for the lifetime of the excited state. However, the peak may still be asymmetric, even after subtraction of the background, e.g. due to the creation of electron-hole pairs at the Fermi edge during the photoemission process. To account for this asymmetry, a line profile according to Doniach - Šunjić, again convoluted with a Gaussian function, is chosen. Again, the width of the two functions is due to the spectral broadening of the apparatus and the lifetime, respectively. In Figure 2.6c, the data is fitted with a Doniach - Šunjić function due to its asymmetry. This asymmetry is observed for all the core levels of the 2D materials.

The integrated peak area of the XPS signal corresponds to the amount of electron emitters, i.e. atoms, in the probed sample volume. This allows for a quantitative analysis of XPS data. However, diffraction (photoelectron diffraction, PED) may lead to a change in signal intensity: Electrons that are emitted with a kinetic energy of about 100 eV show a large surface sensitivity and thus are applied when probing surface sensitive XPS. However, electrons with this energy are also routinely used in e.g. low energy electron diffraction (LEED), as their wavelength is similar to atomic distances, and thus show diffraction. This diffraction can lead to an apparent increase or decrease of intensity of the emitted electrons.

As PED is present for all samples with local order, such as the investigated 2D materials and has an influence on electron emission angle, it influences all XP spectra. To better understand the effect of diffraction on a system under investigation, the angle between the sample and the analyzer, or the excitation energy of the incoming X-rays may be changed.

2.4 Near-edge X-ray absorption fine structure

A further method that needs a synchrotron as radiation source, in particular the tunable energy, is near-edge X-ray absorption fine structure (NEXAFS) spectroscopy. The method measures the absorption of X-rays in matter, depending on the energy of the incidence light. As the name of the method already implies, only the near edge region is measured. The near edge region is considered to be from the absorption edge, to ~ 20 eV after the edge. As is discussed below, in this region nearly all information on adsorbates is gained.

For NEXAFS several detection methods are available that can be used as a probe, e.g., electrons, which are emitted upon absorption or also transmitted photons. Thus, the following types of NEXAFS measurement are available: Transmission measurement, where the loss in incidence intensity is detected. Photon yield, where secondary photons, generated by the decay of a core hole, are detected, i.e. the X-ray fluorescence. Total yield, where all electrons emitted from the sample are detected, in most setups as a current versus ground. Partial yield, where electrons emitted from the sample, which have only lost a certain kinetic energy are detected. And lastly, Auger yield, where only electrons with a certain kinetic energy window are detected.

In this thesis, partial yield NEXAFS was measured using a home-build detector. The partial yield method has the following advantages: It is surface sensitive, as it detects electrons, which must have a certain kinetic energy, thus ignoring electrons that have too strongly interacted with the substrate, i.e. from deeper within the sample. Furthermore, it shows still rather large signal intensity, compared to Auger yield detection.

The underlying principle of NEXAFS is the change of absorption probability of matter with the change in photon energy. The change in photon energy is achieved with a synchrotron light source[95]. The principle of NEXAFS is depicted in Figure 2.7. When the sample is irradiated with light of a suiting wavelength, electrons are resonantly excited from occupied states into unoccupied states. The unoccupied π^* orbitals are below the ionization threshold and have a small energy distribution, resulting in sharp features at low photon energies. The σ^* orbitals have a broader energy width and are located above the ionization threshold and only separated from the vacuum by the centrifugal barrier[95].

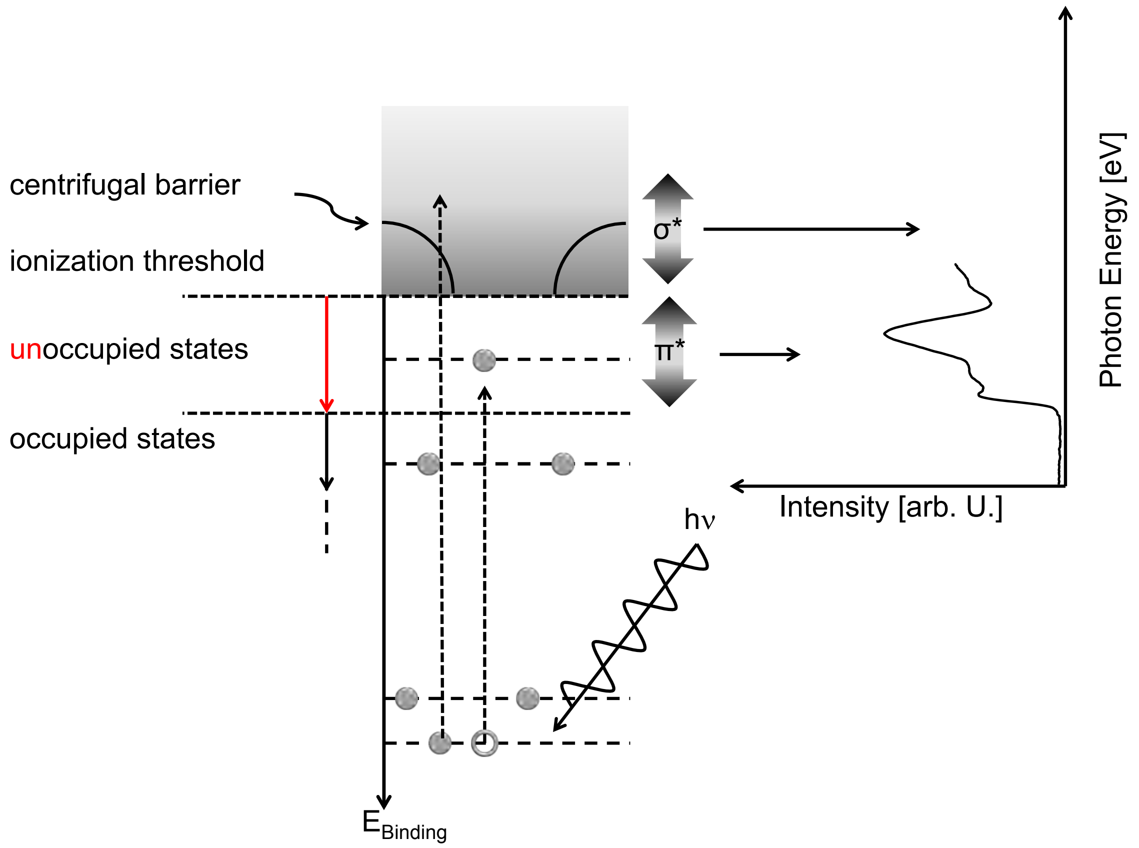

Figure 2.7 A schematic depiction of the light absorption and the resulting excitation of electrons occurring during a NEXAFS measurement. On the right, an nitrogen K-edge absorption spectrum of h-BN/Ni(111) measured at 50° is shown.

As synchrotron light form an insertion device is polarized also information on the orientation of an adsorbate can be obtained from NEXAFS. The adsorption probability is given by the overlap of the dipole operator, with the wave function of the initial and the final state of the electron, according to Fermis golden rule. Therefore, information on the symmetry is obtained[96]. In the case of measurements at the K-edges this means that the absorption probability increases drastically, when the wave vector of the incoming light is parallel to an empty orbital into which the electron is excited, thus information on the geometry is obtained. Moreover, the character of the bonds present on the surface can be determined (e.g. σ or π-bonds), as these absorb in significantly different photon energy ranges. The information of the bond orientation is gained by changing the angle of the incoming light to the sample. For 2D materials, like graphene and h-BN, where the π-bonds are in-plane of 2D material, grazing incidence measurement geometry yields information on these bonds. In contrast, a measurement with the incoming light at normal incidence (X-rays hit perpendicular to the surface) yields information on the σ-bonds[97]. In this thesis, only absorption from the K-edge is investigated, as it contains the desired information on the orientation of the σ or π-bonds and is accessible, for the row 2 elements (boron to oxygen) with the wavelengths available.

The NEXAFS spectra show also a chemical shift, as discussed above for XPS, and thus also the unoccupied states are affected. NEXAFS also shows sensitivity for the chemical surrounding of the probed core-level. The most interesting probed states of 2D materials absorbed on various substrates are the so-called interlayer states, originating from the interaction of the 2D material with its substrate[62,98]. These are present, if the 2D material interacts strongly with the support, while they vanish, if it shows a quasi-free-standing character. NEXAFS for both free-standing as well as heavily interacting 2D materials are available in literature. Thus an easy comparison is possible, and often no further calculations or peak fitting is needed, to describe the interaction of the 2D material and the substrate.

In this thesis, NEXAFS spectra were obtained using partial yield mode (Boron-K-Edge: retardation voltage: -50 V Nitrogen K-edge retardation voltage: -340 V Oxygen K-edge retardation voltage: -490 V). The spectra were obtained by subtracting spectra of the clean Ni(111) crystal from the spectra of h-BN and hydrogen-exposed h-BN. For oxygen K-edge spectra after oxygen adsorption on Ni(111), the h-BN pre-covered Ni(111), is used as a reference. The angle between the sample surface normal and incoming light is 70° for grazing incidence and 0° for normal incidence. Also spectra taken at an angle between the surface and the incoming of 50° are shown. Thereby no angle dependent information is obtained, nevertheless a finger-print of chemical states are observed.

2.5 Temperature programmed desorption

This chapter describes temperature programmed desorption (TPD) spectrometry. For a more detailed description, the PhD thesis of Hartmut Schlichting is suggested[99]. In a TPD experiment, molecules or atoms desorbing from surfaces are detected with a quadrupole mass spectrometer (QMS) in a mass selected fashion[100]. The amount of the de-

sorbing molecules or atoms is plotted versus sample temperature, which is increased linearly. TPD allows to obtain properties of the adsorbate such as desorption energy, desorption order, and pre-exponential factor of the desorption. Moreover, the knowledge of the composition of the gas-phase above the substrate is further valuable information, which is complementary to XPS or NEXAFS, which give information on the surface species. In the case that the pumping speed is high, TPD is fully quantitative, allowing the calibration of e.g. hydrogen coverages that may only be studied indirectly with XPS. Especially the behavior of hydrogen is interesting as it can only be detected indirectly in XPS e.g. by a binding energy shifts. To describe TPD, the Polanyi-Wigner was derived, which is an Arrhenius-type equation adjusted for TDP.

$$r(\sigma) = -\frac{d\sigma}{dT} = \nu(\sigma)\nu^{n}e^{-E_{des(\sigma)}/RT}$$

With:

$r(\sigma)$**: the desorption rate [mol/cm²s]**

σ**: the surface coverage**

ν**: the pre-exponential factor, or attempt frequency [1/s]**

$E_{des(\sigma)}$**: the desorption energy**

R**: gas constant [J/(molK)]**

T**: the temperature [K]**

For a quick estimate of the desorption energy the Redhead analysis is used. Here following approximations are made[101]: The desorption is first order, the desorption energy is independent of the surface coverage and the attempt frequency is 10^{13} Hz.

$$E_{des} = RT_p(\ln\left(\frac{T_p\nu}{\beta}\right) - 3.46)$$

With additionally:

T_p**: the temperature at the desorption peak maximum**

β**: the heating rate during the experiment**

ν**: the attempt frequency, often assumed to be 10^{13} Hz**

To enhance the quality of recorded TPD spectra, a Feulner cup is installed in the TPD setup[102]. This is a cone-shaped attachment to the QMS. The size of the opening is ideally a little smaller than the size as the sample. The sample is placed close to the Feulner cup and the following advantages are gained: (i) it significantly reduces the amount of molecules not desorbing from the sample surface and still being detected. Thus, artefacts from parts of the sample holder, which are also heated during a TPD experiment, are minimized; (ii) reactions of desorbing molecules with the reactive stainless steel wall of the UHV apparatus are minimized. The Feulner cup is made out glass, or is gold coated, to ensure that molecules do not stick to the surface or react with it; (iii) the signal intensity is increased, as the molecules are guided by the Feulner cup to the QMS.

2.6 Super-sonic molecular beam

A super-sonic molecular beam (SSMB) is used in this thesis as it offers two advantages compared to effusive sources: (i) an orders of magnitude increased local pressure on the sample, compared to the background pressure in the chamber, and (ii) the kinetic energy of the adsorbates is tunable. The supersonic molecular beam was used practically for all gas exposures within this thesis, being an invaluable tool for its success. Typical applications were the synthesis of graphene that needs high pressures on the Ni(111) surface, or the formation of the oxygen species on the otherwise inert h-BN on Ni(111).

In a super-sonic molecular beam, gas is expanded through a small nozzle from a high pressure region, into high vacuum, i.e. a low pressure region. Thus, pressure differences of several orders of magnitude are breached in a small distance, where only few molecule-molecule interactions can take place. In this adiabatic expansion, the random, thermal movement of atoms in a gas phase changes to a directed flow perpendicular to the nozzle. For the molecular beam to become super-sonic, the ratio of the background pressure in the region the gas expands into (p_B) compared to the pressure the gas has in side of the nozzle (p_N) must be ~2.1[103]. In our setup, shown in Figure 2.8, p_B is about six orders of magnitude smaller compared to p_N.

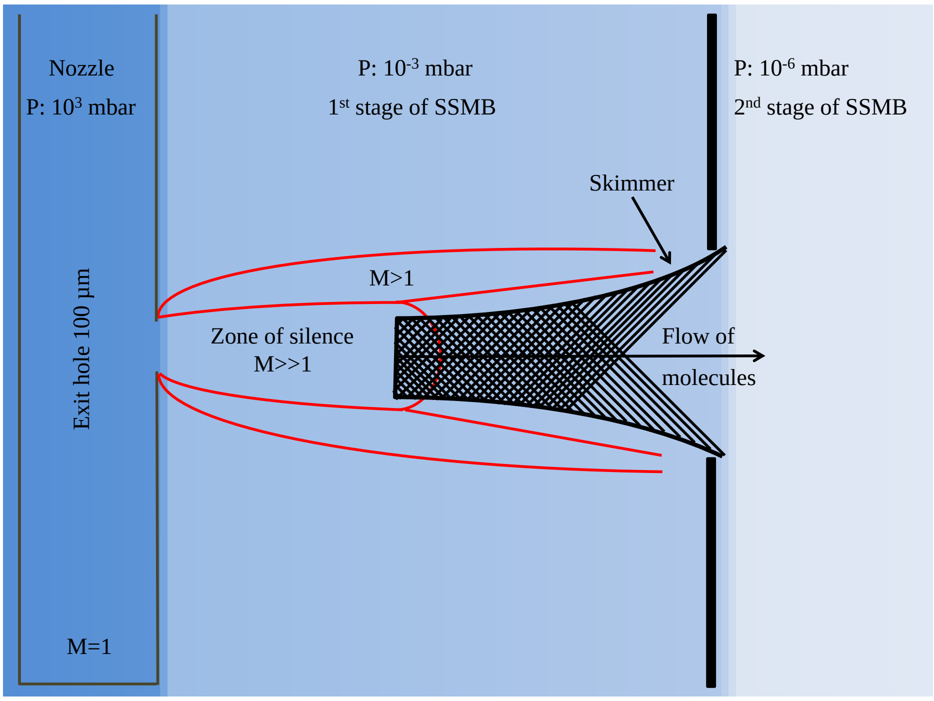

Figure 2.8 schematic of the gas flow in front of the SSMB nozzle, with the shape of the zone of silence, the skimmer and the pressures occurring during operation.

In the high pressure region in front of the nozzle, the gas is in thermal equilibrium and the energy of the gas is given in the sum of its translational, rotational and vibrational energy and has a Boltzmann distribution. Upon expansion of the gas into the vacuum on the other side of the nozzle, the thermal movement is largely converted into directed movement, through molecule-molecule collisions. The energy distribution of the molecules in the beam becomes significantly narrower as the temperature of the gas is reduced and the beam becomes directed. Also the rotational and some of the vibrational energy of the molecules is converted to translational energy. While during the expansion of the gas into the vacuum several molecule-molecule collisions occur, after the adiabatic expansion in the ideal molecular beam no more collisions of the molecules occur.

Gas molecules with the desired properties of a well-defined kinetic energy and a well-defined temperature are present in the zone of silence, see Figure 2.7, which forms in front of the nozzle on the high vacuum side. Here the molecules are faster than the speed of sound (M) thus M>>1[104]. A skimmer selects these molecules.

To increase the kinetic energy of the expanded molecular beam, the source temperature can be increased. The increase of the energy is higher than just the increase in thermal energy, as vibrational and rotational energy is also converted, as discussed above. The second possibility to increase the kinetic energy is to add a lighter seeding gas. Typically light and inert gases, commonly helium or neon, are added in large excess to the adsorbing gas[105]. Before the expansion, the two gases have the same temperature; however, as the seeding gas is significantly lighter, the molecules have a higher velocity. Upon expansion, the velocities of the two gases equilibrate. This leads to an increase in the kinetic energy of the heavier / reactive gas. Thus, the energy of the gases is within a certain window fully tunable. It is possible to increase the translational energy of the heavier gas by a factor of $\frac{m_{gas}}{m_{Seeding\ Gas}}$. To determine the exact energy of the gases time-of-flight spectra have to be recorded for each SSMB setup and each adsorbate and ratio of seeding gas to reactive gas. As an estimate, one can use the formula given by Kneitz[106,107]:

$$< v > = \sqrt{2\, E_{kin} m_{gas}} = \sqrt{\frac{(5 + A_{gas}) k_B T_N}{A_{He} m_{He} + A_{gas} m_{gas}}}$$

The following parameters are used:

$< v >$: mean velocity

E_{kin}: kinetic energy of the seeded gas molecules

m_x: Atomic mass of gas x

A_x: share of x in the gas mixture

k_B: Boltzmann's constant

T_N: Temperature of the nozzle

This formula however, does not take into account that the mean velocities for the seeding gas and the seeded gas do not equilibrate completely (known as velocity slip). This velocity slip is present for even rather small mass differences between seeding and seeded gas, like oxygen and carbon monoxide seeded with helium. Thus an error of up to 50% can occur. For heavier gases, the velocity slip increases further.

2.7 Experimental Setups

In this thesis two UHV setups were used. One is a transportable XPS apparatus, named Sync, which is transported to BESSY II in Berlin. The second UHV apparatus is used to measure TPD data, as it is equipped with a Feulner cup. Both apparatus are described shortly below.

2.7.1 Sync apparatus

The Sync apparatus is a two chamber setup[108] with a preparation and an analysis chamber. The sample is transferable between the two chambers with a xyz manipulator, with which the sample can also be rotated in two axis, cooled to ~100 K and heated to ~1400 K. Behind the sample, a filament is mounted enabling radiative heating and linear heating ramps, while measuring XPS at the same time, without disturbing the photoemission measurements.

To the preparation chamber a sputter gun is mounted that was used for argon ion bombardment to clean the sample but also for intercalating argon under graphene. Similarly, the gun was used to bombard graphene with nitrogen ions for functionalization. As a further functionalization tool, an atomic hydrogen source is mounted. Moreover an Er-LEED is attached to the chamber, for low energy electron diffraction measurements. The second chamber is the analysis chamber. During operation at a synchrotron this chamber is connected to the beamline. It houses the Omicron EA 125 HR U7 electron analyzer, and the home built NEXAFS partial yield analyzer. A quadrupole mass spectrometer (QMS, Pfeiffer Vacuum QME200) and a capillary array doser, to exposes samples to e.g. borazine, are mounted. The SSMB is also connected to this chamber, such that the sample is hit with the beam of molecules, in the same spot as the focus of the electron analyzer and the X-rays from the synchrotron.

2.7.2 Temperature programed desorption apparatus

The TPD machine is a single chamber setup. It is equipped with an Er-LEED, a dosing system to dose gases, an effusive cell, a magnesium and aluminum twin anode and an electron analyzer for XPS and a QMS (Pfeiffer Vacuum QME200) connected to a Feulner Cup. The Feulner Cup facilitates the acquisition of low background TPD spectra, as the molecules desorbing from the sample holder and manipulator are blocked from reaching the QMS. The sample is mounted to a xyz-manipulator. Resistive heating to 1400 K and cooling with liquid nitrogen to 90 K is possible. The TPD data shown in this thesis was gathered with this apparatus.

3 Hydrogenation of nitrogen-doped graphene

The results in this chapter have already been published and the text is has been adapted from this publication:

Hydrogenation and dehydrogenation of nitrogen-doped graphene investigated by X-ray photoelectron spectroscopy, F. Späth, W. Zhao, C. Gleichweit, K. Gotterbarm, U. Bauer, O. Höfert, H. P. Steinrück, C. Papp, *Surf. Sci.* 2015, *634*, 89–94[109].

The binding configuration of nitrogen-doped graphene, prepared with ion-implantation was previously investigated by Zhao et al.[110]. Two stable configurations for the implanted nitrogen in the graphene carbon back-bone were found. These are graphitic nitrogen, substituting a carbon atom, and pyridinic nitrogen. The pyridinic nitrogen is at a defect site, with at least one carbon atom missing, in a twofold coordination. The nitrogen-doped graphene is exposed to hot atomic hydrogen at a sample temperature of 180 K. Upon atomic hydrogen exposure, a distinctive new species in the C 1s core level is observed. From previous experiments, this species is assigned to hydrogenated carbon, in the graphene backbone. Heating experiments after different atomic hydrogen exposures show that the reactivity of the carbon backbone towards atomic hydrogen does not change due to the nitrogen doping. In the N 1s core level, upon exposure to atomic hydrogen, we find that both nitrogen species bind hydrogen, and thus two new species are found in XPS, with a binding energy 1 eV higher compared to the non-hydrogenated nitrogen. The reactivity of the nitrogen species towards atomic hydrogen is as following: Graphitic nitrogen shows a similar affinity to atomic hydrogen as the carbon in graphene. Pyridinic nitrogen shows a higher reactivity, and thus for the same hydrogen exposure more of the pyridinic nitrogen is hydrogenated, compared to carbon. Temperature programmed experiments show that the desorption mechanism for hydrogen bonded to nitrogen is different for graphitic and pyridinic nitrogen. Pyridinic nitrogen shows two desorption maxima for high hydrogen coverages, as does the carbon in hydrogenated graphene, while graphitic nitrogen only shows one desorption maximum, indicating a different hydrogen bond strength.

3.1 Introduction

Graphene, a 2D material consisting of honeycomb arranged sp^2-hybridized carbon atoms, has gained significant interest over the last years, due to its unusual physical and chemical properties[111,112]. These include a high charge carrier mobility[73], due to its linear dispersion at the Dirac point[113], its high transparency[114], which makes it a potential candidate as a replacement for indium tin oxide in modern display technology. Its inertness[115] and impermeability[28] are some of its outstanding chemical properties; in this context, applications as membrane, and for corrosion protection[27,116] as well as for gas separation[26,117] and detection[118] are discussed.

One other important application of graphene, often discussed in literature, is as a potential hydrogen storage material[119]. Due to its unsaturated carbon backbone, it is possible to attach one hydrogen atom to every carbon atom of graphene, yielding exclusively sp^3-hybridized carbon atoms. The resulting material is denoted as graphane (C_nH_n) and has a high hydrogen storage capacity[43,120]. In case of hydrogenation of supported graphene, i.e., of a graphene layer adsorbed on a solid surface, the achievable degree of hydrogenation depends on the surface and the specific interaction between graphene and the surface: For graphene on SiO_2/Si 17 % of carbon atoms can be hydrogenated[121]; for hydrogenation with molecular hydrogen on Ir(111) intercalation is found, and the intercalated hydrogen can react with graphene[64]. On Ni(111), hydrogenation of 50 % of the carbon atoms is found (at sufficiently high exposure to atomic hydrogen), resulting in single-side hydrogenated graphene; in this so-called graphone-($C_nH_{n/2}$), the non-hydrogenated carbon atoms strongly interact with Ni surface. If gold is intercalated between Ni(111) and graphene, only 25% of the carbon atoms bind hydrogen[44]. For a potential application, in addition to a high storage capacity also a sufficiently low release temperature of hydrogen, preferably close to room temperature is required. Furthermore, the hydrogen storage and release processes should be fully reversible, i.e., no loss of carbon should occur, as this would deteriorate the storage material and also could poison a hydrogen fuel cell.

To tune the electronic and chemical properties of graphene, doping and chemical modification have been proposed as two suitable pathways. Doping of graphene can induce a band gap that is crucial for applications in the semiconductor industry. The neighbors in the periodic system of elements, nitrogen and boron, are the natural candidates for such a chemical doping, and we herein will focus on nitrogen-doped graphene (NDG). NDG has already received considerable attention[110,122,123], and applications in ultra-capacitors and lithium ion batteries, electrochemical biosensing, and as metal-free electrocatalyst for oxygen reduction in fuel cells[124–127] have been proposed in literature. Furthermore, also the chemical reactivity of the dopants is of interest, as covalent doping-sites in graphene could serve as potential anchor points for further functionalization.

In this chapter we report on the investigation of the hydrogenation and dehydrogenation of nitrogen-doped graphene supported on Ni(111) by in situ high-resolution photoelectron spectroscopy. In the past, this method has proven to be very powerful to characterize the preparation of nitrogen-doped graphene on the one hand[122,128] and the hydrogenation of undoped graphene on the other hand[42,129]. Herein, we present the first study addressing the hydrogenation of nitrogen-doped graphene. From the analysis of the C 1s and N 1s spectra during heating of a hydrogenated layer detailed information on the hydrogenation and dehydrogenation are obtained. In particular, differences between the hydrogenation of different nitrogen species, i.e. graphitic and pyridinic nitrogen are evaluated.

3.2 Results and Discussion

Doping is achieved by bombarding graphene with low energy nitrogen ions using the sputter gun. The doping process is described in detail elsewhere[110]. The dinitrogen partial pressure during doping was $5x10^{-6}$ mbar, the ion current on the sample was approx. 350 nA, and the sample temperature below 170 K. The kinetic energy of the nitrogen ions was 50 eV. The samples were sputtered for 10 min, yielding N amounts between

0.027 and 0.045 ML as was determined for each preparation by XPS. These amounts are very similar to values obtained in earlier work under similar conditions[110]. As the overall amount of N is very low, and varies slightly from experiment to experiment, as discussed above, we use the fractions of hydrogenated nitrogen species to describe the degree of hydrogenation throughout this paper, with the absolute amounts denoted in the figure captions. The hydrogenation of graphene was achieved by using atomic hydrogen from a dihydrogen (H_2) cracking source. The background H_2 pressure in the chamber during hydrogenation was between $1x10^{-7}$ and $5x10^{-7}$ mbar, depending on the desired exposure. As the sample was close to the hydrogen source, the absolute pressure of atomic hydrogen differs from the values given.

Hydrogenation of carbon in nitrogen-doped graphene

When dosing atomic hydrogen onto NDG, both the carbon and the nitrogen species react, and subsequently a variety of new species are identified in the C 1s and N 1s spectra. The behavior in the C 1s spectra largely mimics the behavior found for undoped graphene on Ni(111), which has been reported on in great detail recently; see[42]. As we herein focus on the reactivity of the dopant atoms in nitrogen-doped graphene, we will restrict the discussion of the C 1s spectra to one typical measurement, which is shown in Figure 3.1. The spectrum at 180 K in Figure 3.1a (black) has been collected after exposing NDG to 90 L atomic hydrogen. In addition to the signal of pristine graphene at 284.9 eV, a new H-induced species is found at 284.4 eV; its binding energy is in good agreement with the value of 284.3 eV found for hydrogenation of pristine graphene. This signal stems from sp^3-hybridized carbon atoms to which the hydrogen is bound. After the adsorption experiment, dehydrogenation was studied by applying a constant temperature ramp, while continuously measuring XP spectra, i.e. by performing a temperature programmed XPS experiment. Spectra at selected temperatures are show in Figure 3.1a, and the complete data set is shown in Figure 3.1b in a color-coded density plot. The quantitative analysis obtained by peak-fitting this experiment is depicted in Figure 3.1c. Upon heating, characteristic changes are observed in the XP spectra that are assigned to a stepwise dehydrogenation yielding gaseous H_2. The spectrum at 650 K is identical to that of the surface prior to exposure to hydrogen, reflecting the reversibility of the hydrogenation/ dehydrogenation process. The rate maxima, i.e. the H_2 desorption temperatures, are determined from the inflection points of the decrease of the hydrogenated graphene signal (which goes along with the increase of graphene signal) in Figure 3.1c, to be at 330 and 600 K. We thus observe stepwise dehydrogenation, at two characteristic temperatures, very similar to the behavior during the dehydrogenation of hydrogenated undoped graphene[42]. The similarity also holds for the hydrogen coverage of 0.9 ± 0.1 ML, which, within the error bars of the experiment and the fitting procedure, is identical to the value found for undoped graphene (1.1 ± 0.1 ML) at the same exposure. Interestingly, we do not observe any new species in the C 1s core level region as compared to hydrogenated undoped graphene. This may be due to the low concentration and a similar binding energy of new components such as C-N-H groups that are formed. Furthermore, we observe no irreversible effects that the hydrogenation might have on graphene, e.g. binding energy shifts, due to altering the graphene substrate interactions, or loss of carbon due to etching, i.e. desorption of C_mH_n species. This is somewhat surprising since NDG has, due to the applied preparation method, a significant number of defects and could thus be prone to etching; such etching effects were found for example for defective graphene with molecular oxygen on Rh(111)[130]. In summary, our findings for the C 1s core level, i.e. the carbon in hydrogenated NDG are identical to our findings for undoped graphene on Ni(111), considering uncertainties in all steps of the preparation and data evaluation. Next, we discuss our findings for the nitrogen in NDG.

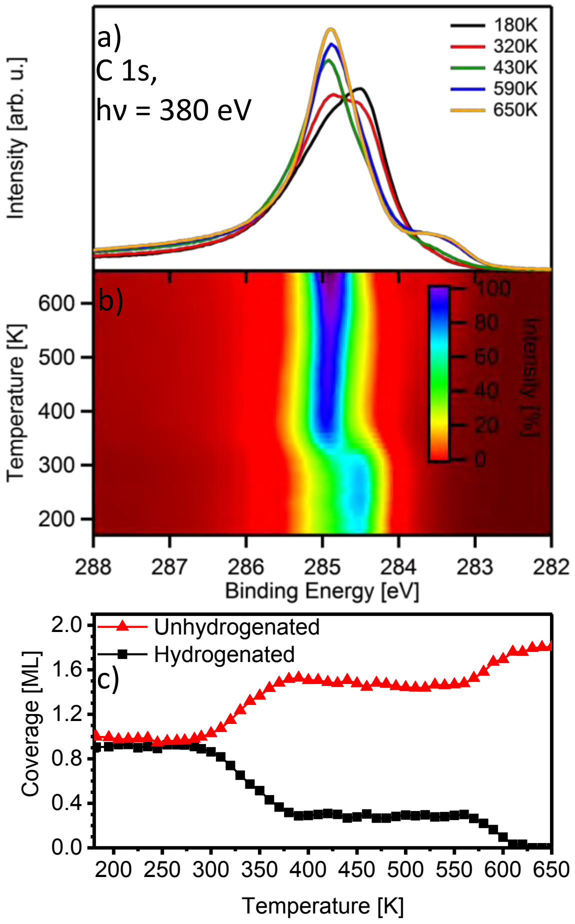

Figure 3.1: TPXPS experiment in the C 1s core level of NDG (ΘN = 0.029 ML) exposed to 90 L atomic hydrogen. (a) Selected spectra recorded at characteristic temperatures; (b) color-coded density plot of full data set; (c) Quantitative analysis of the experiment. The signal due to carbidic carbon (~283.5 eV) is not shown.

Hydrogenation of nitrogen in nitrogen-doped graphene

To start with, we discuss the nitrogen species in NDG prior to exposure to hydrogen. In previous experiments and calculations[122], we were able to identify two main nitrogen species in NDG in the N 1s spectra; see Figure 3.2 a, bottom spectrum. The first is substitutional nitrogen, also denoted as graphitic nitrogen, N(G), at a binding energy of 400.6 eV, and has a similar bonding configuration as carbon in graphene. The second is pyridinic nitrogen, N(P), at a binding energy of 398.8 eV; it has only two neighboring C atoms, and a vacancy next to it. Note that we are not able to distinguish other geometries of the nitrogen, e.g. nitrogen at a zig-zag or an armchair edge[131]. Furthermore, from intercalation experiments it was deduced that the pyridinic nitrogen interacts with the surface, while the graphitic nitrogen does not, e.g. it does not show a shift to lower binding energies upon Au intercalation[122].

When NDG is exposed to atomic hydrogen, the following changes in the nitrogen spectra are observed in Figure 3.2a: The two well-separated peaks of pyridinic and graphitic nitrogen loose intensity and two new features appear. This is most obvious at the highest exposure of 180 L and in the corresponding fits in Figure 3.3 c, where new contributions are identified at 399.5 and 401.8 eV, i.e. one peak in between the original peaks and one at higher binding energies, and a shift of the pyridinic and graphitic nitrogen to 398.2 and 400.5 eV, respectively, is observed. From the spectra for increasing H exposure in Figure 3.2a and the quantitative analysis in Figure 3.2b, it is evident that pyridinic nitrogen is hydrogenated faster than graphitic nitrogen. For both species, hydrogenation seems to saturate at 180 L, with values $N(P)H \ / \ N(P)_{total} = 0.63$ for pyridinic nitrogen and $N(G)H \ / \ N(G)_{total} = 0.48$ for graphitic nitrogen.

Next, we discuss the peak assignment: We observe two new peaks which are intuitively assigned to the hydrogenated form of the formerly non-hydrogenated nitrogen atoms in NDG. The peaks shift from 398.2 to 399.5 eV upon hydrogenation of pyridinc N, and from 400.5 to 401.8 eV upon hydrogenation of graphitic carbon. On average in all experiments a binding energy difference of 1.2 ± 0.1 eV is observed between the hydrogenated and unhydrogenated nitrogen species.

This magnitude of this difference and its direction towards higher binding energy is in line with differences observed for other systems with hydrogenated and dehydrogenated (substituted / unsubstituted) nitrogen species, e.g., pyrrole[132], dodecahydro-N-ethylcarbazole on Pt(111)[133] and metalloporphyrins on Ag(111)[134]. The smaller value for this binding energy difference in our case might be due to different substrate or due to the very confined conjugated π-system in the case of furan. Since the Gaussian width of all species found in NDG does not change during the thermal evolution (see below), we conclude that no further species (apart from a small nickel nitride contribution at ~397 eV) is contributing to the spectra. The larger width of both hydrogenated species by 10% may be either explained with N-H vibrational excitations in the ionic final state[135] or by unresolved lines due to slightly different adsorption geometries for the hydrogenated nitrogen species[136].

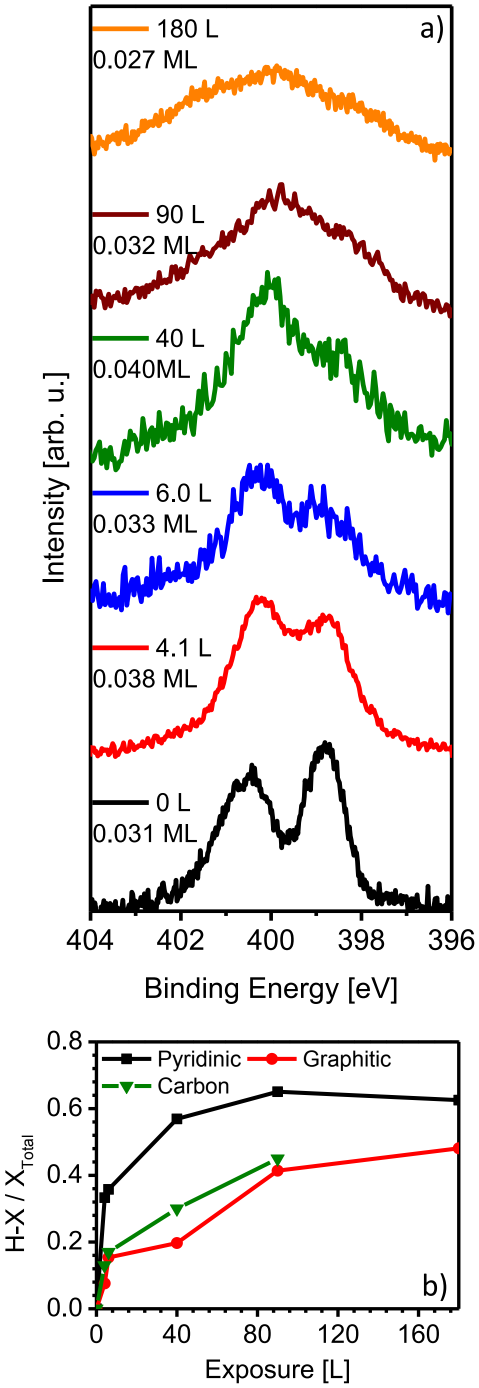

Figure 3.2: (a) Spectra in the N 1s region taken at 170 K at different, hydrogen exposures, as denoted; (b) relative degree of hydrogenation X-H/X_{Total}, for pyridinic and graphitic nitrogen, as well as carbon, at 170 K. Note that for each H exposure a separate NDG layer was prepared with slightly different total N amounts in each case, as denoted in (a).

To investigate the dehydrogenation of the hydrogenated NDG layer, i.e. the stability of the new hydrogenated nitrogen species, a temperature-programmed XPS (TPXPS) experiment was conducted. Selected N 1s after a hydrogen exposure of 180 L are shown in Figure 3.3d, and the complete data set as color-coded density plot in Figure 3.3b. In this experiment, an initial amount of 0.027 ML of nitrogen was incorporated into the graphene sheet. The spectrum at 170 K corresponds to the NDG layer saturated with hydrogen, i.e., it shows the broad structure due to superposition of two new contributions of the hydrogenated nitrogens (401.8, 399.5 eV) and the two contributions of the remaining non-hydrogenated nitrogens (398.2, 400.5 eV) - see fit in Figure 3.3c. With increasing temperature, the signals due to hydrogenated nitrogen decrease, and at 650 K the spectra resemble those observed prior to hydrogenation. From the color-coded density plot, one finds that the two new hydrogenated species start to decrease at about the same temperature of ~340 K, which is attributed to dehydrogenation. By fitting the spectra during heating (see exemplary fits in Figure 3.3a and 3.3c) the quantitative analysis of the thermal evolution in Figure 3.4 is obtained. We would like to add that at no time we were able to detect any beam damage due to the synchrotron radiation. This is in line with a previous study on the hydrogenation of graphene, where also no beam damage was observable.

For the hydrogenated graphitic nitrogen, which is structurally similar to carbon in graphene in terms of its bonding situation (three neighbors), we find a slow, steady initial decrease between 170 to 330 K (by ~15%). At higher temperature, the decrease strongly accelerates, resulting in a complete dehydrogenation until 420 K, i.e., within a temperature window of 90 K. When comparing this to the dehydrogenation of the carbon atoms in NDG (and also in hydrogenated undoped graphene), we find that the rate maximum for dehydrogenation (as determined from the inflection points in Figure 3.2c and Figure 3.4) is found at somewhat higher temperatures than for the hydrogenated graphitic nitrogen. The fraction of 0.48 of graphitic nitrogen that has reacted with hydrogen found in Figure 3.4 compares well with the fraction of 0.45 of carbon atoms that have reacted with hydrogen deduced from Figure 3.2b. This could be the result of graphitic (i.e., substitutional) nitrogen having a graphone-like configuration and thus the same amount of hydrogen can be stored, as in carbon for H-NDG. For pyridinic nitrogen, we initially find a similar behavior: A slow decrease is observed (by ~18%) up to ~ 330 K, which is followed by a steeper decrease. In contrast to the graphitic nitrogen, the signal does, however, not disappear at 420 K but reaches a level of ~40% of the original value. Upon further heating, it slowly decreases until 580K, followed by a very steep decrease to zero at 600 K. This latter behavior is very similar to that observed for hydrogenated carbon in NDG.

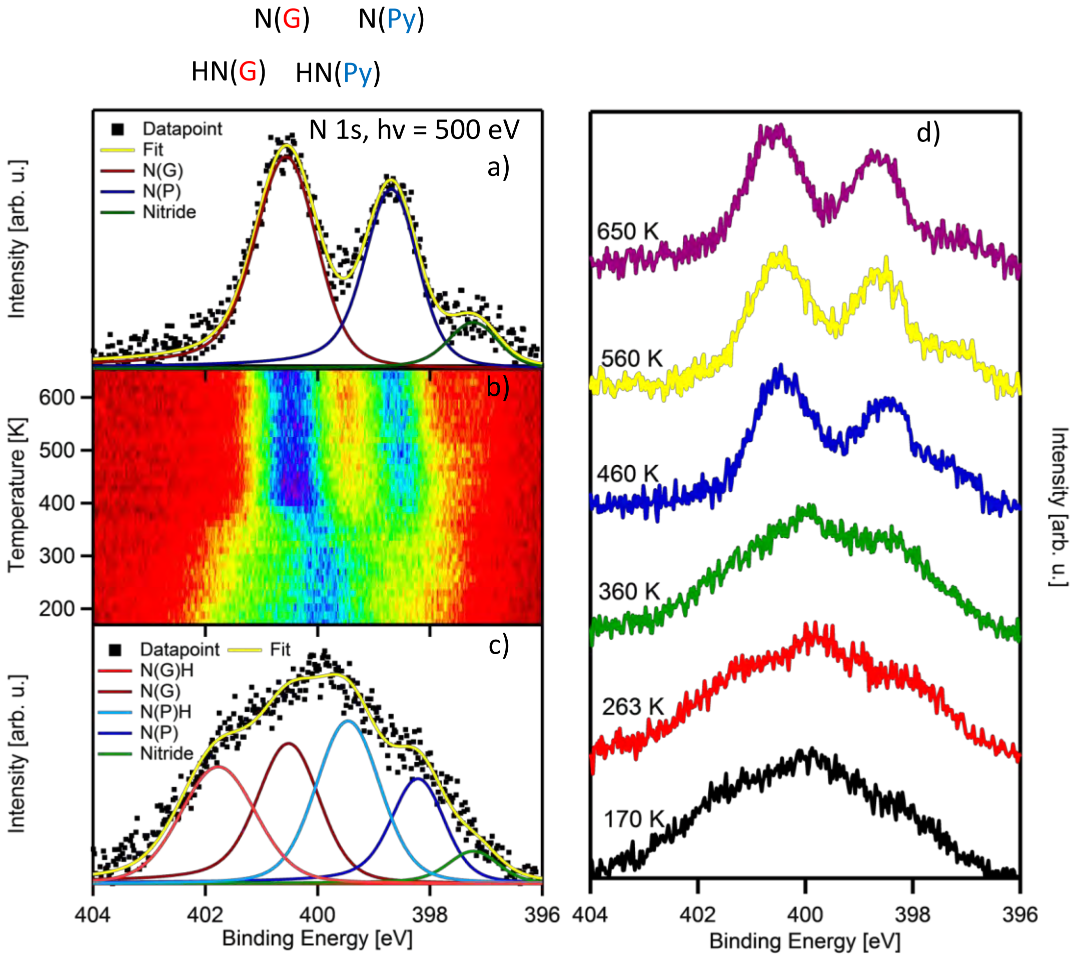

Figure 3.3: Thermal evolution of NDG exposed to 180 L hydrogen. (a) Deconvolution at 650 K (highest recorded temperature). (b) Color-coded density plot of the thermal evolution of H-NDG; spectra are collected every 12 K. (c) Spectra recorded at the lowest temperature (170 K). (d) Spectra at characteristic temperatures. $\Theta_N = 0.027$ *ML*

In addition to the experiments performed after a hydrogen exposure of 180 L, we also performed TP-XPS experiments after lower exposures, from 4 to 180 L. The quantitative analysis of these experiments is shown in Figure 3.5. In line with Figure 3.2b, the amount of hydrogenated pyridinic and graphitic nitrogen formed after exposure at 170 K increases with hydrogen exposure, with saturation (within the margin of error) achieved for both species at 180 L. The thermal evolution overall shows the same behavior as found already in Figure 3.4. For pyridinic nitrogen (Figure 3.5b), we find stepwise dehydrogenation with two rate maxima (i.e. inflection points) at 340-370 and ~590-620 K, regardless of the hydrogen exposure. This situation is similar to the situation of carbon in undoped and N-doped graphene. For graphitic nitrogen, complete dehydrogenation already occurs upon heating to ~420 K.

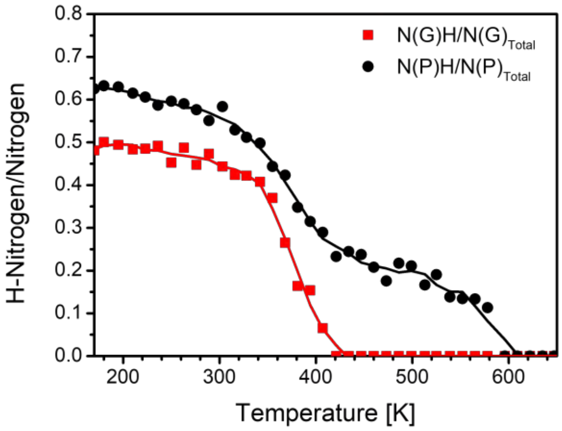

Figure 3.4: Quantitative analysis of the thermal evolution of NDG exposed to 180 L hydrogen, obtained by fitting of the data in Figure 3.3. The symbols represent the experimental data, the line serve as guide to the eye.

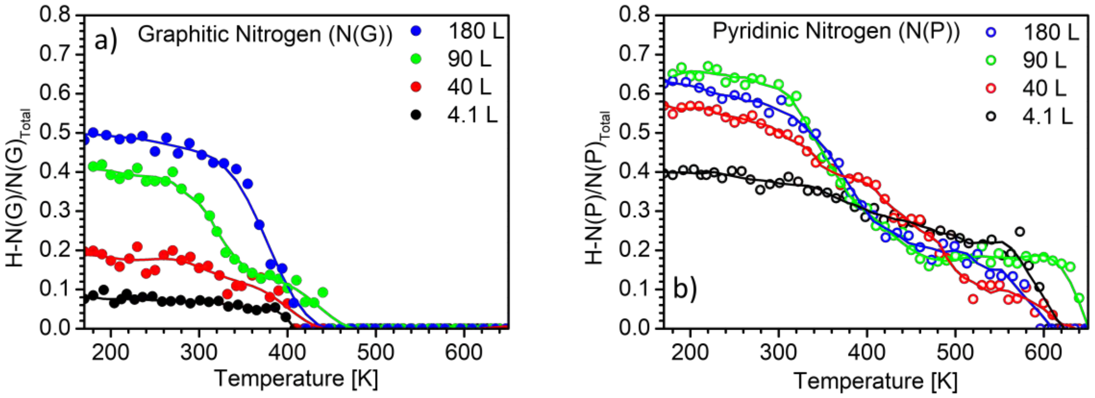

Figure 3.5: Quantitative analysis of all probed exposures. (a) Graphitic nitrogen; (b) pyridinic nitrogen. The symbols represent the experimental data, the lines serve as guide to the eye.

For all coverages, there is one intriguing difference in the hydrogenation of pyridinic nitrogen as compared to graphitic nitrogen and carbon in NDG. This is the larger fraction that has reacted with hydrogen: At saturation (180 L exposure), we find a ratio of 0.63 for pyridinic N, as compared to 0.48 for graphitic N and 0.45 for carbon in NDG (experimental uncertainty: ± 0.05). A possible explanation is the different electronic structure and local environment of pyridinic N, which sits next to a vacancy. For graphitic N and C atoms, which are part of the hexagonal lattice (with 3 neighbors), the expected ratio for the proposed single-side hydrogenation of graphene on Ni(111) is 0.50, due to the fact that hydrogenation of a specific N(G) or C atom impedes hydrogenation of the second atom in the graphene unit cell, which bonds to the Ni substrate. The situation is different for pyridinic nitrogen which sits next to a defect. If hydrogenation was more efficient for pyridinic nitrogen than for carbon, then one expects a ratio of larger than 0.5, with the limiting case of no hydrogenation of carbon atoms and a full hydrogenation of pyridinic nitrogen, i.e. a ratio of 1.0. This is due to the fact that pyridinic N atoms are structurally different from carbon atoms and graphitic (substitutional) nitrogen atoms, i.e. they have a neighboring vacancy, and thus the restrictions for hydrogenation do not apply. From our data, we indeed have evidence that the reactivity of pyridinic nitrogen is larger than that of carbon and graphitic nitrogen in NDG: This is deduced from the achieved (relative) coverage after a given exposure. For 6 L, we find ratios of 0.36 for pyridinic N and 0.17 for carbon that is comparable to the value of 0.15 for graphitic nitrogen (see Figure 3.2b). The lower reactivity of graphitic nitrogen compared to pyridinic nitrogen also explains the observed saturation ratio of 0.48 for this site. Since the graphitic nitrogen is incorporated in the graphene lattice, it follows the behavior of the carbon atoms with every other atom hydrogenated, also leading to the same saturation of 0.5[137,138]. Interestingly we find an even lower stability of hydrogenated graphitic nitrogen, as we observe a complete dehydrogenation at 420 K, in contrast to pyridinic nitrogen and carbon, where a temperature of 600 K is needed. Furthermore, we want to mention here that we do not know the exact hybridization of graphitic nitrogen after hydrogenation.

3.3 Conclusions

To summarize, when studying the hydrogenation of nitrogen-doped graphene, we found two new species in addition to hydrogenated carbon atoms. These new species are hydrogenated pyridinic and hydrogenated graphitic nitrogen. The hydrogenation and dehydrogenation of the carbon lattice is not influenced by the doping with nitrogen. For the two hydrogenated nitrogen species, we found different and distinct chemical behavior. The fraction of 0.63 of hydrogenated pyridinic nitrogen was higher than the fractions observed for graphitic nitrogen and carbon in nitrogen-doped graphene, where value of 0.48 and 0.45, respectively, were observed. This behavior is attributed to an enhanced reactivity of pyridinic nitrogen towards hydrogen. Hydrogenated pyridinic nitrogen shows a similar dehydrogenation behavior than carbon in non-doped graphene. Dehydrogenation occurs stepwise with two rate maxima at ~370 and 600 K. Graphitic nitrogen is found to be much less reactive than pyridinic nitrogen, which is also reflected in the fact that complete dehydrogenation of these nitrogen atoms is already achieved at 420 K. Thus, at higher temperatures hydrogen is exclusively bound to pyridinic nitrogen and carbon.

The reaction of nitrogen-doped graphene with atomic hydrogen shows that specifically the strong interaction of 2D materials with the substrate facilitates an interesting tool for the functionalization. This will be shown to be a general trend in the next chapter on the reaction of h-BN with atomic hydrogen.

4 Hydrogenation of h-BN/Ni(111)

The results in this chapter have already been published and the text has been adopted from this publication:

Hydrogenation and hydrogen intercalation of hexagonal boron nitride on Ni(111): Reactivity and electronic structure, F. Späth*, J. Gebhardt*, F. Düll, U. Bauer, P. Bachmann, C. Gleichweit, A. Görling, H. P. Steinrück, C. Papp, *2D Mater.* 2017, *4*, 35026[139]. (*shared first authors)

In the following the reactivity of h-BN on Ni(111) towards atomic hydrogen is investigated over a wide exposure range. h-BNs analogue, graphene, was already investigated in detail and a reaction mechanism was found[42]. For graphene, a hydrogen coverage-dependent desorption mechanism was observed. For low hydrogen coverages, the hydrogen atoms must overcome a diffusion barrier on the surface at higher temperatures to recombine and desorb. For higher coverages, the majority of the hydrogen atoms have neighboring hydrogen atoms. Thus, recombination is not limited by diffusion and desorption at lower temperature is observed. For h-BN, a similar dependence of the desorption temperature was found. However, extensive NEXFAS measurements revealed that for high hydrogen exposures h-BN becomes quasi-free-standing. Thus hydrogen intercalation is observed. Low atomic hydrogen exposures, similar to graphene, result in hydrogen bonding to the surface of h-BN. The desorption temperature for intercalated hydrogen is 390 K, while the desorption temperature for bonded hydrogen is 600 K. The hydrogen bonding likely occurs at the boron sites. The results were further affirmed by DFT calculations. Moreover, the DFT calculations revealed that h-BN also shows two adsorption geometries on Ni(111), as does graphene. However, these are not discernable with XPS.

4.1 Introduction

Hexagonal-Boron Nitride (h-BN) has attracted great attention over the last years, due to its interesting electronic and chemical properties. Similar to graphene, h-BN has a honeycomb two-dimensional (2D) structure, which is composed of alternating nitrogen and boron atoms[52,140,141]. Its electronic properties are very different from the semi-metal graphene that is, h-BN is an insulator with a bandgap of ~5 eV[76,77,142]. One promising application is the use as a dielectric substrate for future graphene-based transistors, as it was recently shown that graphene can directly be grown on h-BN[97,143–145]. The chemical properties of h-BN are similar to those of graphene: It is very inert, and harsh conditions have to be used in order to functionalize or dissolve h-BN[146]. Recently, it was reported that h-BN is even less prone to oxidation than graphene and may be used as a coating for oxidation protection and friction reduction[147]. With its unsaturated π-electron system, h-BN is a promising candidate for hydrogen storage. It was recently shown that it has similar promising properties as carbon-based materials[148]. Full hydrogenation of one side of h-BN would allow for storing 3.9 wt% (weight percent) of hydrogen. This single-side hydrogenated h-BN is isoelectronic to graphone, which has been reported to be stable on Ni(111) at low temperatures[42,109]. Fully hydrogenated h-BN could even store up to 7.5 wt% of hydrogen.

However, only few studies were conducted on the hydrogenation of h-BN, with three investigating it on a Ni(111) substrate[98,149,150]. Using X-ray photoelectron spectroscopy (XPS) and near edge X-ray absorption fine structure (NEXAFS) measurements, these studies focus on a particular coverage of atomic hydrogen, thereby ignoring possible dependencies on hydrogen coverage. For the chosen conditions, hydrogenation at B sites that is, the formation of covalent B-H bonds is proposed. Further information on the adsorption geometry of hydrogen on h-BN was obtained by a normal incidence X-ray standing wave study, which showed that hydrogen does bind to boron and revealed a faint magnetic moment[150].

Hydrogenation leads to strong changes in the electronic structure of h-BN. Theoretical studies addressing the hydrogenation of h-BN and h-BN nano-ribbons show that the electronic properties are highly tunable with hydrogen[151,152]: For semi-hydrogenated h-BN a smaller bandgap is predicted than for non-hydrogenated h-BN, and the properties of nanoribbons might be tunable, from non-magnetic to magnetic, and from insulating to metallic.

A second possibility for the interaction of hydrogen with supported h-BN is intercalation that is, the formation of a hydrogen layer between h-BN and the supporting substrate. Hydrogen intercalation was indeed found, e.g., for the h-BN/Rh(111)[153] and h-BN/Pt(111)[79] systems. Intercalation studies carried out for graphene on various substrates in the past showed that intercalation can significantly influence the electronic properties of 2D layers, which are also termed two-dimensional adsorbates[154–157]. Furthermore, for graphene it was shown that the substrate plays a key role for hydrogenation. This is because the interaction between a 2D adsorbate, like graphene, and a substrate determines the amount of stored hydrogen, the structural arrangement of the stored hydrogen, the release temperature, and even if intercalation of hydrogen is possible at all[44, 64, 129,158].

Despite the relevance of h-BN and the structural and electronic similarities to graphene, the possible intercalation of hydrogen between h-BN and its substrate is still mostly unknown and was not studied on the Ni(111) surface so far. Herein, we report on the reactivity of h-BN towards atomic hydrogen on a Ni(111) single crystal over a wide exposure range. The investigations characterizing the reaction of h-BN with atomic hydrogen are carried out with high resolution XPS and NEXAFS. The thermal stability is studied with TPXPS, temperature-programmed desorption (TPD) and NEXAFS. From our systematic approach with different atomic hydrogen exposures, we obtain detailed insight into the reaction of atomic hydrogen with h-BN/Ni(111) and the dependence of the reaction on the atomic hydrogen exposure. Density-functional theory (DFT) results assist in the assignment of structural arrangements and clarify the geometries of h-BN/Ni(111) and the hydrogenated species. In addition, the electronic structure of the newly formed hydrogenated species is analyzed and compared with pristine h-BN/Ni(111) and free-standing h-BN in vacuum, showing that the dominant species that is, hydrogen-intercalated h-BN/H/Ni(111) electronically corresponds to free-standing h-BN. The weakened interaction towards the surface is also in line with the theoretical analysis of the adsorbate-substrate bands for all systems and in agreement with UPS experiments.

The exposures are calculated from the background pressure in the chamber and the exposure time. However, as the pressure on the sample cannot be measured directly, the absolute exposure is unknown; it depends on the distance between the sample and the capillary of the hydrogen source. For the TPD-apparatus, the distance between sample and capillary is larger; thus, the used exposures are higher by a factor of ~5 to 10 compared to the exposures used in the two-chamber setup for synchrotron-based XPS. Notably, above exposures of 140 L, tungsten oxide was observed in high-resolution XPS, which is attributed to oxygen impurities in the hydrogen gas bottle. The oxide is stable to above 750 K. Since molecular oxygen does not react with h-BN on Ni(111) at the adsorption temperature of 170 K, we assume that small amounts of atomic oxygen are also produced in the hydrogen cracking source, resulting in tungsten oxide coverages of up to 0.1 ML.

4.2 Computational Details

The experiments were accompanied by DFT calculations conducted by J. Gebhardt from the working group of Prof. Dr. A. Görling. In the following the computational details are given.

Spin-polarized DFT calculations were carried out for slab models with the Vienna-ab initio-simulation package[159], employing a plane wave basis set up to a converged kinetic energy threshold of 415 eV, and the projector-augmented wave method[160] for the description of core electrons. The applied Perdew-Burke-Ernzerhof exchange-correlation functional[161] was supplied with the D3 correction[162] (including Becke-Johnson damping[163]) to account for dispersive interactions. Energies and geometry optimizations were converged to 10^{-6} eV and until forces acting on ions were below 0.01 eV/Å. Vacuum layers of 10 and 18 Å were employed for freestanding h-BN and h-BN on Ni(111), respectively. The latter was modeled by placing a h-BN sheet on an optimized nickel slab representing the (111) surface. A slab model with six layer thickness was chosen, fixing the bottom three layers to their bulk positions. The Brillouin zone was sampled by 19×19×1 k-point grid[164] for (1×1) cells, and a reduced 2 × 2 × 1 grid in the larger (4×4) unit cell. A dipole correction[165] was employed in order to correct for the finite size of the slab along *z*. Different h-BN arrangements on Ni(111) were computed in the smaller (1×1) unit cell, whereas hydrogen adsorption was considered in the larger (4×4) unit cell, allowing coverages down to 1/16 ML . In order to account for the metallic character of the substrate-supported systems, a first order level broadening according to Methfessel and Paxton[166] with $\sigma = 0.15$ eV was employed. For the free-standing cases, a reduced half-width of 0.05 eV was used. Adsorption energies are defined as $E_{ads} = (E(ads/Ni(111)) - E(ads) - E(Ni(111))/M$ that is, the energies of the isolated adsorbate (ads) and the Ni(111) surface are subtracted from the combined system, and are given per atom of the h-BN sheet in the computed cell (M=32). Charge-density differences (CDD) where computed analogously that is, by subtracting the densities of the isolated adsorbate (hydrogenated (H) h-BN) and the isolated surface from the density of the combined system. Similarly, hydrogenation energies per hydrogen atoms are defined as $E_{hyd} = (E(nH/h\text{-}BN/Ni(111)) - E(h\text{-}BN/Ni(111)) - nE(H))/n$ that is, subtracting the energy of the pristine h-BN/Ni(111) sheet and a hydrogen reference energy from systems that are containing *n* hydrogen atoms (either adsorbed on the h-BN sheet or intercalated between h-BN and Ni(111)). As hydrogen reference, we chose a single hydrogen atom, in accordance to the experimental procedure.

4.3 Results and Discussion

Structure of h-BN on Ni(111)

A 2D hexagonal adsorbate layer can form two classes of high symmetry arrangements relative to a commensurable (111) surface of a face-centered cubic crystal. The first consists of the "on top" arrangements (Figure 4.1a), with one adsorbate sublattice adsorbed on top of a first layer substrate atoms (top sites) and the other sublattice over fcc or hcp hollow sites. The alternative "bridged" arrangements can be constructed by laterally shifting the 2D lattice relative to the surface, leading to structures where adsorbate-adsorbate bonds are bridging the high symmetry sites (top, fcc-hollow, and hcp-hollow) of the surface[50]. Consequently, top and bridged arrangements are denoted according to the surface sites that the adsorbate atoms or the adsorbate-adsorbate bonds, respectively, are located on. For graphene on Ni(111), it was shown that the top-fcc and the bridge-top arrangements represent the thermodynamical minimum, with both structures being practically isoenergetic[50,167]. Similarly, for h-BN two different coexisting adsorption sites were suggested on Ni(111); however, clear experimental proof seems to be missing[52,141]. In principle, three different top and bridged arrangements can be envisioned. Since in h-BN the two sublattices are distinguishable, each structure has two variants, i.e., in total twelve different structures have to be taken into account (Figure 4.1). Herein, we refer to the different structures as X-Y_{AB} with X and Y being an adsorption site, such as, top, fcc(-hollow), and hcp(-hollow) and A and B denoting the sublattice that is adsorbed over these sites (N or B).

During structural optimization, most of the bridged adsorption sites were not stable, transforming into more stable top sites. For the top sites, the most stable geometries have nitrogen atoms located at top site and boron at fcc (Figure 4.2a and 4.2b) or hcp hollow sites. These structures are almost isoenergetic with adsorption energies of -0.27 to -0.28 eV/u.c. This preference of nitrogen over boron atoms adsorbed at top sites is in line with earlier reports[51,168–175]. The resulting adsorption energies and distances are shown in Table 4.1.

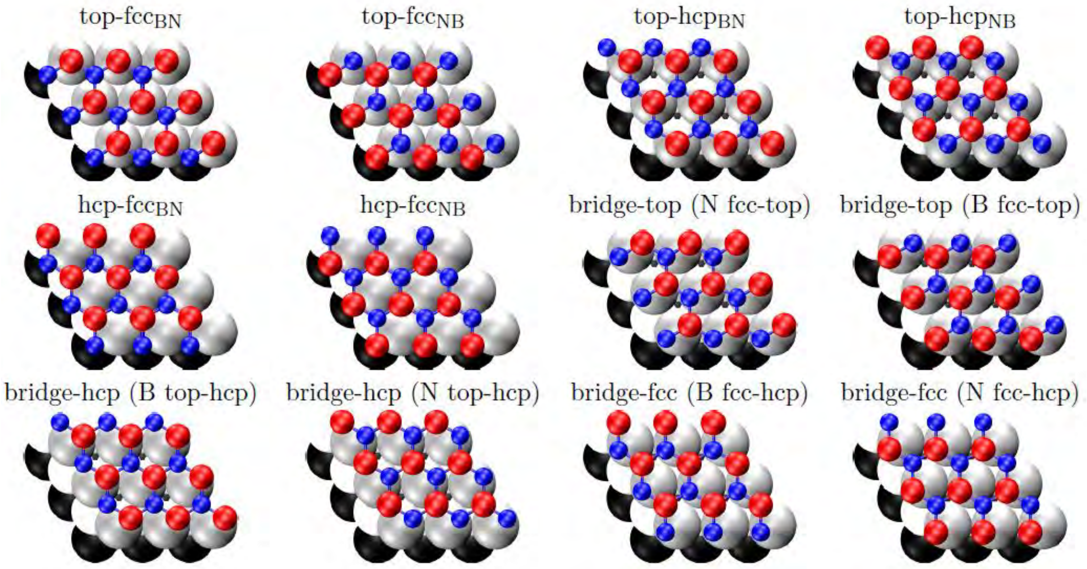

top-fcc$_{\text{BN}}$ top-fcc$_{\text{NB}}$ top-hcp$_{\text{BN}}$ top-hcp$_{\text{NB}}$

hcp-fcc$_{\text{BN}}$ hcp-fcc$_{\text{NB}}$ bridge-top (N fcc-top) bridge-top (B fcc-top)

bridge-hcp (B top-hcp) bridge-hcp (N top-hcp) bridge-fcc (B fcc-hcp) bridge-fcc (N fcc-hcp)

Figure 4.1: Structures of h-BN on Ni(111) discussed in the text. Structures are denoted according to the adsorption positions of adsorbate species or adsorbate-adsorbate bonds on the substrate for on top and bridged structures, respectively. Since the adsorbate species are different, the atomic labels are added as subscript in the order of occupied substrate sites for an unambiguous nomenclature for top arrangements. For bridged structures, the location of one adsorbate species between substrate sites along a B—N bond is specified in brackets. Atoms are represented by black (third row nickel, fcc-hollow site), white (second row nickel, hcp-hollow site), gray (first row nickel, top site), blue (boron), and nitrogen (nitrogen) spheres, respectively.

Adsorption Site	E_{ads} / eV	d_{ads} / Å
top-fcc$_{\text{BN}}$	-0.15	3.2
top-fcc$_{\text{NB}}$	-0.28	2.1
top-hcp$_{\text{BN}}$	-0.15	3.2
top-hcp$_{\text{NB}}$	-0.27	2.1
hcp-fcc$_{\text{BN}}$	-0.15	3.2
hcp-fcc$_{\text{NB}}$	-0.15	3.2
bridge-top$_{\text{BN}}$	→ top-hcp$_{\text{NB}}$	2.1
bridge-top$_{\text{NB}}$	→ top-fcc$_{\text{NB}}$	2.1
bridge-hcp$_{\text{BN}}$	-0.15	3.2
bridge-hcp$_{\text{NB}}$	→ top-hcp$_{\text{NB}}$	2.1

bridge-fcc$_{\mathrm{BN}}$	→ top-fcc$_{\mathrm{NB}}$	2.0
bridge-fcc$_{\mathrm{NB}}$	-0.15	3.2

Tab. 4.1: Adsorption energies and distances for the investigated h-BN/Ni(111) arrangements (see Figure 4.1). Most bridged structures were observed to be unstable, and were transformed to one of the two stable top-hollow sites during relaxation, which is indicated by the notion of an arrow pointing to the final structure.

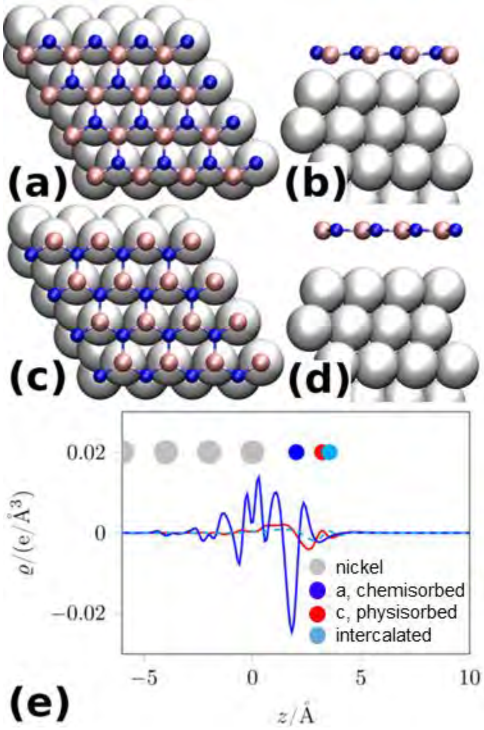

Figure 4.2: (a) Top and (b) side-view of optimized DFT structures of the most stable top-fccNB site (red: boron; blue: nitrogen). (c) Top and (d) side-view of a representative physisorbed geometry top-fccBN. (e) Two-dimensional charge-density difference averaged over the xy plane for the two structures shown in (a-d), showing the effect of the adsorption distance comparing chemisorption (blue) and physisorption (red) on the pillow-effect. In addition, the hydrogen-intercalated species (see below) is included (dashed, cyan). Gray circles indicate the position of nickel atoms along z, whereas blue, pink, and cyan circles indicate the position of the adsorbate layer in the top-fccNB, top-fccBN, and H-intercalated (Hint-fccH) arrangement, respectively.

At first sight, this might be counterintuitive, since the boron atom is expected to interact stronger with the Ni(111) surface due to its electron deficiency, in line with the stronger bonding of boron-vs. nitrogen-doped graphene sheets[176]. However, as the calculations show, the hollow sites are better suited for a stronger boron-nickel interaction, since in this arrangement every boron atom has three surface nickel atoms it can bind to. This is also in line with studies of boron-doped graphene, where boron also preferred the adsorption in hollow sites[176]. This bonding of boron atoms to the surface leads to a small buckling of the h-BN sheet in the stable arrangements, with boron being 0.11 Å closer to the surface than nitrogen. This is accompanied by a charge transfer from the substrate to boron atoms (see below). Averaging over the small buckling in the most stable top adsorption sites, we find a mean adsorption distance of 2.08 Å. All other adsorption sites have a much larger average adsorption distance of 3.15 to 3.22 Å (see e.g. Figure 4.2c and 4.2d. This suggests the existence of two separated minima, one chemisorbed state with a smaller adsorption distance around 2.1 Å and one physisorbed state at a larger adsorption distance around 3.2 Å, in analogy to what was observed previously for graphene on Ni(111) and what was reported earlier for top-hollow adsorption sites of h-BN in the literature[169,171]. For top-fcc hollow and top-hcp hollow adsorption the less stable physisorbed state represents a local minimum with an adsorption energy being 0.12 eV / u.c. higher than that of the corresponding chemisorbed state. As for graphene, the less stable physisorbed state can be obtained when considering different metal substrates[170]. For graphene, we showed in an earlier report[63] that this changed adsorption distance and the accompanied electrostatic effects (the electrostatic surface potential and the pillow-effect) are responsible for the major changes that are observed in the electronic structure of graphene comparing strong interaction with a substrate (chemisorption on Ni(111)) and quasi-free-standing cases (physisorption on Au(111)). For h-BN, this is illustrated in Figure 4.2e, where the charge rearrangement upon the h-BN adsorption to a Ni(111) surface for the chemisorbed and physisorbed adsorption distances is displayed. The pillow-effect is one order of magnitude larger in the chemisorbed case, identical to what is observed for graphene[63].

In summary, we confirm that top-hollow (fcc or hcp) structures with nitrogen atoms at the top site are the thermodynamically most stable arrangements. A second structural alternative was not found, even when considering the energetically most favorable bridged structures that were not included in previous theoretical studies. The less stable physisorbed cases are unlikely to coexist with the chemisorbed state in the same experiment.

4.4 Effects of atomic hydrogen exposure on h-BN

NEXAFS

In Figure 4.3, the NEXAFS spectra after various atomic hydrogen exposures are depicted, for both the boron K-edge and the nitrogen K-edge, at normal and grazing incidence.

The spectra of clean h-BN on Ni(111) show pronounced differences for grazing and normal incidence. The characteristic features are marked with dashed vertical lines at the respective photon energies and are labeled with roman numbers, starting at low photon energy. For the grazing incidence spectra at the B K-edge (Figure 4.3a), we observe two well-resolved features at, 192.4 (I) and 194.2 eV (II), which are more or less absent at normal incidence (Figure 4.3b). On the other hand, the normal incidence spectra show a well-defined peak at 198.8 eV (III; with a low energy shoulder), which nearly disappears at grazing incidence. Similar differences are also found at the N K-edge. From earlier studies[149,177,178] these features are known; (I) and (II) are assigned to the π^* resonances. While (I) is due to the lowest and rather localized unoccupied orbital, (II) is due to the hybridization of the π h-BN states with Ni 4p and 4s states[177], or interlayer states[178]. In a simplified picture, (II) can be assigned to the Ni - h-BN interaction. In a similar manner, the features in the N K-edge spectrum at grazing incidence are assigned: (V) and (VII) are both again associated out-of-plane “interlayer states” due to hybridization, and (VI) is associated with localized π^* states. Feature (V), again in a simplified picture, is a measure for the h-BN substrate interaction. The states measured at normal incidence are associated with transitions to σ^* orbitals; as no strong changes are observed upon hydrogenation, they will not be discussed in more detail. Furthermore, Usachov et al.[97] studied quasi-free-standing h-BN on Ni(111) and minimized the adsorbate/h-BN interaction by the intercalation of gold. Their NEXAFS spectra indeed show a strong similarity to spectra of bulk h-BN[179] that is, a system with weakly interacting h-BN layers. For the B K-edge, they observe one feature at 192 eV at grazing incidence and a doublet at 198 and 199 eV at normal incidence.

Upon exposure to hydrogen, the observed peaks show characteristic changes. At grazing incidence, the two well-resolved features at 192.4 (I) and 194.2 eV (II) in the B K-edge spectra in Figure 4.2a are slightly broadened for an exposure of 1 L. Moreover, we observe a decrease of (I) and an increase of (II) compared to pristine h-BN. For 90 L, feature (I) increases, while (II) decreases compared to pristine h-BN. For 600 L, (I) is dominant, and (II) no longer visible. We interpret these changes as a change in the interaction of h-BN with the substrate. For 1 L exposure, we find an increased interaction, in line with a hydrogenation of h-BN, while for 90 L, we observe the onset of a quasi-free-standing h-BN sheet. For 600 L, the layer is quasi-free-standing, as concluded from the similarity of the spectra to those of intercalated h-BN or bulk h-BN. The normal incidence spectra in Figure 4.3b show a broadening of the feature at 198.8 eV (III) for exposures of 1 and 90 L, while for 600 L a well resolved double peak structure with a new peak at 199.9 eV (IV) is found, again being similar to what is found for quasi-free-standing h-BN.

In the grazing incidence spectra at the nitrogen K-edge in Figure 4.3c, we find three peaks at 400.0 (V), 402.5 (VI), and 403.7 eV (VII), which all change upon atomic hydrogen exposure. At 1 L, only feature (V) becomes slightly more pronounced; at 90 L, feature (VI) increases significantly and is now visible as a distinct shoulder and feature (V) decreases slightly. At 600 L, feature (VI) becomes dominant, while the other peaks decrease, especially feature (V), which was assigned to the h-BN substrate interaction. This data set is again in agreement with the interpretation discussed above: first, an increase in the h-BN substrate interaction indicative of hydrogenation (1 L) is observed. Subsequently, the onset (90 L) of hydrogen intercalation and for higher exposures, the formation of quasi-free-standing h-BN layer (600 L) is deduced. In the normal incidence spectra at the nitrogen K-edge, a broad structure is observed. No significant changes are found up to a hydrogen exposure of up to 90 L. Only at 600 L, a new feature develops at 409.6 eV (VIII), which is similar to results for bulk h-BN.

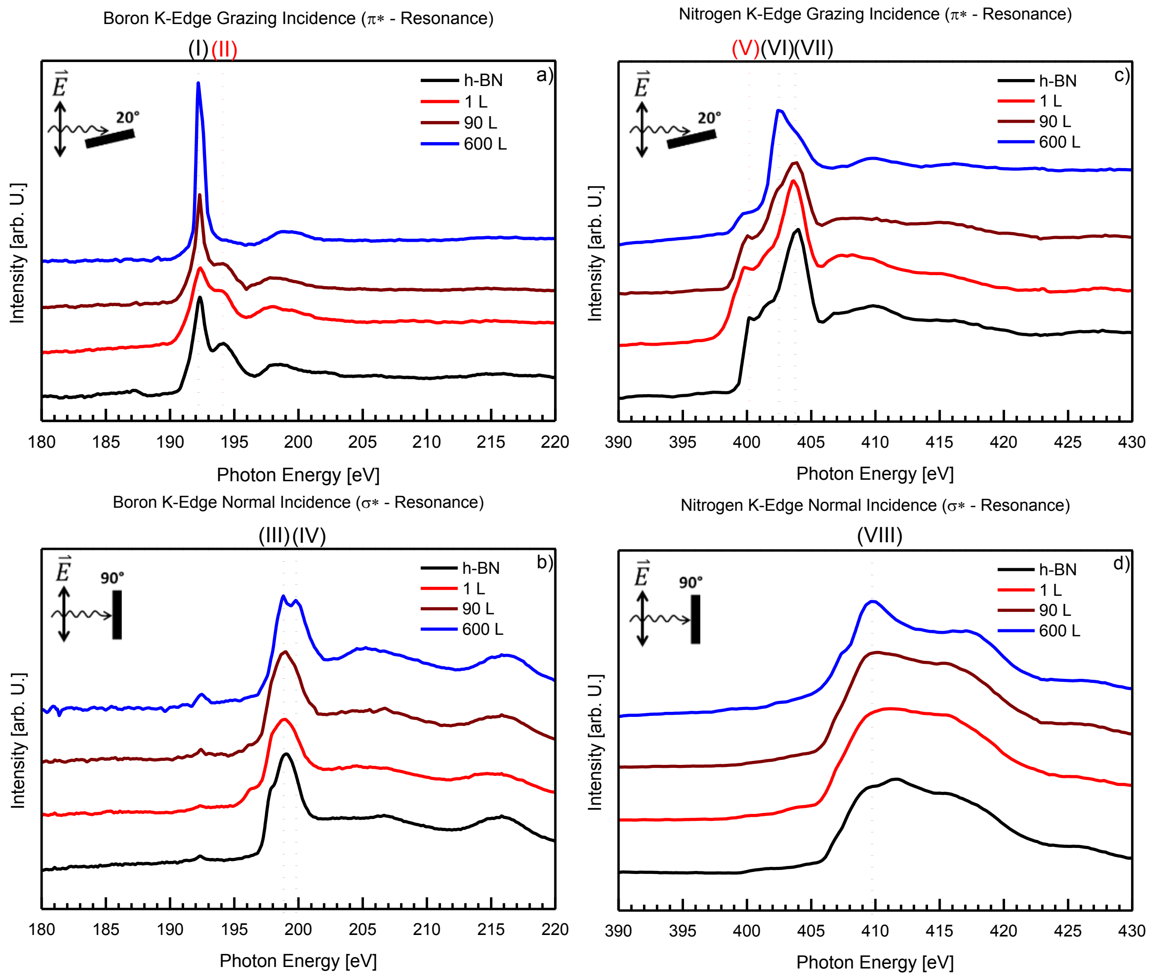

Figure 4.3: NEXAFS spectra obtained for h-BN and h-BN exposed to various amounts of atomic hydrogen. (a) Boron K-edge grazing incidence. (b) Boron K-edge normal incidence. (c) Nitrogen K-edge grazing incidence (d) Nitrogen K-edge normal incidence. Characteristic features are marked with dashed lines. Features characteristic for the h-BN - substrate interaction are labeled in red. The measuring geometry is indicated as an inset in the top left of the figures.

To summarize the conclusions derived from our NEXAFS experiments, we identify two different, exposure-dependent routes of hydrogen to interact with the h-BN/Ni(111) system: For lower hydrogen exposure, we find an increased h-BN/substrate interaction, indicating hydrogenation, and for higher hydrogen exposure, the h-BN/substrate interaction is decreased, indicating intercalation. While hydrogenation along with an increase in the interaction strength with the substrate has already been shown in detail for graphene[42], no intercalation with atomic hydrogen was observed for graphene/Ni(111).

Photoemission

Next, we discuss the XP spectra shown in Figure 4.4. While in NEXAFS only small changes are observed for small exposures, in XPS strong changes are observed already for small exposures. For low exposures of 1 and 90 L, in the B 1s spectra a shift of the h-BN peak at 190.5 eV towards lower binding energy is observed, which goes along with a broadening of the peak. In the N 1s spectra, a more distinct effect is visible for 1 and 90 L: in addition to a decrease and slight broadening of the main h-BN peak at 398.5 eV, a pronounced shoulder emerges at 397.9 eV. The overall amount of both boron and nitrogen remains constant. These changes are associated with the formation of a stronger bond of h-BN with the Ni(111) surface at these low hydrogen exposures, analogously to formation of hydrogenated graphene. Our DFT calculations (see below) show that hydrogen preferentially binds to the boron atoms in h-BN on Ni(111). Interestingly, the hydrogen-boron bond does not lead to a distinct chemical shift in the B 1s core level, which we attribute to a balance of the two opposing effects from weakened nickel-boron interactions and newly formed B-H bonds, i.e. the newly formed bond does not change the total charge at the boron atom.

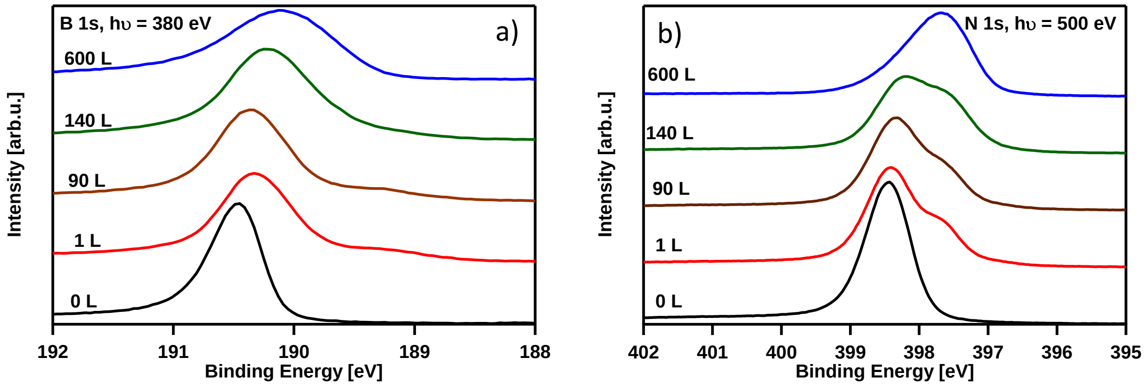

Figure 4.4: XP spectra of h-BN after different exposures (0 – 600 L) of atomic hydrogen in the B 1s (a) and N 1s (b) core level region.

At 600 L, we find a very broad B 1s peak centered at 190.1 eV (i.e. shifted by 0.4 eV relative to the value found for lower exposures; notably, the B 1s shift for Au-intercalated h-BN is slightly larger with 0.7 eV[97]). At the same time, the main N 1s peak has nearly disappeared and is only observable as an asymmetry towards higher binding energy, while the dominant feature is now at a lower binding energy of 397.7 eV. We interpret these spectra, as being due to hydrogen-intercalated h-BN for the following reasons: We find a chemical shift towards lower binding energy, which is very similar to the one observed by Usachov[97] for Au-intercalated h-BN/Au/Ni(111); notably, the N 1s shift is slightly smaller in our case (0.8 eV vs. 1.1 eV for Au-intercalated h-BN). Notably, shifts for CO intercalation were considerably larger (3 and 2 eV for the N 1s and B 1s core levels, respectively)[180]. In a simple picture, these core level binding energy shifts reflect the different electronic structure, i.e. chemical identity and the size of the intercalated species. A more sophisticated model was developed for graphene on Ir(111), where relative shifts upon intercalation of several molecules can be described by a combination of a rigid band model and additionally taking into account the transferred charge[181]. This analysis, however, has not yet been performed for h-BN on a strongly interacting substrate such as Ni(111).

At 140 L, the B 1s spectrum shows a further broadening of the signal towards lower binding energies, as compared to the 90 L situation. In the N 1s spectrum, the shoulder already observed for 1 and 90 L, increased, while the main peak at 398.4 eV decreased. As will be shown below, this is an intermediate case that shows a mixture of intercalation and hydrogenation.

DFT: Atomic hydrogen interacting with h-BN/Ni(111)

In order to gain further insight, we also performed DFT calculations of hydrogenated h-BN. We focus on the stable adsorption arrangement that is, h-BN adsorbed in top-hollow with nitrogen atoms at the top site (top-fcc$_{NB}$, see above). Optimized structures of the discussed hydrogenation arrangements for various coverages are shown in Figure 4.6. In this arrangement, adsorption of hydrogen can occur on either nitrogen or boron atoms. For an isolated hydrogen atom at a coverage of 1/16 ML, we find that boron hydrogenation is favorable by 0.63 eV/H atom as compared to nitrogen hydrogenation, with an adsorption energy of -2.07 vs. -1.44 eV/H, respectively. This adsorption energy is 0.18 eV/H smaller than the one found on graphene carbon atoms. In both adlayers (h-BN and graphene), the energetically most stable hydrogenation site is at the atom in the hollow site. For graphene, the driving force for this was found to be the increased bonding of the neighboring carbon atoms adsorbed in top sites, which move closer to the substrate, inducing a large buckling of the adsorbate sheet. For h-BN, the situation is somewhat different. The atom located above hollow sites is the one that interacts more strongly with the substrate, which is demonstrated by the charge density difference (CDD) for pristine h-BN in Figure 4.5a: Charge is depleted at the nickel surface, mostly from orbitals along z, and is transferred mostly towards the boron atoms in the hollow sites and, to a smaller extent, towards nitrogen atoms and nickel orbitals in the xy plane.

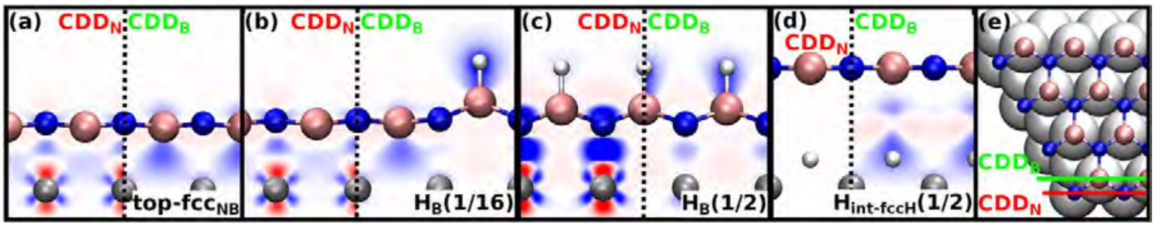

Figure 4.5: Side view on the structures of (a) pristine h-BN/Ni(111), h-BN with hydrogen adsorbed on B with a coverage of (b) 1/16 and (c) 8/16 ML, and (d) hydrogen-intercalated h-BN. Nickel, nitrogen, boron, and hydrogen atoms are indicated by silver, blue, pink, and white spheres, respectively. In addition, the charge-density difference is shown for each case, showing charge depletion (red) and accumulation (blue). In each case, CDDs are shown for planes (see panel (e)) containing nitrogen (CDDN, left) and boron (CDDB, right) atoms, respectively (separated by a dashed line).

This would, at first sight, suggest hydrogenation of nitrogen atoms at top sites, which, however, is not observed. Instead, the boron-nickel interaction is weakened and newly B-H bonds are formed, with boron moving away from the surface. The hydrogenation is accompanied by a rearrangement of atoms along the z-direction (see Figure 4.5b, 4.5c). Boron atoms are lifted away from the substrate, whereas nitrogen atoms are moving closer to the substrate. For the smallest considered coverage of 1/16 ML, this leads to a flat h-BN sheet, with only the hydrogenated boron atom lifted 0.59 Å above the h-BN plane.

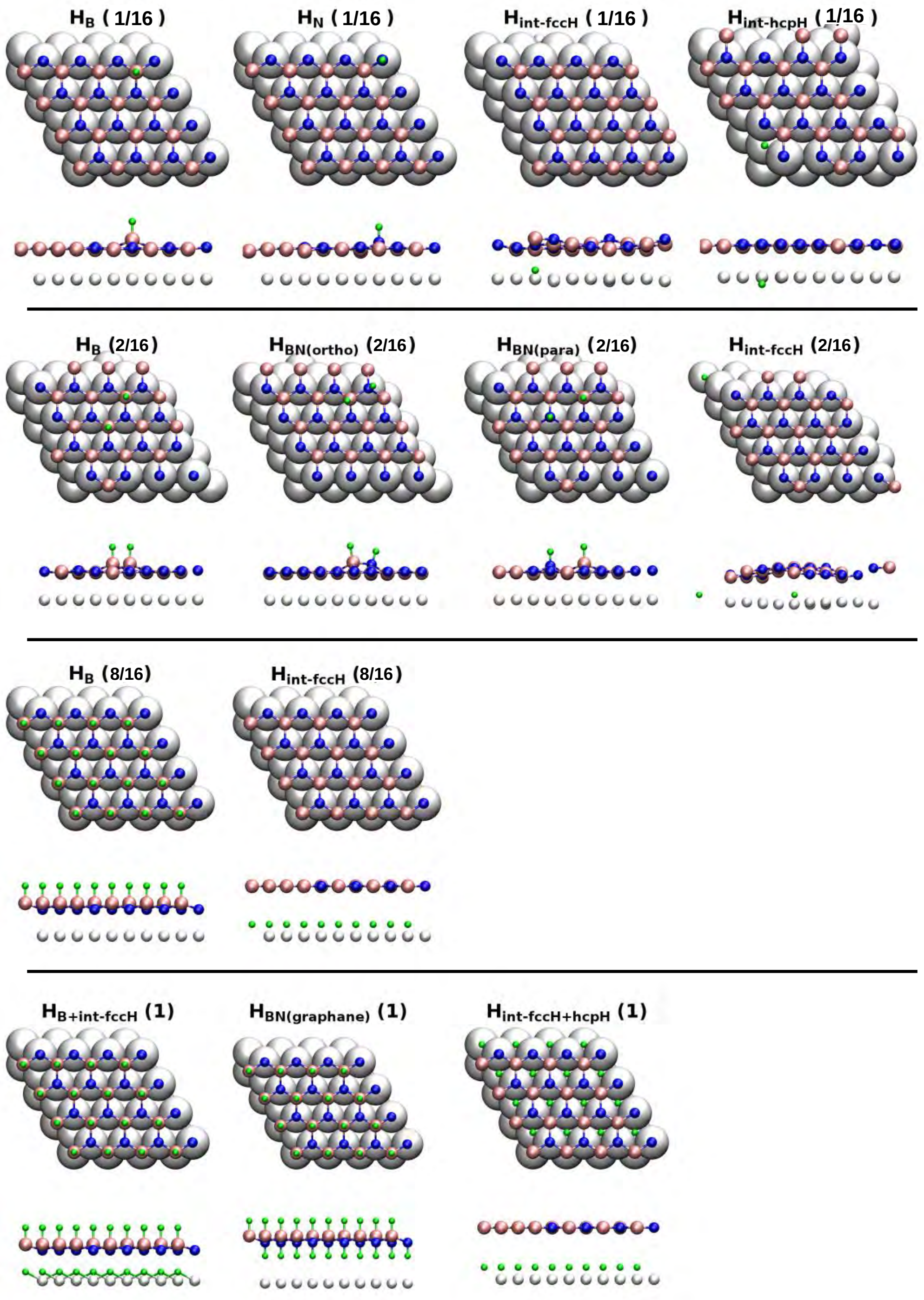

Figure 4.6 Hydrogenated structures discussed in the main text (see Table 4.2).

For a (maximal) coverage of 8/16 ML (1 ML, with respect to the Ni(111) surface), the arrangement strongly changes to a situation with a reversed buckling compared to unhydrogenated h-BN, with nitrogen and boron atoms in adsorption distances of 1.91 and 2.36 Å, respectively. This structural change is accompanied by considerably strengthening the h-BN-Ni interactions, as well as quenching the surface magnetic moment moment. The magnetic moment is quenched by 9 μ _B/u.c., leaving only a small magnetization of ~0.02 μ _B at the nitrogen atoms in the h-BN sheet. The binding energy of the hydrogenated layer to the substrate increases by -0.72 eV/ atom that is, from -0.19 to -0.91 eV/atom, comparing the pristine with the maximally hydrogenated layer (see Table 4.2). This can be explained by the destabilization of a free-standing h-BN sheet that goes along with hydrogenating only boron sites, comparable to graphone, and demonstrates the obtained stabilizing substrate effect for such hydrogenated two-dimensional layers[42]. The magnetic moment is quenched by 9 μ_B/u.c., leaving only a small magnetization of ~0.02 μ_B at the nitrogen atoms in the h-BN sheet. Especially for the maximal coverage, the depleted charge of the nickel surface atoms along z is attributed mainly towards the nitrogen atoms, whereas hydrogenated boron atoms are solely interacting with the bound hydrogen atom. The nature of the h-BN sheet and the inequality of lattice sites (boron and nitrogen atoms) also exclude a possible further stabilization by additional hydrogenation with a second hydrogen atom on the alternating sublattice (adsorption at N sites) on the other side of the h-BN sheet, which was observed in free-standing graphene. For h-BN, such an equal hydrogenation of both sublattices is not stabilizing.

Although it is feasible to hydrogenate h-BN by forming B-H bonds, accompanied by formation of stronger bonds to the surface, intercalation of hydrogen between the h-BN sheet and the nickel substrate is the thermodynamically more stable situation. Already at small coverages of 1/16 ML, the hydrogenation energy of intercalation is favorable by 0.1 eV/H/u.c. compared to B-H formation, with adsorption energies of -2.17 vs -2.07 eV/H/u.c. With increasing coverage, this effect is even more pronounced: while the hydrogenation energy for chemical bonding to the h-BN sheet decreases with increasing hydrogen coverage by 0.85 eV/H/u.c., the energy for intercalation increases, by 0.60 eV/H/u.c. for a coverage of 8/16 ML.

We also considered further structures with even higher hydrogen coverages, such as further intercalation, full hydrogenation at B and N atoms (a graphane analogue[64]) and a mixture of hydrogenation and intercalation. They all show a decrease in the hydrogenation energy by at least 0.6 eV/H/u.c.

The structural arrangement of hydrogen beneath h-BN in intercalated structures is rather insensitive with respect to surface adsorption sites of the hydrogen atoms. Both hollow sites (fcc and hcp) yield similar hydrogenation energies, with the fcc site being more stable by only 0.05 eV/H/u.c. (for a coverage of 1/16 ML). Upon intercalation, the h-BN layer becomes detached from the nickel surface (see Figure 4.5d) with an adsorption distance of 3.60 Å (2.76 Å to the intercalated layer of hydrogen atoms). As a result, no buckling is observed in the physisorbed h-BN layer. Consequently, the interaction to the substrate is weakened, with a low adsorption energy of the boron nitride sheet to the substrate of only -0.07 eV/atom.

Structure (H Coverage/ML)	E_{hyd}/H/eV/u.c.	E_{ads}/eV/atom
h-BN(top-fcc$_{NB}$)	---	-0.19
H_N (1/16)	-1.44	
H_B (1/16)	-2.07	-0.26
$H_{int\text{-}fccH}$ (1/16)	-2.17	
$H_{int\text{-}hcpH}$ (1/16)	-2.12	
H_B (2/16)	-1.93	
$H_{BN(ortho)}$ (2/16)	-1.87	
$H_{BN(para)}$ (2/16)	-1.79	
$H_{int\text{-}fccH}$ (2/16)	-2.21	
$H_{B\ (graphone)}$ (8/16)	-1.22	-0.91
$H_{int\text{-}fccH}$ (8/16)	-2.77	-0.07
$H_{B+int\text{-}fccH(graphone)}$ (1)	-1.60	
$H_{BN(graphan)}$ (1)	-2.05	
$H_{int\text{-}fccH+hcpH}$ (1)	-2.17	

Table 4.2. Hydrogenation energies E_{hyd} of hydrogen atoms at h-BN in different arrangements and various coverages. In addition, the binding energy to the Ni(111) substrate per h-BN layer atom is compared for the most relevant (hydrogenated) h-BN layers as well as the intercalated case.

The weakened interaction to the Ni surface is also manifested in the CDD (Figure 4.4d), which shows only little charge reordering towards the h-BN layer. Especially the charge depletion of the surface nickel atoms is no longer observed. This weak interaction is also in line with our results in Figure 4.2e, which shows a similar physisorption for the hydrogen intercalated system and the physisorbed pristine h-BN sheet. Instead of intercalation of isolated hydrogen atoms, the confined reaction space between substrate and h-BN sheet could also lead to the formation of molecular hydrogen. However, computing an isolated intercalated hydrogen molecule is not observed to yield a thermodynamically stable alternative. Instead we observe the splitting of the H-H bond resulting in the $H_{int-fccH}$ (2/16) structure.

Changes to the electronic structure due to hydrogen adsorption

Next, we want to discuss how the atomic hydrogen exposure effects the electronic structure of h-BN/Ni(111). Figure 4.7a shows the band structures of a pristine free-standing h-BN and 4.7b pristine h-BN on Ni(111). The effect of the substrate is mainly to shift all h-BN bands to larger binding energies by roughly 2 eV, with respect to the Fermi energy, resulting in an n-doping of the h-BN sheet. This is in line with other adsorbate/metal substrate systems and can be attributed to the alignment of the h-BN bands with the Fermi energy of the Ni substrate, which comprises effects from the pillow-effect and the electrostatic surface potential[63]. In addition to this uniform shift of all bands, the π-band exhibits a differential shift due to interactions with nickel bands in the region around 5 eV below the Fermi level. In pristine h-BN, boron and nitrogen s, p_x, and p_y hybridize to sp^2 orbitals, forming three σ bands, similar to graphene. Despite similarities to graphene, subtle differences exist, e.g., the significant downshift of the lowest σ band by roughly 4 eV compared to pristine graphene on Ni(111)[182]. The π bands, on the other hand, are significantly different, with the bonding π band being of mainly nitrogen character, whereas the antibonding π* band is of mainly boron character. This is an interesting difference to graphene, where both carbon sublattices contribute equally to π and π* bands. At the same time, this can be attributed to the differences in electronegativities between boron and nitrogen. Both bands are not approaching each other around K, but are well separated with a band gap of ~5 eV, similar to bulk h-BN[183].

In addition, Figure 4.7 shows UP spectra of h-BN with hydrogen adsorption on boron atoms (c) and hydrogen intercalation (h) that is, for the two arrangements that are observed experimentally after hydrogen exposure to h-BN/Ni(111). Hydrogenation of boron atoms affects the band structure in several ways (Figure 4.7).

All σ bands are shifted towards smaller binding energies by 2-3 eV, without any band hybridization of the hydrogen atoms. This is explained by the chemical effect of hydrogenation on the h-BN sheet. Due to the B-H bond formation and the accompanied charge redistribution that is observed in Figure 4.5c, adsorbate charge pointing towards the surface in pristine adsorbed h-BN is depleted. As a result, the pillow-effect and, thus, the resulting *n*-doping of the Ni(111) surface is weakened, resulting in a partially decreased substrate-induced *n*-doping.

The bonding π-band is almost unaffected, showing only slightly decreased band dispersion compared to the pristine case. The bands with π contribution of the boron atom, however, are now displaying hydrogen character. The band appears downshifted compared to the pristine case, indicating a decreased band gap, but it is interacting with numerous bands of the Ni(111) substrate around the Fermi level. Overall, this suggests that, besides a shift, the σ framework of h-BN remains unchanged upon hydrogen bonding to boron, not supporting the traditional view of a change of boron atoms towards sp^3 hybridization. The p_z orbitals do not admix with the former σ bands, but instead remain unchanged in the case of nitrogen and form a sp hybridized σ band in case of the newly formed B-H bond. For the π–bands, one observes a shift towards lower binding energy by ~0.2 eV in UPS. However, no change in the σ bands around the fermi edge is observable, due to the intense nickel d-bands.

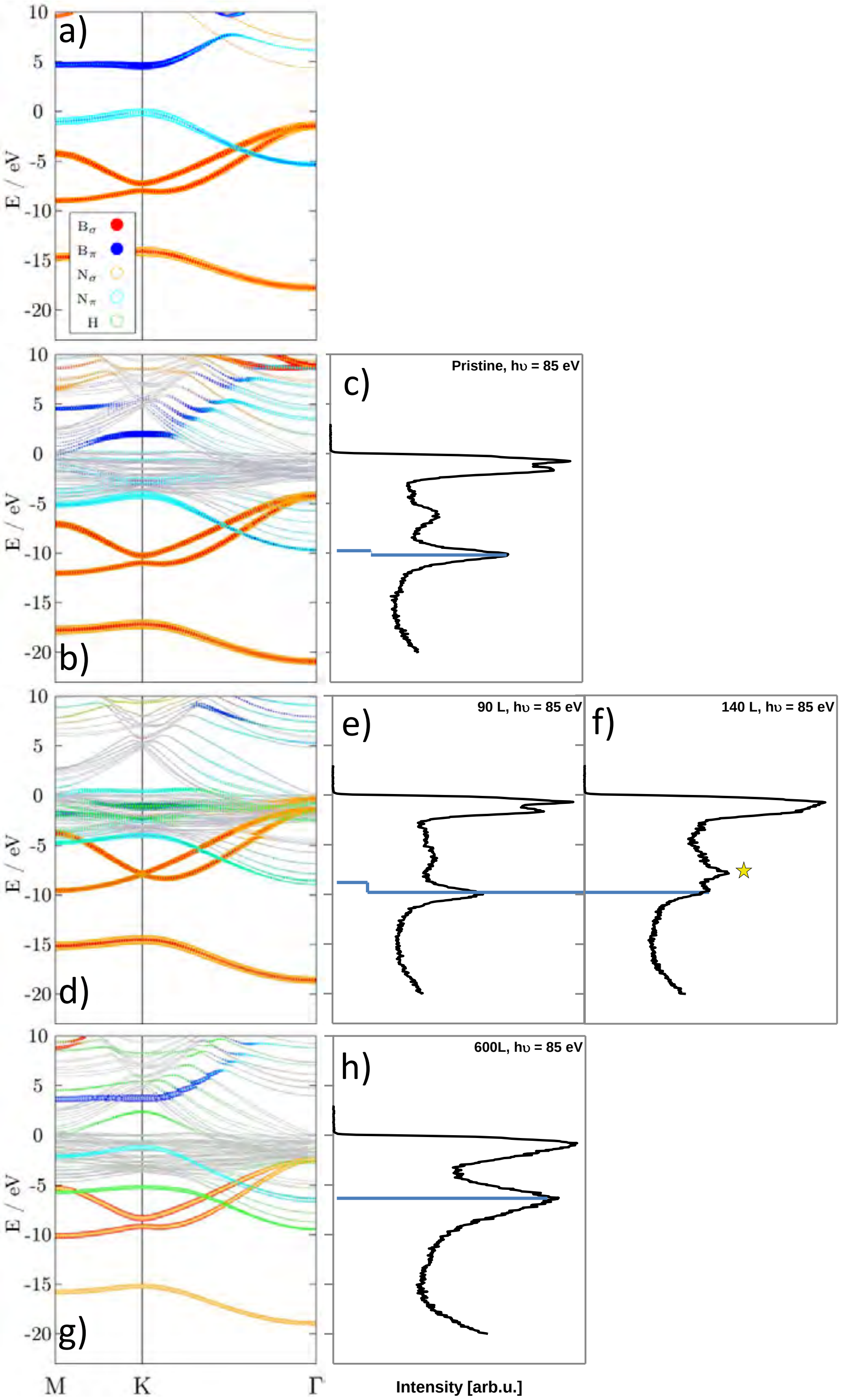

Figure 4.7: Band structure of (a) h-BN free-standing, as well as (b) adsorbed on Ni(111) in top-fccNB adsorption geometry, together with UPS measured at the Γ-point (c). (d) h-BN with hydrogen atoms adsorbed at the boron atoms and UPS data at the Γ-point acquired after a hydrogen exposure of 90 (e) and 140 L (f) (partially intercalated, intercalated contribution marked with a yellow star). (g) with hydrogen intercalating between h-BN and the nickel surface and UPS data after a hydrogen exposure of 600 L (h). Boron and nitrogen σ (red and orange), π (blue and cyan), and hydrogen (green) contribution to bands is indicated by circles, with the size indicating the amount of the contribution.

Finally, we discuss the effect of hydrogen intercalation displayed in Figure 4.7g, h. All h-BN bands appear almost uniformly shifted by ~2 eV towards smaller binding energies, indicating a *p*-doping effect. This is similar to the hydrogenation effect discussed above, but has different reasons. Here, it can be solely attributed to the weakened interaction with the substrate and the resulting increased adsorption distance, as it was demonstrated previously for graphene on metal substrates[54] and proven by the comparison between Figure 4.7a and 4.7b. The π–band is also shifted in the same direction, but by a slightly larger amount. UPS observes the shift of the π-bands well. Similarly, the shift of the π band is observed in the UPS data, showing a value of ~4 eV, in line with DFT. This, again, can be explained by additional hybridizations with nickel bands around the Fermi level that act in addition to the uniformly changed metal doping influence. Thus, hydrogen intercalation is lowering the effect of the substrate, resulting in h-BN bands that are located almost at the energies of the free-standing case This can also be observed, as for the intercalated case a new feature between the two nickel d-bands at the fermi edge is found. In addition to this shift, a new band with hydrogen character arises between -5 and -10 eV. Hydrogen contributions are only found in nickel bands, demonstrating that h-BN is detached and quasi-free-standing, since the influence of the metal is negated, whereas no new interaction with the intercalated layer is observed. The binding energy of the bands in Figure 4.7 c, 4.7e 4.7h is well reproduced in the experiments, with a shift below 0.5 eV. The additional feature in Figure. 4.7c, marked with a yellow star, is due to already intercalated parts of the h-BN sheet, showing the coexistence of both intercalated and hydrogenated domains on the surface, as will also be discussed below. The nearly complete absence of the hydrogen band is well in line with other UPS data, and with the calculated binding energy and the dispersion of the band[184].

Before discussing the thermal stability of our above found two stable configurations (hydrogenation and intercalation), we comment on the difference between DFT and experimental results. From DFT, we expect that hydrogen intercalation is always energetically favorable compared to hydrogenation, and thus should be the dominant structure for all atomic hydrogen exposures. In our UHV experiments, we find hydrogenation for low exposures (< 140 L), while intercalation occurs only for high atomic hydrogen exposures (≥ 140 L). We attribute this to the kinetics of the reactions of atomic hydrogen with h-BN or the Ni(111) substrate. The atomic hydrogen needs to find its way below the h-BN sheet before it can bind to the Ni(111) surface, i.e., before it reaches its energetically favored position (it passes the h-BN mesh likely through defects, as is observed for not closed patches of graphene, were the rim is the defect[185]). However, the probability for a reactive species, such as a hydrogen radical, to form a covalent bond with h-BN is very high. Thus, at low exposures, the hydrogenation of h-BN is more likely than diffusion underneath the h-BN lattice, in order to form the intercalated structure. Once formed, the more stable intercalated h-BN does not allow for the necessary interaction with Ni(111) to form bonds to hydrogen that is, it cannot be hydrogenated. This leads to a removal of hydrogen from the top side of h-BN when h-BN is intercalated, again due to the suppressed h-BN substrate interaction.

Thermal evolution of h-BN exposed to various doses of atomic hydrogen

To further substantiate our findings and to have a deeper understanding of the two possible interaction mechanisms, we conducted temperature programmed experiments, see Figure 4.6.

We will only discuss the results from the N 1s region, since the B 1s core level shows a less distinct chemical shift; see Figure 4.9. The data are plotted in a color-coded density plot, which allows for following the changes with temperature. The starting points of these experiments are the spectra taken after hydrogenation, shown in Figure 4.4. The hydrogenated species with a peak at 397.8 eV remains unchanged up to 470 K. Around this temperature, a peak shift by 0.18 eV to higher binding energies and the disappearance of the shoulder at 397.9 eV is observed, which is attributed to dehydrogenation as indicated in Figure 4.8a. This behavior goes along with an accelerated decrease of the peak intensity above 470 K found in the quantitative analysis in Figure 4.8d (black curve). In Figure 4.8b, the thermal evolution is shown after exposure to 600 L that is, when intercalation has occurred. The corresponding deintercalation is visible as an abrupt shift in binding energy by 1.0 eV at 390 K. This indicates that the intercalated hydrogen has a distinctively different thermal stability. Interestingly, we do not observe any successive dehydrogenation reaction above 470 K. This is again also evident in the quantitative analysis in Figure 4.8d (green curve). The observed behavior leads to the conclusion that no hydrogen can bind to h-BN once hydrogen is intercalated.

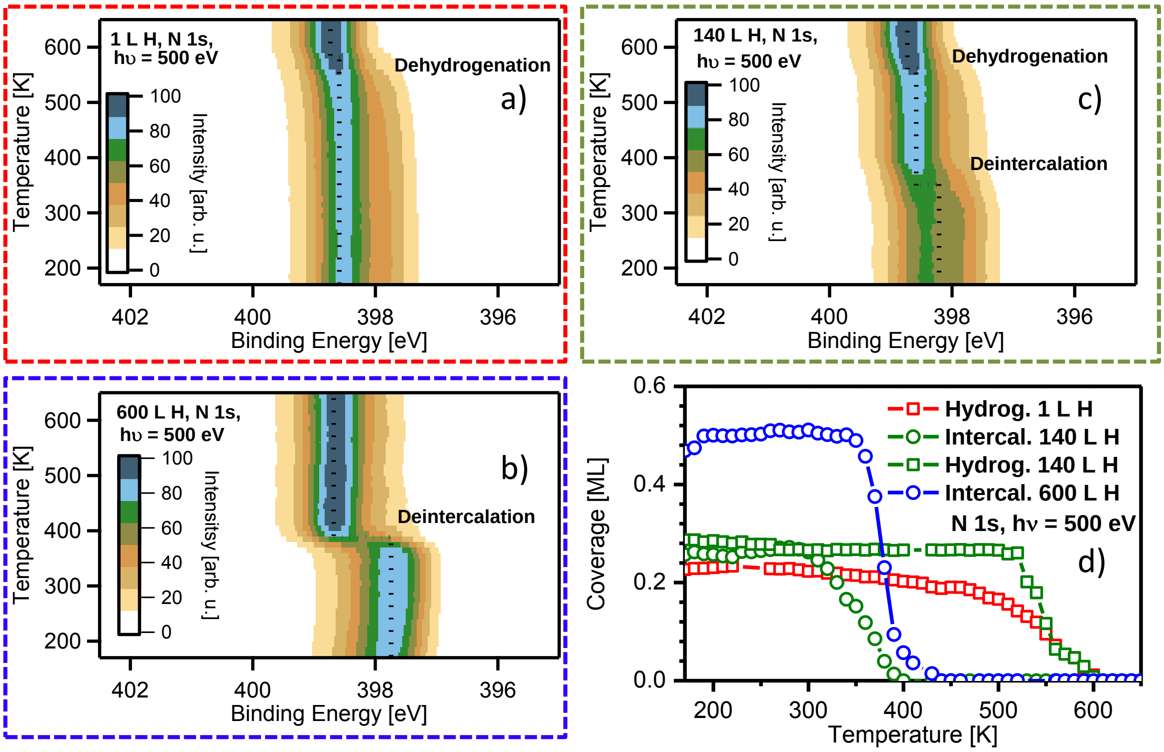

Figure 4.8: Thermal evolution of h-BN exposed to various atomic hydrogen exposures in the N 1s core level depicted as a color-coded density plot, where white is the lowest and dark blue the highest recorded intensity. Exposures of (a) 1 L, (b) 600 L, (c) 140 L, are depicted. Dashed lines are a guide to the eye for the binding energy from the fit. (d) quantitative analysis of (a-c). (T_{ads}=170 K; β=0.5 K/s)

An intermediate case is found for 140 L. Here, both deintercalation and dehydrogenation are observed: During heating, first the intercalated hydrogen desorbs at 390 K, resulting in a first shift of the main intensity, denoted as deintercalation in Figure 4.8c and subsequently, a second shift of the main peak occurs at 550 K, denoted as dehydrogenation. This behavior is also seen in quantitative analysis in Figure 4.8d, where the intensities of intercalated and hydrogenated h-BN are plotted separately (green circles and squares, respectively). This experiment suggests the coexistence of intercalated and hydrogenated parts of the h-BN layer, which we expect not to intermix: The surface interaction in the case of hydrogenation is stronger as the neighboring atoms to the atom that binds to hydrogen will create a stronger surface bond. In the case of intercalation, the opposite behavior is found, leading to a lower interaction. Thus, we propose that in the case of the exposure of 140 L we observe different domains on the surface.

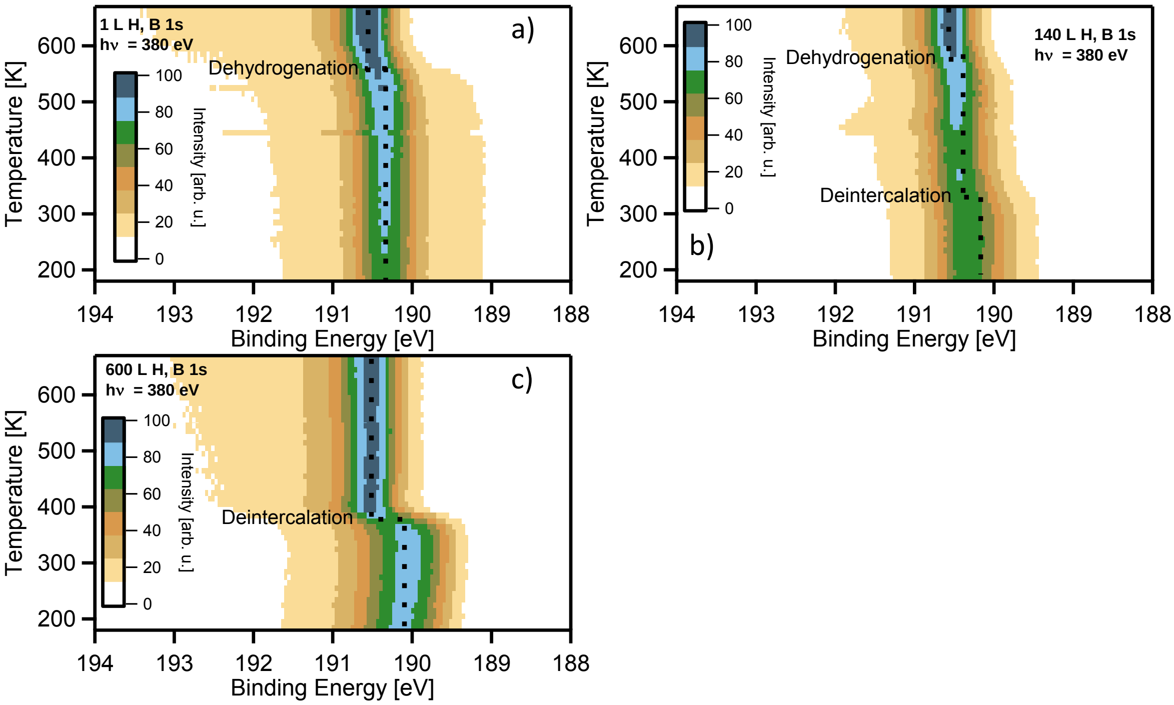

Figure 4.9 Thermal evolution of h-BN exposed to various atomic hydrogen exposures in the B 1s core level depicted as a color-coded density plot, where white is the lowest and dark blue the highest recorded intensity. (a) 1 L, (b) 140 L, (c) 600 L, depicted as a color coded density plot striped lines are a guide to the eye for the occurring reaction.

As a last experimental method, temperature-programmed desorption (TPD) was applied. In Figure 4.10, we show a series of TPD spectra of molecular hydrogen (m/z = 2), collected after increasing atomic hydrogen exposures. Please note that these experiments were carried out in a different apparatus and thus the atomic hydrogen exposures are different, as mentioned in the beginning.

For low exposures, a single peak (γ) is observed at 610 K. This peak increases in intensity with increasing atomic hydrogen exposure, as shown in Figure 4.10a. Additionally, a small peak grows at ~510 K. When increasing the H-exposure, peak (γ) no longer increases, but decreases, as seen from the purple spectrum in Figure 4.10 a for 100 L. Figure 4.10b shows that at even higher exposures peak (γ) decreases further and vanishes

at 1250 L. Simultaneously, above 100 L, a new peak (β) is observed at 390 K, which gains intensity with increasing exposure. Finally, for exposures of 800 L and above, an additional peak at 230 K (α) is observed.

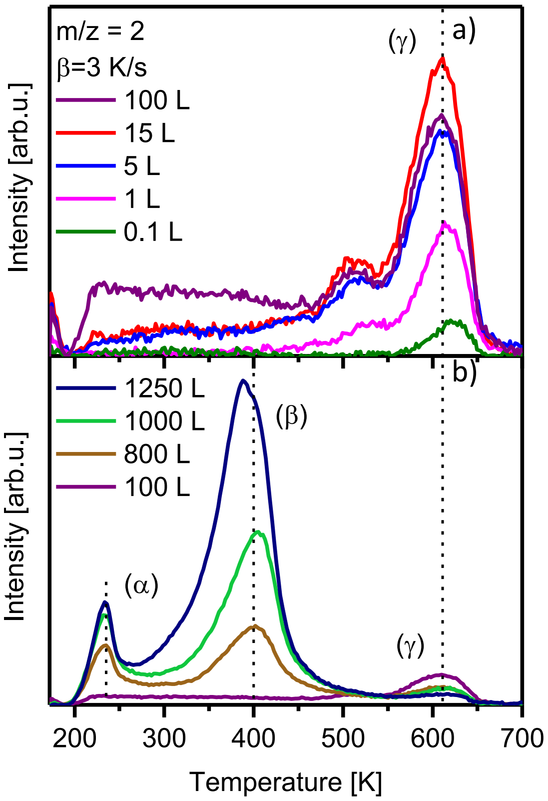

Figure 4.10 TPD spectra recorded after exposing h-BN to various doses of atomic hydrogen. (a) exposures up to 100 L, resulting only in hydrogenation. (b) Larger doses, resulting mainly in intercalation, and the 100 L spectrum shown in a for comparison. (T_{ads}= 180 K; β=3 K/s)

The interpretation of the TPD spectra is well in line with that of the TPXPS experiment: The reaction occurring at higher temperatures that is, the desorption of hydrogen as peak (γ), is due to the dehydrogenation, which only occurs for low hydrogen exposures. We find saturation of this hydrogenation at 15 L. At higher exposures, peak (γ) decreases and finally disappears, in agreement with the TPXPS data. The smaller peak at ~500 K (not labeled) cannot be observed in XPS. Peak (β), fits very well to the deintercalation observed in TPXPS for high exposures. Also, the fact that no dehydrogenation is observed in TPXPS for 600 L atomic hydrogen, fits well to the TPD spectrum of 1250 L (dark blue) that is, intercalation results in dehydrogenation of the h-BN sheet. This again shows that hydrogenation and intercalation are two competing reactions of

atomic hydrogen on h-BN. The TPD peak at lowest temperature, (α), is not observed in XPS. In an experiment with high exposures of molecular hydrogen, this peak is also observed. We thus conclude that it stems from the sample holder and the manipulator.

From a comparison to H_2-TPD spectra from literature,[186] and from our group with the same heating rate of 3 K/s (see Figure 4.11), we find that the desorption temperature on bare Ni(111) is lower by ~30 K than for the "confined" geometry under the h-BN layer (Figure 4.10b). This is in contrast to what is found for other intercalated molecular species[80,187]. While in our calculations the bonding to hydrogen is considerably weakened (1.57 eV/H atom) by the confinement, as it was also found for other adsorbates under 2D materials, the formation of the intermediate "H_2 under h-BN" is very unfavorable and we did not find such an intermediate as semilocal minimum in our calculations (see above). Possibly also kinetic effects such as diffusion barriers of hydrogen under h-BN might unfavorable thus leading to a higher desorption temperature for hydrogen on h-BN/Ni(111) as compared to on clean Ni(111).

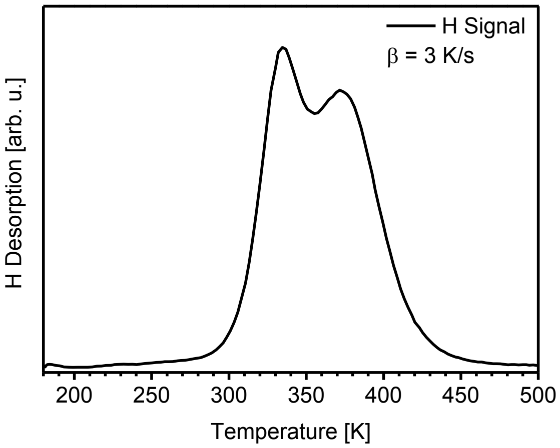

Figure 4.11 TPD of hydrogen adsorbed onto Ni(111) measured with a heating ramp of 3 K/s, with the same apparatus as the TPD data depicted in Figure 4.10.

The experimental results for hydrogen desorption deviate from the stabilities predicted by DFT, since the more strongly bound intercalated hydrogen species is observed to desorb first. This indicates that reaction kinetics dominate the desorption processes. This can be understood since hydrogen has to recombine to molecular hydrogen in order be able to desorb. For hydrogenated h-BN, this process is likely to have a considerable energy barrier (compare the dehydrogenation mechanism of hydrogenated graphene[42]), especially if hydrogen atoms are not directly adsorbed next to each other that is, dehydrogenation does not occur from nearest neighboring sites. In such a case, large diffusion barriers are expected for lower coverage, because nitrogen sites, which are shown to be unstable for hydrogenation, have to be bridged.

4.5 Conclusions

We have studied the reaction of h-BN on Ni(111) with atomic hydrogen and subsequently the thermal stability of the system. High resolution XPS, NEXAFS, and UPS were applied to gain a basic understanding of the system; DFT provide detailed insight into the specific geometrical arrangements of pristine, hydrogenated and intercalated species. We find two different competing regimes of interaction of hydrogen with h-BN; the first is a chemical bond formation for low exposures that is, hydrogenation of h-BN, similar to the behavior previously observed also for graphene. The other regime is intercalation of atomic hydrogen, which lifts the interaction of h-BN with the substrate, resulting in new features in both NEXAFS and photoemission experiments. Our calculations show that these two chemical modifications have different effects on the electronic structure of h-BN. In both cases, the interaction with hydrogen decreases the n-doping effect of the surface. In the case of intercalation, this is due to a larger adsorption distance, leading to quasi-free-standing h-BN. In the case of hydrogenation, B-H bond formation is observed, which is accompanied by charge redistribution and a change of the buckling of the adsorbed h-BN sheet. These changes reduce the adsorbate charge near the surface, leading to a reduced pillow-effect and, thus, a similar raising in energy of the σ bands. Intercalation and hydrogenation lead to two opposite interactions with the surface. While intercalation leads to a less strongly bound h-BN, the opposite is observed for hydrogen bonding to h-BN. The π bands react differently due to the imposed changes of the chemical structure. Subsequently, the thermal stability of the systems was probed with TPXPS and TPD. We find different thermal stabilities for hydrogenated and intercalated h-BN, with dehydrogenation occurring at 550 K and the deintercalation occurring and 390 K.

The following chapters now will move away from atomic hydrogen as the reaction partner of the 2D materials and move to a second, small molecule that is molecular oxygen albeit supplied from the supersonic molecular beam.

5 Oxygen adsorption on h-BN/Ni(111) at 290 K

This chapter also contains theoretical calculations that were conducted by the working group of Prof. Dr. Andreas Görling from the Chair of Theoretical Chemistry at the Friedrich-Alexander-Universität Erlangen-Nürnberg

In this chapter, the adsorption of highly energetic oxygen on h-BN was investigated with temperature programmed XPS and NEXAFS. The interpretation of the data is further supported by DFT calculations: Upon exposure to highly energetic oxygen a single oxygen species develops in the O 1s core level, observed with in-situ high resolution XPS. This species is interpreted as the formation of covalent oxygen boron bonds in an activated adsorption process. The formation of this molecular oxygen species goes along with a weakening of the oxygen-oxygen bond. A shift of both the B 1s and the N 1s signal of h-BN to lower binding energy is observed. The N 1s signal of h-BN further splits into two contributions, which amount for the same coverage. Valence band measurements show that the bands of h-BN are also shifted to lower binding energies. NEXAFS measurements for the nitrogen and boron K-edge show that the h-BN-Ni(111) interaction has increased. Angle dependent NEXAFS measurements at the oxygen K-edge show that still both a π* and σ* contribution are found, indicating that the oxygen-oxygen bond from molecular oxygen is still present. With DFT calculations, a transition state is found confirming that the adsorption of oxygen on h-BN is an activated process. Temperature programmed XP experiments show that oxygen desorbs at 580 K.

5.1 Introduction

Hexagonal boron-nitride (h-BN) is a honey comb arranged alternation of boron and nitrogen atoms, forming a 2D single crystal. As with graphene and graphite, its properties differ greatly from the 3D layered material. E.g. the band-gap of h-BN decreases to 5.4 eV, as a 2D material[52, 141,169]. Similar to graphene, h-BN is believed to be inert[147], possess a high strain endurance[140,188] and also a peculiar electronic structure. The large band-gap of h-BN is very intriguing, in that it is an insulator with a bandgap of 5.4 eV[77,142] and thus a possible deep UV-light emitter, whereas graphene, of which it is a structural and isoelectronic analogue, is a semi metal with a Dirac cone, and thus has no band-gap. Interestingly graphene can be readily grown on top of h-BN[97]. However, the use for 2D materials is still largely limited to fundamental research. Possibly, as only the pristine, free-standing 2D material has the interesting properties described above. However, by using the right substrate or functionalization it may be possible to enable bandgap tuning at will. However, introducing functional groups in large scale or with high purity is still difficult. Thus previously, mostly intercalation was explored. For graphene, already numerous studies are found in literature[181,189–193]. From group one in the periodic table, with alkali metals[194], as well as hydrogen[195], up to noble gases[196]. For h-BN such examples are more scarce[153,197,198]. Regarding the intercalation of 2D materials, it was found that the stronger the interaction of the 2D material with its substrate is the more difficult intercalation is to achieve. Moreover, due to the above described inert character of graphene and h-BN chemical functionalization of the pristine starting material is still in its infancy. Only bulk functionalization of graphite to graphene-oxide (GO) was investigated in detail, as GO is solvable. However, GO and reduced GO often have little to do with graphene. However, besides hydrogenation, no study on the functionalization under defined ultra-high vacuum (UHV) conditions of h-BN/Ni(111) was carried out to our knowledge. However, numerous theoretical studies show that oxygen functionalization should be possible[172,199,200] on Ni(111).

In the following we will discuss the interaction of h-BN on Ni(111) with molecular oxygen as determined by XPS, NEXAFS, UPS and DFT. We show that, for the first time the activated adsorption of oxygen on h-BN has been achieved. We prove that the oxygen-oxygen bond is still present, and that the oxygen-boron bond shows high stability, as deduced from temperature programmed experiments. We believe, that with this experiments, a first true step towards the metal-free CO oxidation catalyzed by h-BN was made[200]. A comparison to graphene on Ni(111) will be given, where no functionalization with oxygen was found under similar experimental conditions.

The amount of oxygen is referenced to XP spectra of the well-known LEED structures of 0.25 ML O_2 on Ni(111)[201], collected with our setup at the same photon energy and sample geometry. The samples measured with the Al Kα X-ray source were referenced to the known LEED structure of 0.5 ML of CO[202].

5.2 Computational Details

The experiments were accompanied by DFT calculations from Himadri Soni of the working group of Prof. Andreas Görling. The computational details are given below.

We have used spin-polarized density-functional theory (DFT) as implemented in the Vienna Ab initio Simulation Package[159], which employs a plane-wave basis set and the projector augmented-wave method[160]. The applied Perdew-Burke-Ernzerhof exchange-correlation functional[161] was supplemented by the D3 van der Waals correction[162] (including Becke-Johnson damping)[163] to take dispersive forces into account. An energy cutoff of 415 eV was used in conjunction with a Methfessel Paxton smearing[166] of order one with 0.15 eV half-width. Vacuum layers of 18 Å decouple periodic images from each other along the z direction. The Brillouin zone (BZ) was sampled by 11 × 11 × 1 Monkhorst-Pack k-point grids[164] for hexagonal (2 × 2) unit cells of hexagonal boron nitride (h-BN) on Ni(111) surface. Electronic structures and geometries were converged below 1×10^{-6} eV and 0.01 eVÅ^{-1} with respect to total energies and forces acting on ions, respectively. We have considered six layers of the nickel substrate, keeping the bottom three layers at their bulk position. This setup was shown to provide good results in our previous work[139]. A dipole correction was employed along z in order to correct for the finite size of the slabs.

Oxygen adsorption energy E_{ads} per oxygen molecule is calculated according to the formula given below:

$$E_{ads} = \left(E_{tot} - E_{(BN/N)} - \frac{N}{2} \circ O_2\right)/N$$

where, N is the number of oxygen molecules adsorbed. For reference, we use oxygen molecule O_2 in gas phase, in accordance with experimental procedure. $E_{BN/Ni}$ is the total energy of the pristine h-BN/Ni(111).

Transition states (TS) where calculated using following procedure: First, a climbing-image nudged-elastic band (NEB)[203] search was performed with reduced optimization parameters, the k-point set was reduced to the Γ-point. The highest energy image (out of three to five images) was taken as initial guess for a dimer search[204], optimization parameters, and k-point grids as in the optimization runs described above. All local minima and first order transition states were verified by vibrational frequency analysis.

5.3 Results

Dependence of the coverage on the kinetic energy of oxygen

Prior to this study, the covalent bonding of oxygen to h-BN was a purely theoretical prediction. This was due to the fact that the adsorption of oxygen on h-BN is an activated process. To overcome the activation barrier for adsorption, we used the supersonic molecular beam with a heatable nozzle. We exposed the h-BN layer on Ni(111) to ~117 L oxygen (O_2) with kinetic energies of up to 0.7 ± 0.2 eV eV at 290 K, and subsequently recorded XP-spectra in the O 1s region. The oxygen coverages obtained from these O 1s spectra are shown in Figure 5.1.

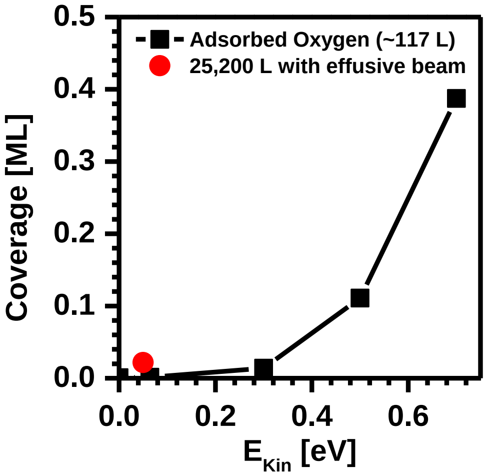

Figure 5.1 Oxygen coverages after exposing h-BN to molecular oxygen with various kinetic energies; also shown is the coverage obtained after exposure to 25,200 L of oxygen from the effusive beam described in the experimental section; the oxygen coverages were determined from O 1s XP spectra measured in the lab in Erlangen, using a conventional Al Kα source.

We observe that the oxygen coverage strongly depends on the kinetic energy of the impinging O2 molecules. At energies below 0.3 eV, only very small coverages are achieved. Only when increasing the kinetic energy to 0.5 eV and beyond, we observe significant oxygen amounts on the surface. For 0.7 eV, the highest kinetic energy that can be reached with our setup, the highest coverage of ~0.4 ML is found. The observed behavior clearly proves the activated nature of the chemisorption of a molecular oxygen species on h-BN on Ni(111). For comparison, we performed an experiment with an exposure of 25,200 L from an effusive molecular beam, i.e. at a 200 times higher exposure than in the molecular beam experiments. Such a high dose leads to only ~0.03 ML of oxygen on the sample (red data point Figure 5.1). This value is similar to the amount found after exposing h-BN to ~117 L of oxygen with a kinetic energy of 0.3 eV. It is attributed to oxygen molecules at room temperature with a Maxwell-Boltzmann distribution of which a small fraction have sufficient energy to overcome the activation barrier. Notably, such high exposures typically go along with contamination from the residual background pressure in the chamber.

High resolution O 1s in-situ photoemission

To study the activated adsorption process of molecular oxygen on h-BN, we collected O 1s XP spectra *in situ* during O_2 exposure onto h-BN at a substrate temperature of 290 K. We will focus on results obtained with a kinetic energy of $E_{kin} = \sim 0.7$ eV, because this incident energy leads to the highest oxygen coverage.

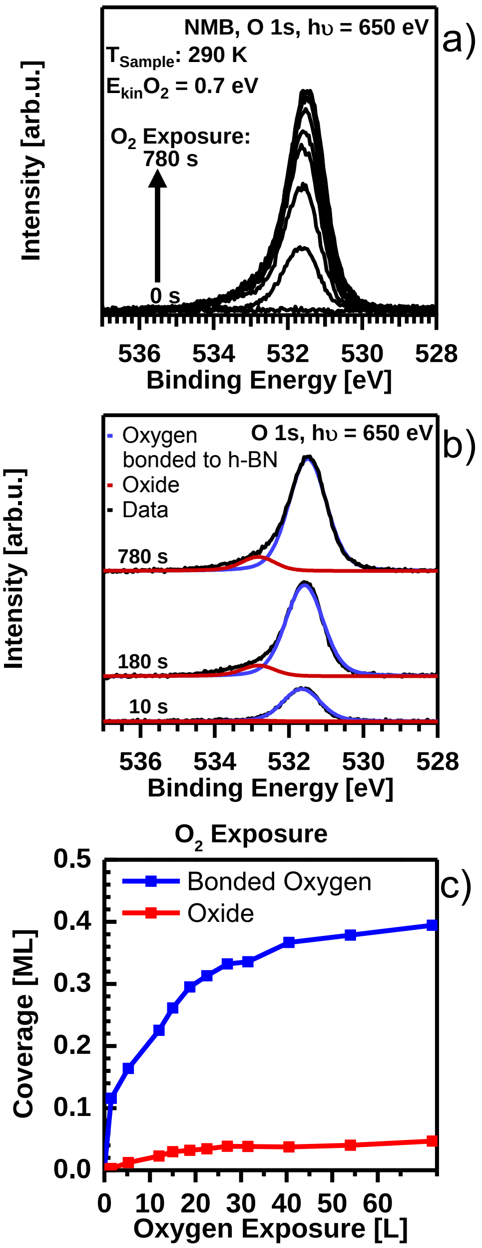

Figure 5.2 (a) spectra obtained during exposure of h-BN to high energetic oxygen, at 290 K sample temperature. (b) fits of selected spectra, depicted in (a). (c) quantitative analysis of the experiments performed, depicted in (a). All data recorded in NMB-geometry as described above.

In Figure 5.2a, we show the corresponding O 1s spectra, along with selected fits to the data in Figure 5.2b. During exposure to O_2, we observe the growth of an O 1s peak 531.6 eV, which slightly shifts to 531.5 eV with increasing oxygen coverage. The quantitative analysis in Figure 5.2c reveals a rapid initial increase in coverage for the first 30 L. It is followed by a more gradual increase, until a coverage of ~0.4 ML is obtained after 72 L. Peak fitting reveals a weak shoulder at 533 eV; in different experiments its coverage varies slightly, but is always less than 10% of the main peak (Figure 5.2c, red). It is assigned to oxide species on the surface. No evidence for further contributions are observed. To ensure that no reaction takes place after switching off the SSMB, we collected spectra for an additional 300 s after the end of the exposure, but observed no further changes (not shown), demonstrating that the achieved oxygen functionalities are stable at 290 K.

Changes to the core-levels of h-BN upon oxygen adsorption

After the adsorption experiment, we recorded the B 1s and N 1s spectra shown in Figure 5.3a and 5.3b to investigate the changes of the h-BN layer upon oxygen functionalization. For these measurements, the sample was rotated such that the surface normal pointed to the energy analyzer. The XP spectra prior to O_2 exposure (Figure 5.3, green) are characteristic of h-BN. They show a single B 1s peak at 190.5 eV with a small shake-up satellite at 193.4 eV, and a single N 1s peak at 398.8 eV.[97,139] Upon exposure to oxygen at 290 K, the main B 1s peak increases in width and shifts to 190.0 eV (Figure 5.3a, blue) and develops a shoulder at 191.1 eV (red) which is assigned to an oxidized minority species. Peak fitting also shows that a small amount of the original h-BN peak is still present, indicating the h-BN is not fully covered by oxygen (see also UPS spectra below).

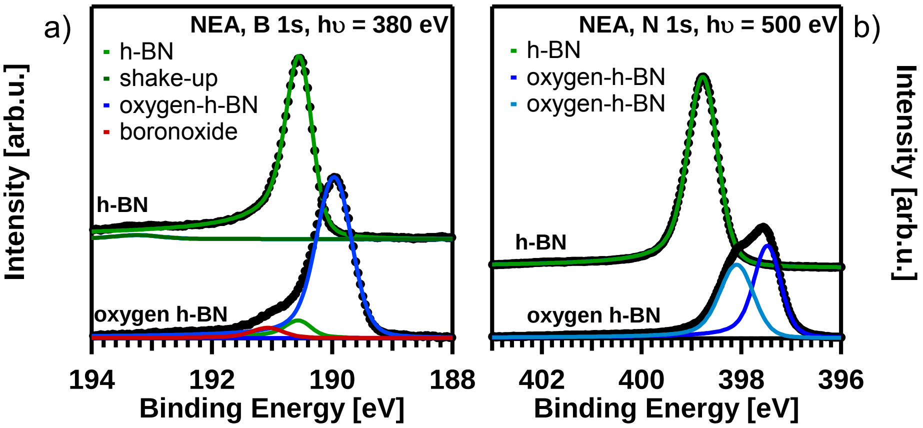

Figure 5.3 Spectra obtained in the (a) B 1s and (b) N 1s region. Top: pristine h-BN; bottom: oxygen bonded to h-BN

In the N 1s region, the sharp peak of pristine h-BN at 398.8 eV (Figure 5.3b, dark green) vanishes upon oxygen exposure at 290 K and two new contributions at 397.5 (dark blue) and 398.1 eV (light blue) are observed. Both account for roughly 0.5 ML nitrogen, confirming that no nitrogen was lost during the adsorption.

NEXAFS

To obtain further information, we recorded NEXAFS spectra at the boron, nitrogen and oxygen K-edges; see Figure 5.4. The spectra of pristine h-BN on Ni(111) agree very well with literature[62, 97,98, 139,149]. At the B K-edge, the dominating peak a_0 lies at 191.9 eV, and the σ* transitions of h-BN are observed as two peaks at 197.3 and 198.3 eV. At the N K-edge, h-BN shows one main feature at 402 eV, which is associated with a π* transition, and the σ* transitions are found from 405 to 417 eV. In addition, so-called interlayer states were assigned to the interaction (hybridization) of h-BN with the Ni(111) substrate.[62, 98,149] We have marked their photon energy ranges with red double-arrows in Figure 5.4a and 5.4b. These states have π*-character and lie parallel to the h-BN sheet. At the boron K-edge, they manifest themselves as a broad feature from ~193 to 195 eV. At the nitrogen K-edge, they are typically found between ~397 and 399 eV[62, 98,149], with a maximum at ~398 eV. These interlayer states and the a_0 peak have been interpreted as indicators of the interaction strength of h-BN with the substrate: a large a_0 peak and weak or vanishing interlayer states indicate quasi-free-standing h-BN[139, 149,177,178].

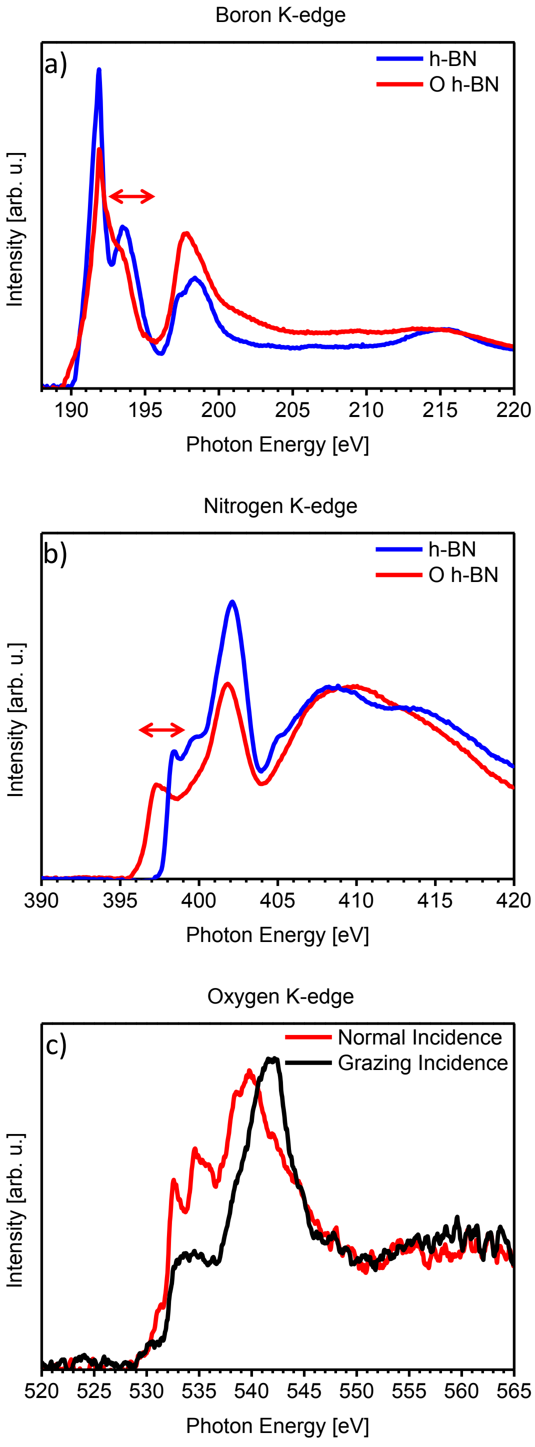

Figure 5.4 (a) NEXAFS spectra measured at the boron K-edge for oxygen adsorption at 290 K (blue) and for pristine h-BN. (b) Spectra recorded at the nitrogen K-edge, for pristine h-BN (black) and oxygen adsorbed h-BN (blue). Photon energy range of the interlayer states is given with a red double arrow. (c) Spectra recoded at the oxygen K-edge at different incidence angles.

In the following, we discuss the changes in the NEXAFS spectra upon reaction of h-BN with molecular oxygen at 290 K. For the boron K-edge (Figure 5.4a), we find a decrease of the peak at 192 eV, while the interlayer states broaden towards lower photon ener-

gies. Moreover, the σ* transitions merge into a single asymmetric broad peak at 197.7 eV. No feature indicative of boron oxide is observed, which would show sharp up as resonances between 192 and 194 eV[205]. At the nitrogen K-edge (Figure 5.4b), after oxygen exposure at 290 K (blue), the main h-BN feature decreases and shifts slightly, to 401.8 eV, and the interlayer states broaden towards lower photon energies, from 398 to 397.5 eV. Similar changes to the NEXAFS spectra as seen in Figure 5.4 after oxygen exposure have been observed upon hydrogenation of h-BN[139], and have been assigned to a stronger interaction of h-BN with a Ni(111) substrate.

At the oxygen K-edge (Figure 5.4c), spectra were measured at normal and grazing incidence, to provide information on the bonding geometry and orientation of the adsorbed oxygen species. At normal incidence (0°, red), we observe π* transitions at 532.6 and 534.6 eV, along a broad absorption feature from 537 to 546 eV, which likely originates from σ* transitions. At grazing incidence (70°, black), we observe a weaker and smeared out π* transitions from 531 to 536 eV, and intense σ* transitions from ~539 to 548 eV. Based on pronounced differences in the NEXAFS spectra at normal and grazing emission, we propose that the adsorbed species is a molecular state.

DFT calculations

To obtain additional insights into the interaction of oxygen with h-BN/Ni(111) and the nature of the adsorbed species, we performed DFT calculations of possible adsorption structure. The studies are performed using a (2 × 2) unit cell of h-BN on Ni(111). The h-BN lattice adopts the stable top-fcc hollow structure with nitrogen atoms at top sites. In this structure, the B-B and N-N distances are 2.49 Å, the B-N bond length is 1.44 Å, with a B-N-B dihedral angle of 119°. The buckling of the h-BN lattice is 0.11 Å, with the boron atoms being closer to the Ni(111) surface than the nitrogen atoms.

As first step, we consider the adsorption of atomic oxygen on h-BN/Ni(111), at sites on-top of boron or nitrogen atoms. We calculated atomic adsorption energies with respect to molecular oxygen in the gas phase as described in the computational details. The optimized structures of one oxygen atom per unit cell are shown in Figure 5.5a and 5.5b, respectively. The obtained adsorption energies of -0.07 eV at the top-B site and +1.78 eV at the top-N site indicate that only very weak or even no bonding with respect to molecular oxygen is observed, respectively. Upon oxygen adsorption at the top-B site, the functionalized boron atom moves 0.58 Å out of plane and the adjacent nitrogen atom 0.08 Å closer to the Ni(111) surface, creating an overall buckling of 0.59 Å. The B-O bond length is 1.36 Å and the N-B-N dihedral angle is 106°. Upon oxygen adsorption at the top-N site, the functionalized nitrogen atom moves 0.20 Å out of plane, and also the adjacent boron atoms move 0.07 Å away from the surface, still being closer than the nitrogen atoms. This yields an overall buckling of 0.27 Å of the h-BN layer. The N-O bond length is 1.49 Å and N-B-N dihedral angle is 118°. In addition to the described behavior, oxygen adsorption also changes B-B, N-N and B-N bond lengths. A Bader charge analysis[203] reveals that oxygen adsorbed at top-B gets 1.3 electrons from the surface, whereas oxygen adsorbed at top-N acquires a charge of 0.5 electrons from the surface.

Next, we addressed the adsorption of intact O_2 on h-BN on Ni(111), with one oxygen molecule per unit cell. This corresponds to a coverage of 0.25 ML. We investigated a variety of different adsorption geometries, and will discuss the most relevant three in the following. The most stable arrangement is the top-B site bridge configuration with an adsorption energy of -0.51 eV/atom (-1.02 eV/adsorbed molecule); see Figure 5.6a and Table 5.1. In this geometry, the two oxygen atoms sit on top of two neighboring boron atoms by forming two B-O bonds of bond length 1.52 Å. The buckling in the h-BN layer is 0.66 Å, and the O-O bond length is 1.44 Å, as compared to 1.23 Å in the gas phase. A Bader charge analysis[206] shows that each oxygen atom acquires 0.76 electrons and becomes negatively charged. For comparison, we also calculated the O-O bond length for O_2^- in gas phase, obtaining 1.31 Å. From these results, we can say that O_2 adsorption at top-B results into a negatively charged O_2 species. The stability of the structure was confirmed by a vibrational analysis at the Γ- point, which yielded all positive frequencies.

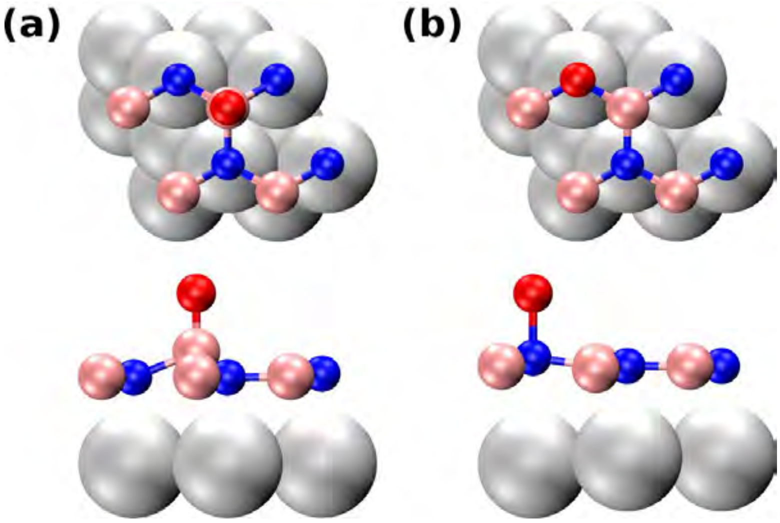

Figure 5.5: Top and side view of isolated oxygen adsorption on (a) top-B and (b) top-N site of h-BN/Ni(111). Nickel, boron, nitrogen and oxygen atoms are shown in silver, pink, blue and red spheres respectively. We have reduced the size of the nickel atoms in the side views for clear view.

O_2 adsorption at top-nitrogen sites leads to a physisorbed O_2 species, 3.10 Å above the surface with an adsorption energy of -0.1 eV/atom. The buckling of the h-BN layer of 0.11 Å is identical to that of pristine h-BN on Ni(111), and the O-O bond length of 1.25 Å is only slightly larger than the gas phase value of 1.23 Å. The third configuration to be discussed is O_2 adsorption in an ortho-functionalization pattern (i.e. one oxygen at a top-boron site and one oxygen at a top-nitrogen site). The corresponding geometry optimization leads to O_2 adsorbed on top of a boron atom with the molecular axis inclined from the surface normal as shown in Figure 5.6c with an adsorption energy of -0.24 eV/atom and accompanied by a buckling of the h-BN layer of 0.53 Å. Furthermore, we performed test calculations for O_2 adsorbed at a bridge site between two neighboring boron atoms of h-BN/Ni(111) in its frozen pre-adsorption geometry, i.e. adsorption according to the structure of Figure 5.6a without relaxation of the h-BN/Ni. Geometry optimization of the O_2 molecule leads to an only merely physisorbed O_2. Hence bucking is important parameter for the adsorption of oxygen on top-B sites of h-BN/Ni and a prerequisite for chemisorption. Upon increasing the oxygen coverage the adsorption energy decreases. For the maximal coverage of 0.50 ML, oxygen adsorption becomes endothermic as shown in Table 5.1.

Structure	E_{ads}/O/eV	O-O /Å	Buckling	Charge on O/e
h-BN			0.11	
O_2 in gas phase		1.21		0
O_2^- in gas phase		1.28		-0.50
O_2^{2-} in gas phase		1.49		-1.00
1O top-B	-0.07	-	0.59	-1.30
1O top-N	1.78	-	0.27	-0.50
O_2 bridge configuration	-0.51	1.44	0.66	-0.76
O_2 physisorption	-0.10	1.25	0.11	-0.05
O_2 on top-B	-0.24	1.34	0.53	-0.43
3O top-B → O_2 top-B and 1O top-B	-0.02	1.39	0.60	-0.77
3O top-N	2.08	-	0.64	-0.24
$2O_2$ top-B	0.05	1.40	0.60	-0.60
4O top-N	2.09	-	0.60	-0.32

Table 5.1: Average adsorption energies per oxygen atom with respect to O2 in the gas phase, O-O bond lengths and buckling in h-BN, and charge on oxygen atom upon adsorption on h-BN/Ni(111). For the reference, we have also added O-O bond length of O2 in gas phase.

Our DFT calculation show that the top-B site bridge configuration is the most stable configuration of O_2 on h-BN on Ni(111). This configuration of adsorbed oxygen is between a superoxide (O_2^-) and a peroxide (O_2^{2-}) bound to two boron atoms, with its molecular axis is parallel to the surface. This is in agreement with DFT calculations in literature[172, 199,207].

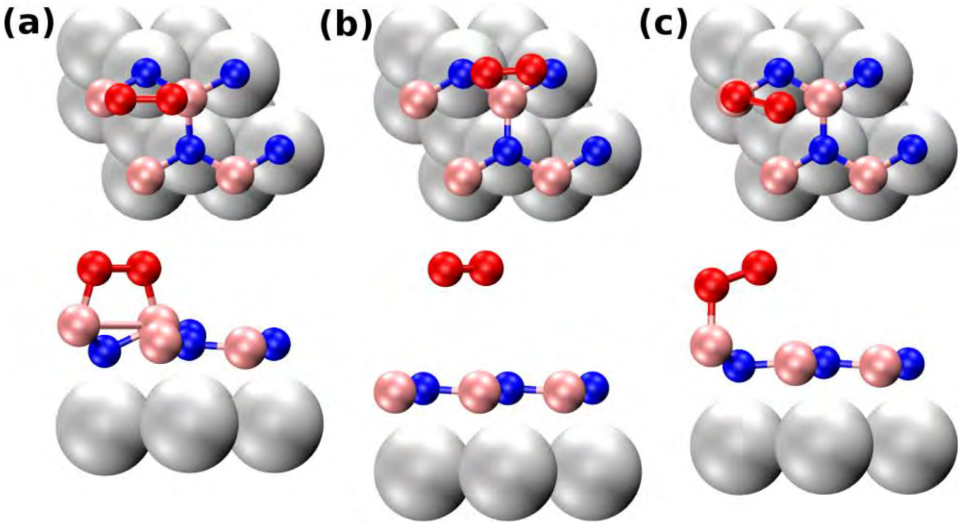

Figure 5.6: Top and side view of optimized structures of O_2 adsorption on (a) top-B site bridge configuration, (b) physisorption and (c) top-B site of h-BN/Ni(111).

As a next step, we addressed the experimental observation of an activated adsorption. To that end, we searched for the transition states between the molecule in the gas phase and its adsorbed final state in the top-B site bridge. In the DFT calculations, we locate the transition states for O_2 adsorption through the climbing image nudged elastic band (CI-NEB) method implemented in VASP. Five images connecting reactants and products have been used. The TS search procedure involved a first Cl-NEB calculations using a force criteria of 0.02 eV/Å as convergence criteria. Then the highest image was relaxed by a quasi-Newtonian method.

In Figure 5.7, the calculated energy landscape along the reaction coordinate for O_2 adsorption is shown. Local TSs for a number of different possible reaction paths were studied and compared. For reference, we considered O_2 in gas phase. Altogether, we find energy barriers in two steps: The first energy barrier is found between O_2 physisorption and the top-B site geometry; the barrier is ~0.4 eV, with the TS ~0.2 eV above the (zero) energy of the free molecule. The second barrier is located between the top-B site geometry and the most stable top-B site bridge configuration; its height is ~0.6 eV with the TS again ~0.2 eV above the (zero) energy of the free molecule.

The calculation clearly shows that in order to reach the stable top-B site bridge configuration, the molecule has to overcome the identified activations barriers, which amount to 0.2 eV/atom or 0.4 eV/molecule above the (zero) energy of the free molecule. This result is taken as explanation for the experimentally observation that the sticking coefficient for thermal oxygen with an energy of 2kT = 0.05 eV is close to zero. Only when using oxygen with a higher kinetic energy, the activation barrier can be overcome. Very likely, the molecules will not fully thermalize into the local minima along the reaction coordinate.

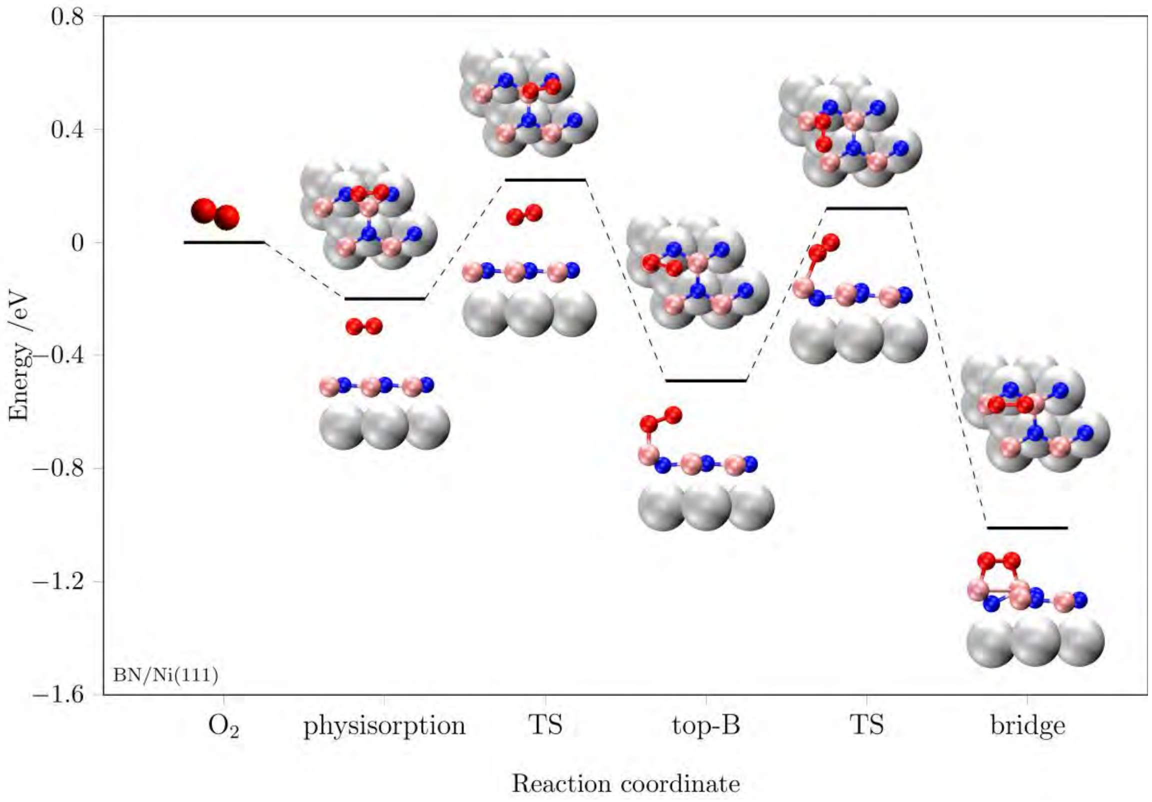

Figure 5.7: Oxygen adsorption energies of possible barrier and (local) minimum structures during adsorption of O_2 on h-BN/Ni(111) calculated in a (2×2) unit cell.

Changes to the electronic structure of h-BN/Ni(111) upon oxygen adsorption

Next, we discuss the electronic structure of h-BN/Ni upon adsorption of molecular oxygen. We have already discussed the electronic band structure of pristine h-BN/Ni(111) in our previous work[139]. We measured valence band spectra of h-BN at the Γ-point (that is, at normal emission) with a photon energy of 85 eV; see Figure 5.8. According to literature, h-BN shows three bands at the Γ-point, the σ_1 band at 5.0 eV, the π band at 10.0 eV and the σ_2 band 22.7 eV[62, 97,139]. The π and the σ_2 band are well resolved, but at the photon energy of 85 eV, the σ_1 band is not discernible from the background. Additional contributions, arising from the h-BN-substrate interaction may be present close to the Fermi edge (0 - 3 eV)[62].

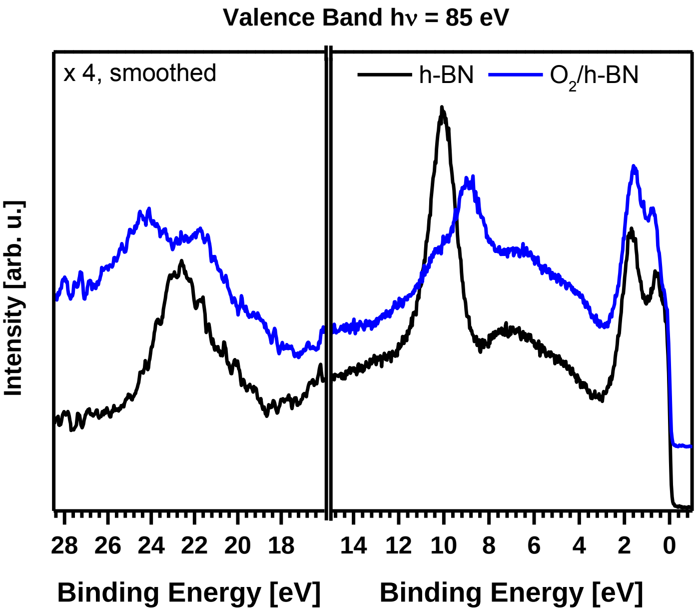

Figure 5.8: *Valence band spectra of h-BN (black) and after oxygen adsorption on h-BN at 290 K (blue); measured with hν = 85 eV, at normal emission.*

Upon oxygen exposure (Figure 5.8, blue), the maximum of the π band shifts to 8.8 eV; however, at its original position at 10.0 eV still intensity remains, indicating that only part of the h-BN has reacted, as was also concluded in the analysis of the B 1s core level (see above). The σ_2-band shifts to ~21.7 eV. Moreover, an additional contribution is observed at 24.3 eV, which we assign to the O 2s core level. Moreover, we find that the shape of the Ni 3d states at the Fermi edge changes. This may be due to the stronger interaction of h-BN with the Ni(111) substrate after oxygen adsorption.

Figure 5.9 shows the calculated electronic band structure of h-BN/Ni with 0.25 ML of O_2 adsorbed in the most stable adsorption geometry, i.e. the bridge geometry between two boron atoms. The Fermi level is set to zero. Upon oxygen adsorption, we find the oxygen 2s states at 23 eV that shows no dispersion. The h-BN related bands all show a shift to lower binding energies ~ by 1 eV towards E_F, according to the experimental findings.

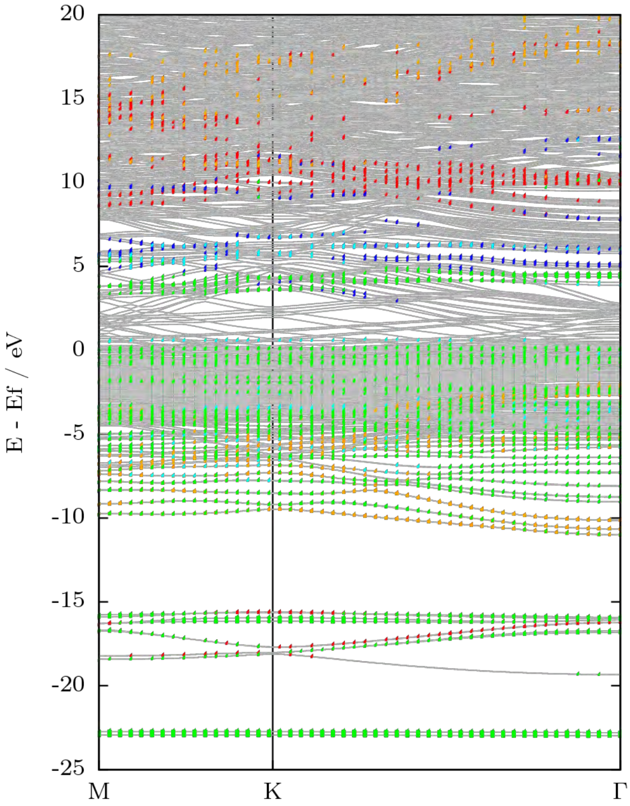

Figure 5.9: *Band structure of h-BN/Ni(111) (from a 2x2 unit cell) with 0,25 ML of O_2 adsorbed at top-B bridge position. Boron and nitrogen σ (red and orange) and π (blue and cyan) are indicated by circles, respectively. Oxygen contribution to σ and π bands are shown in dark green and magenta color respectively.*

Thermal evolution

Finally, we studied the stability of the oxygen functional groups with temperature programmed XPS. The quantitative analysis of this data is shown in Figure 5.10. At the start of the experiment, we observe the two oxygen species, bonded oxygen and a small contribution from boron oxide, which was also seen during the adsorption. During heating, we observe a slow decrease of the adsorbed oxygen species from 400 to 500 K, due to desorption. Beginning at 500 K, the desorption rate accelerates, with the steepest decrease at 580 K, indicating the highest desorption rate. In the same temperature region, we observe the reaction of a fraction of the bonded oxygen with h-BN, yielding various boron oxides, the sum of which is shown in Figure 5.10. A more detailed discussion of the reaction of the oxides will be given in Chapter 6. Heating to 900 K leads to a band structure and also to core level spectra that are similar to those observed before oxygen adsorption (but with loss of nitrogen) and the additional features in the B 1s and O 1s core levels, indicative of the formation of boron oxides.

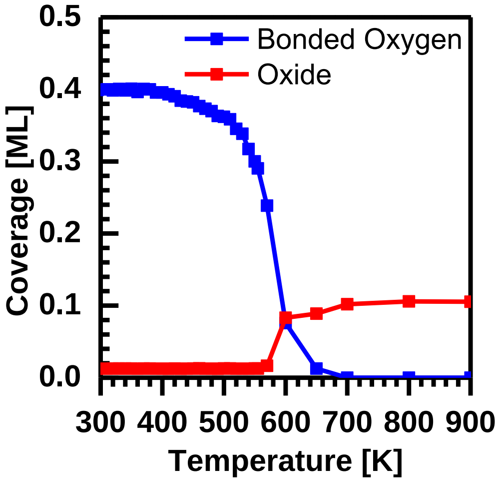

Figure 5.10 Quantitative analysis of the temperature programmed experiment carried out in the O 1s core level.

5.4 Discussion and Conclusion

We accumulated combined experimental information on adsorbed molecular oxygen species on h-BN. This species was until now not investigated experimentally, since the adsorption is an activated process and the relevant activation barrier can only be overcome using a supersonic molecular beam of molecular oxygen, in our case with a kinetic energy of 0.7 eV. From our combined XPS, NEXAFS and UPS results, we conclude that the adsorbed species is a molecular rather than in atomic state. The clearest evidence stems from the pronounced differences in the NEXAFS spectra at normal and grazing emission. While the identification of the nature of the adsorbed molecular species is difficult form the experimental data alone, our DFT calculations provide very clear evidence that the adsorbed oxygen is between a superoxide (O_2^-) and a peroxide (O_2^{2-}) bound to two boron atoms, denoted as top-B site bridge configuration. In this configuration, the molecular axis is parallel to the surface. This is in agreement with DFT calculations in literature,[172, 199,207] which find that this is the most stable bonding configuration for oxygen adsorbed on h-BN. The bonding leads to a buckling of h-BN, with one of the nitrogen atoms becoming closer to the Ni(111) surface and the two boron atoms that bind to oxygen move away from the surface.

In the DFT calculations, we also determined the transition states for O_2 adsorption through the climbing image nudged elastic band method. The calculation clearly shows that in order to reach the stable top-B site bridge configuration, the molecule has to overcome the identified activations barriers, which amount to 0.2 eV/atom or 0.4 eV/molecule above the (zero) energy of the free molecule. This result is taken as explanation for the experimentally observation that the sticking coefficient for thermal oxygen with an energy of $2kT = 0.05$ eV is close to zero. Only when using oxygen with a higher kinetic energy, the activation barrier can be overcome. Very likely, the molecules will not fully thermalize into the local minima along the reaction coordinate.

By analysis of the nitrogen and boron XPS and NEXAFS data, we find that upon oxygen binding, the h-BN Ni(111) interaction becomes stronger. Particularly the B K-edge shows a decrease of the a_0 feature along with a broadening of the interlayer states, which indicates a stronger bond. In the σ^* transitions of the B K-edge, we find a change from a double peak structure to a single broad, asymmetric peak, similar to what was found for h-BN functionalized with hydrogen[139], also supporting a stronger h-BN-surface interaction upon oxygen bonding. This similarity is taken as confirmation of the formation of an oxygen-boron bond (similar to the hydrogen – boron bond upon hydrogenation), as is also predicted by DFT. From the NEXAFS data, we rule out the possibility of oxygen intercalating the h-BN layer.

The bonding mode proposed from DFT is in agreement with the core level shifts observed in the B 1s and N 1s region: In the N 1s spectra, the formation of a doublet after oxygen adsorption is attributed to chemically and geometrically inequivalent nitrogen atoms within the O_2-h-BN lattice. In a simplified picture, with a periodical 2x2 unit cell, we find rows of nitrogen atoms with one neighboring boron atoms that bind to oxygen and nitrogen atoms with two neighboring boron atoms that bind to oxygen (see Figure 6a and also Supporting Information) This leads to the two peaks at 398.1 and 397.5 eV. In the B 1s region, the signal broadens and shifts to lower binding energies after oxygen functionalization due to the formation of two chemically different species. We expect one signal from boron atoms bonding to oxygen, and one from boron atoms not in contact with oxygen. However, these two contributions are not resolved.

Finally, temperature programmed experiments reveal that the adsorbed oxygen is stable to temperatures above 500 K, showing that the oxygen forms strong covalent bond to the h-BN surface. The bonded oxygen mostly desorbs at ~580 K, with partial reaction to boron oxides. Notably, the same experiment was also performed for the graphene/Ni(111) system. However, graphene seems to interact more strongly with the Ni(111) substrate, preventing bonding. Even elevated temperatures do not lead to an intercalation or oxygen bonding (see supporting information). Only increased temperatures and orders of magnitude higher oxygen pressure result in intercalation[81,208].

6 Oxygen adsorption on h-BN/Ni(111) at 440 and 600 K

Interestingly, the reaction pathway of molecular oxygen on the surface does not only depend on the kinetic energy of the impinging molecules, but also on the substrate temperature. For the oxygen adsorption at 440 K, in the beginning of the experiment bonded oxygen is observed. Subsequently, this oxygen species vanishes and intercalated oxygen is found, with minor amounts of boron oxide. The interpretation of oxygen intercalated h-BN is supported by NEXAFS measurements, revealing that h-BN has a more free-standing character after the oxygen adsorption. Temperature-programmed desorption experiments show that the intercalated oxygen has completely desorbed at 900 K with the desorption maximum at ~ 700 K. Parallel to the desorption of the intercalated oxygen h-BN becomes significantly oxidized. Upon adsorption at 600 K, the main reaction pathway is the oxidation of h-BN, with the formation of various boron oxides and the loss of nitrogen. Heating the sample, results in partial desorption of oxygen, the formation of B_2O_3 as the main oxide contribution and the partial restoration of h-BN, likely as intact islands.

6.1 Introduction

Hexagonal boron-nitride (h-BN), a 2D crystal, where boron and nitrogen atoms are alternatingly arranged in a hexagonal pattern has gained interest in the scientific community over the last years[52, 141,169]. Its interesting properties are e.g., its chemical inertness[147], its band structure, and high strain endurance[140,188]. h-BNs electronic properties are very intriguing, in that it is an insulator with a bandgap of 5.4 eV[77,142]. In contrast, graphene, its a structural and isoelectronic analogue, is a semi metal with a Dirac cone. Furthermore, it was shown that it is possible to grow graphene on top of h-BN[97]. Together this makes the two materials very interesting for semiconductor industry, as an atomically thin semi-conducting layer (graphene) and an atomically thin dielectric (h-BN). As devices made out of 2D materials are still in their infancy, it is necessary to better understand the interaction of these 2D materials with gases from atmosphere in particular oxygen and water are always present in minor concentrations during device operation, even if it is sealed, which may lead to drastic changes in charge carrier mobility, or on/off ratios, as the band structure changes.

Previously, 2D materials were studied as a barrier to prevent oxidation of metal supports with ambiguous results. Graphene adsorbed on copper was investigated by two different groups, finding that copper is oxidized faster in air, both at room temperature and at elevated temperatures, when graphene is adsorbed[209,210]. However, theoretical studies fail to observe this effect entirely and find that the ideal, i.e. defect free graphene layer should be an excellent barrier to oxidation[211]. For h-BN, a first study shows indeed that it might be this ideal, one atom thick oxidation barrier, at least for copper[147]. With pressures achievable in an UHV-setup, the oxidation of h-BN on Ir(111) was already studied in detail, showing that elevated temperature lead to the oxidation of h-BN with the formation of various boron oxides[205]. Until now, a study on the interaction of oxygen with h-BN on Ni(111) is missing in literature. This might be due to the strong interaction of h-BN with the Ni(111) substrate, which is larger than for Cu(111) and Pt(111)[178,212]. Thus, finding suitable reaction conditions may be challenging, as explained below.

In the following, we will discuss the interaction of high energetic oxygen molecules with h-BN on Ni(111) at different substrate temperatures, as determined by XPS, NEXAFS, UPS and DFT. Depending on the substrate temperature, we find different interactions of oxygen with h-BN: At 440 K, the majority species is intercalated oxygen (h-BN/O/Ni(111)), and at 600 K, we find the oxidation of h-BN. A comparison to graphene on Ni(111) will be given, where no intercalation with oxygen was found under similar experimental conditions.

6.2 Results

High-resolution in-situ photoemission spectra of oxygen adsorption

In the following, we discuss the XP spectra collected in the O 1s regions during exposure of h-BN at 440 and 600 K to molecular oxygen using the supersonic beam with a kinetic energy of E_{kin} ~ 0.7 eV. Notably, this high kinetic energy is required, because oxygen with a thermal energy corresponding to 300 K does not stick on the surface. During this adsorption experiment, the sample is normal to the molecular beam (NMB). After the end of the uptake, N 1s and B 1s spectra were recorded, with the sample rotated such that the surface normal points towards the electron analyzer.

The spectra of the O 1s region are shown in Figure 6.1a, 6.1c, while selected fits of the spectra are shown in 6.1b and 6.1d. At 440 K, in the first 45 seconds we observe nearly exclusively the formation of peak at 531.5 eV (Figure 6.1e blue curve). From previous work, shown in Chapter 5, we conclude that this is the XP-fingerprint of oxygen binding to h-BN in a side-on configuration, from the vacuum side. At higher exposures, the formation of two further peaks at 533.1 and 531.4 eV (red and green in Figure 6.1d, respectively) is observed, albeit at a lower rate (see Figure 6.1e). The total oxygen coverage at the end of the experiment at 780 s corresponds to ~ 1 ML, with 0.06 ML in the peak at 531.5 eV (blue, O-bonded), 0.6 ML in the peak at 531.4 eV (green, intercalated O) and 0.3 ML in the peak at 533.1 eV (red, oxide), as is evident from Figure 6.1f. Notably, the two species at 531.5 and 531.4 eV have a very similar binding energy, but a strongly different FWHM, which make the fit equivocal. For our fits, we used constraints such that both contributions cannot change binding energy or FWHM. Thus due to a broadening of the peak towards lower binding energy upon adsorption the sharper species at 531.5 eV is reduced in height for the more broader species at 531.4 eV, to achieve a better fit.

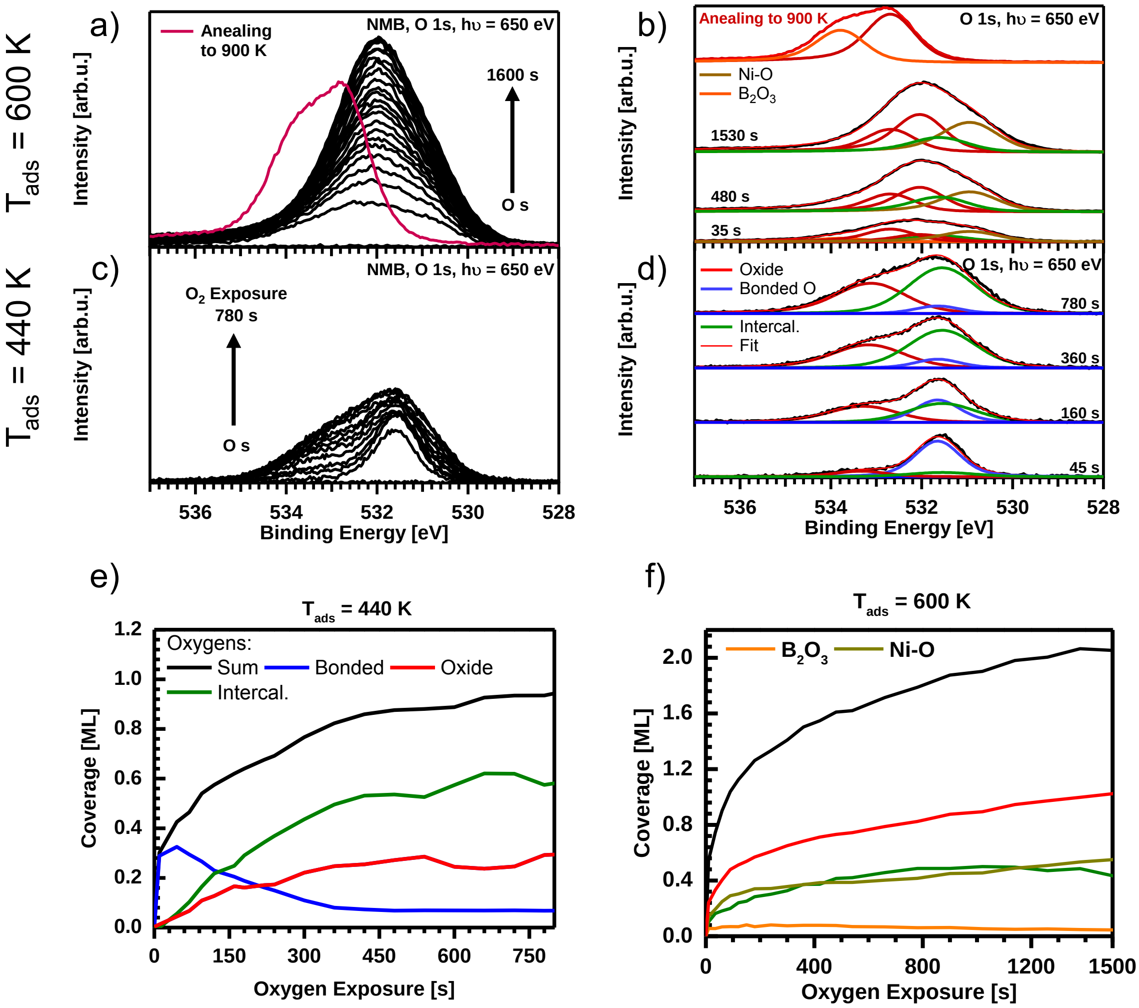

Figure 6.1 spectra obtained during exposure of h-BN to high energetic oxygen, at (a) 600, (c) 440 K. (b), (d) fits of selected spectra, depicted in (a), (d), respectively. (e), (f) quantitative analysis of the experiments performed at 440 and 600 K, respectively. In the analysis, we account for damping of the oxygen that is intercalated. Damping, as determined from a measurement of the Ni 2p region with a similar electron kinetic energy, and leads to a reduction of the signal by 33% when h-BN has formed a closed layer on top of Ni(111).

The spectra collected during exposure of molecular oxygen to h-BN at 600 K are shown in Figure 6.1a, along with selected fits in Figure 6.1b, and the quantitative analysis given in Figure 6.1f. In the first 100 s, we observe a rapid increase of a single, broad contribution. At higher exposure, the shape of the broad peaks shows some change; the intensity increase slows down, but shows no sign of saturation, even at very high exposures. After the highest exposure at 1500 s, the coverage is 2.1 ML. Please note that the fit in the O 1s region is ambiguous and needs to be correlated to the findings in the B 1s and N 1s regions, and to our NEXAFS data (see below). One of the fitted peaks is found at 531.4 eV that is, at the same energy as one of the species found at 440 K. In addition, we observe three additional species at 532.0, 532.7 and 533.8 eV (Figure 6.1b). The quantitative analysis reveals an increase of all peaks during the exposure, expect for that at 531.4 eV (green), which saturats at ~800 s. When heating the sample after adsorption at 600 K to 900 K (Figure 6.1a, red), we observe an increase of the peak at 532.7 and the development of a new peak at 533.8 eV; simultaneously all other peaks decrease. The two peaks at 900 K are assigned to B_2O_3 (orange) and various other oxides (red) see below.

Photoemission spectra of the B 1s and N 1s core level after oxygen adsorption

After the in-situ adsorption experiment, the sample was rotated such that the surface normal pointed to the energy analyzer (NEA) and B 1s and N 1s spectra were recorded; see Figure 6.2a and 6.2b. Prior to oxygen exposure, we observe a single B 1s peak at 190.5 eV and a single N 1s peak at 398.8 eV, characteristic of h-BN[97,139]. Upon oxygen adsorption at 440 K, the main peak shifts to 190.2 eV (Figure 6.2a, red) with a pronounced high binding energy shoulder at 191.5 eV. At 600 K (Figure 6.2a, dark red), we again observe the peak at 190.2 eV, but with lower intensity than at 440 K; the high energy shoulder, now at 191.0 eV and broadened towards higher binding energy, has become the dominant feature. When heating this sample to 900 K (Figure 6.2a, green) we find the restauration of the peak at 190.5 eV, which is attributed to pristine h-BN. In addition, peaks at 191.1 and 193.6 eV are observed, with some non-resolved features in-between.

In the N 1s region, upon oxygen adsorption at 440 K, we observe, two contributions, at 397.6 and 398.3 eV, with an asymmetry of the former towards lower binding energy. The overall signal has decreased by ~30%, indicating loss of nitrogen. For exposure at 600 K, we find the same peaks as at 440 K, but an overall decrease the total amount of nitrogen by 50%. When heating this sample to 900 K, the single contribution of h-BN on Ni(111) at 398.8 eV is restored, however, with decreased intensity due to the loss of nitrogen.

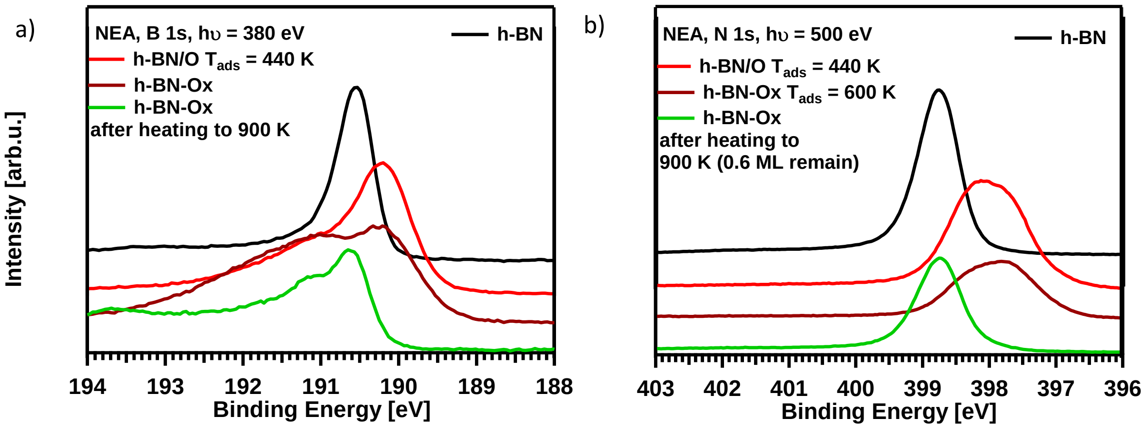

Figure 6.2 Spectra obtained in the B 1s core level (a) and N 1s core level (b). Pristine h-BN, the starting point for each experiment is depicted in black. Spectra recorded after each adsorption experiment are subsequently offset.

NEXAFS

To obtain further information, we applied NEXAFS at the nitrogen and boron K edges; see Figure 6.3. We here only want to discuss the changes in the absorption spectra, when h-BN is exposed to highly energetic oxygen at different substrate temperatures. The spectra of pristine h-BN on Ni(111) agree with literature[62, 97,98, 139,149]. They shows so called interlayer states, due to the interaction (hybridization) of h-BN with the substrate[62, 98,149]. These states have a π-character and lie parallel to the h-BN sheet. In Figure 6.3, we have marked the corresponding photon energy range with a red double-arrow: At the boron K-edge, these states manifest themselves as a broad feature from 193 to 195 eV. We observe that the dominating a_0 peak of h-BN lies at 192 eV, in line with literature. This feature is an indicator for quasi-free-standing h-BN: a large a_0 peak and weak or vanishing interlayer states indicate a quasi-free standing character. This is observed, when comparing the spectra recorded after oxygen intercalation (red) and pristine h-BN (black). Thus a quasi-free standing character is observed. Upon oxidation of h-BN, several characteristic features have been reported in literature[205], and their energies are indicated by vertical lines in Figure 6.3a denoted in green $a_{1\text{-}3}$. They correspond to boron atoms with 1, 2 or 3 neighboring oxygen atoms, respectively, for each small index. These features partly overlap with the energy range of the interlayer states, but are easily identified due to their small linewidth. From 196 to 201 eV, the σ* transitions of h-BN are found[205]. From our studies addressing bonded hydrogen, we know that single H atoms do not have an effect on these states[139]. At the nitrogen K-edge, the interlayer states are found between 397 and 399 eV[62, 98,149] (marked with a red double-arrow), as a sharp shoulder at ~398 eV. Additionally, pristine h-BN shows one main feature at 402 eV, which is marked with (II). Upon oxygen adsorption, a new feature named (I) develops at 401 eV, which was previously also observed for h-BN with a quasi-free-standing character, achieved via hydrogen intercalation.

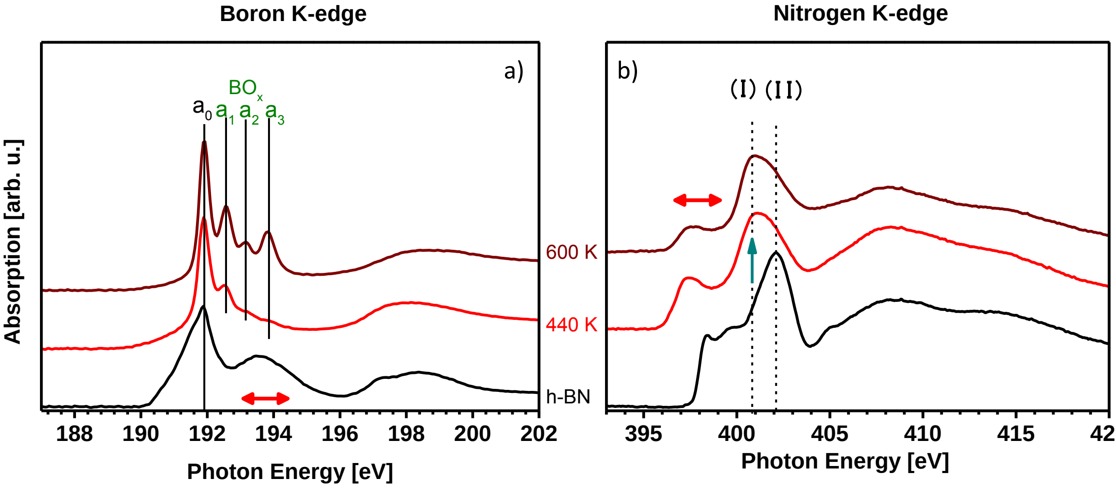

Figure 6.3 (a) NEXAFS spectra measured at the boron K-edge for oxygen adsorption at various temperatures. Feature a0 is attributed to h-BN, while $a_{1\text{-}3}$ are attributed to oxidized boron. The photon energy range of the interlayer states is given with a red double arrow. (b) Spectra recorded at the nitrogen K-edge for different oxygen adsorption temperatures. Interlayer states region is given with a red double arrow, the main features are marked with dashed lines.

In the following, we discuss the changes in the NEXAFS spectra upon oxygen adsorption, first at the boron and subsequently at the nitrogen K-edge. At the boron K-edge, at 440 K (red), the main peak a_0 sharpens and shows increased intensity, while the interlayer states (red double arrow) decrease, which indicates a quasi-free-standing character[97, 139,177]. In addition, feature a_1, which is attributed to boron binding to a single oxygen atom, is now observed. The σ* transitions smear out, and shift to higher photon energies. At 600 K (brown), the intensity of a_0 is similar to that at 440 K. However, feature a_1 increases and additionally also features a_2 and a_3 appear as well resolved peaks. The interlayer states are no longer visible, and the σ^* transitions shift to slightly higher binding energy.

At the nitrogen K-edge in Figure 6.3b, we find that the interlayer states shift to lower photon energies, from 398 to 397 eV. To the best of our knowledge, such a shift has not been observed before for intercalated h-BN. This shift is generally accepted to originate from defects[213]. However, the difference in bonding of h-BN to the surface upon oxygen exposure may also populate this state. The new state (I) at 401 eV (a green arrow in Figure 6.3) was also previously observed for hydrogen intercalation, i.e. h-BN that has a more quasi-free standing character. Upon adsorption of oxygen at 600 K, no major differences to the spectrum recorded at 440 K are visible, except for a lower overall intensity, hinting towards a loss of nitrogen, in line with our XPS results.

UPS spectra of oxygen adsorbed h-BN

To obtain insight to the changes in the electronic structure of h-BN upon exposure to molecular oxygen, we measured valence band spectra at the Γ-point (that is, at normal emission) with a photon energy of 85 eV and an angular acceptance of ± 1°; see Figure 6.4. h-BN shows three bands, the σ_1 band at 5.0 eV, the π band at 10.0 eV, the σ_2 band 22.7 eV at the Γ-point, in line with literature[62, 97,139]. At the photon energy of 85 eV, the σ_1 band is not discernible from the background. Additional contributions, arising from the h-BN-substrate interaction may be present, close to the Fermi edge (0 - 3 eV)[62].

Upon oxygen exposure at 440 K, (red), the π band shifts to 8.6 eV, the σ_2 shifts to 21.2 eV. Moreover, the doublet originating from the Ni 3d states between 0 - 2 eV is no longer resolvable, indicating some change in the hybridization between the h-BN and Ni 3d orbitals. A small contribution from oxygen at 26 eV is observed. At 600 K (brown), the π and σ states are very similar to the situation at 440 K; however, states attributed to significant amounts of adsorbed oxygen species are now found at ~7 and 26 eV. After heating this sample to 900 K (green), we find the π and σ_2 states at a binding energies characteristic of pristine h-BN. In addition, the two states attributed to oxygen are still observed at ~7 and 26 eV. This is in line with XPS, where also significant amounts of oxygen are still observed on the sample after heating.

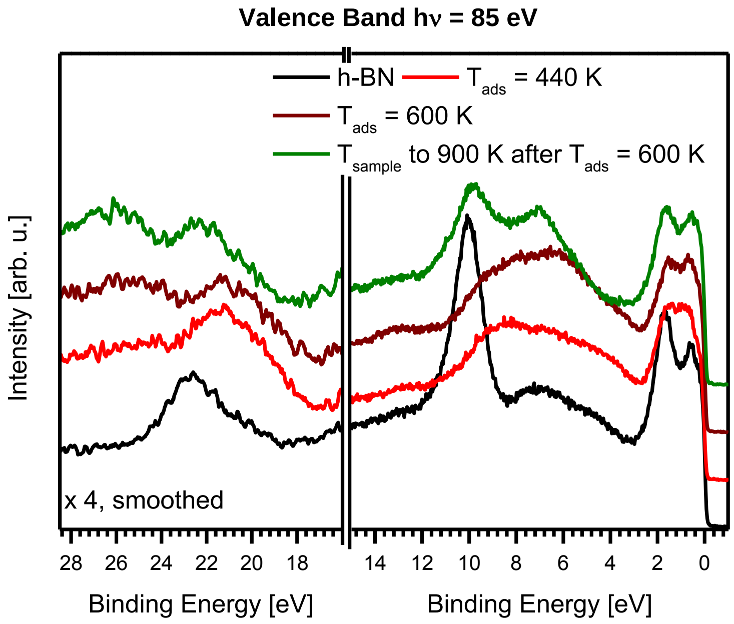

Figure 6.4 Valence band spectra of h-BN and oxygen adsorbed h-BN.

Thermal stability of the adsorbed oxygen

To obtain insight into the thermal stability of the intercalated oxygen and various boron oxides, a heating experiment was conducted. For the sample exposed to oxygen at 440 K, up to 550 K every 10 K a spectrum in the O 1s core level was recorded. Subsequently every 100 K a spectrum was recorded. The quantitative analysis of the obtained data is shown in Figure 6.5a. The thermal stability of the bonded oxygen is discussed in Chapter 5 and the reaction of oxidized h-BN at higher temperature is given in detail for the layer specifically oxidized at a substrate temperature of 600 K in Figure 6.5b.

The intercalated oxygen starts to desorb already at 460 K. Up to 600 K, a slow continuous desorption is observed. Above 600 K, the desorption rate increases. At 900 K, no intercalated oxygen is observed on the sample. However, a large fraction of intercalated oxygen was transformed into various oxide species, described in detail for the sample oxidized at 600 K. For the sample exposed to oxygen at 600 K, the following is observed, when heating to 900 K, as shown in Figure 6.5b: Intercalated oxygen vanishes, in line with the heating experiment described for the experiment shown in Figure 6.5a. Also the contribution for nickel oxide vanished at 900 K. The contribution for the oxides (Figure 6.5b, red) diminishes by ~ 10%. However, the contribution for B_2O_3 increases to 0.5 ML. This increase is expected as B_2O_3 is the most stable oxide of boron.

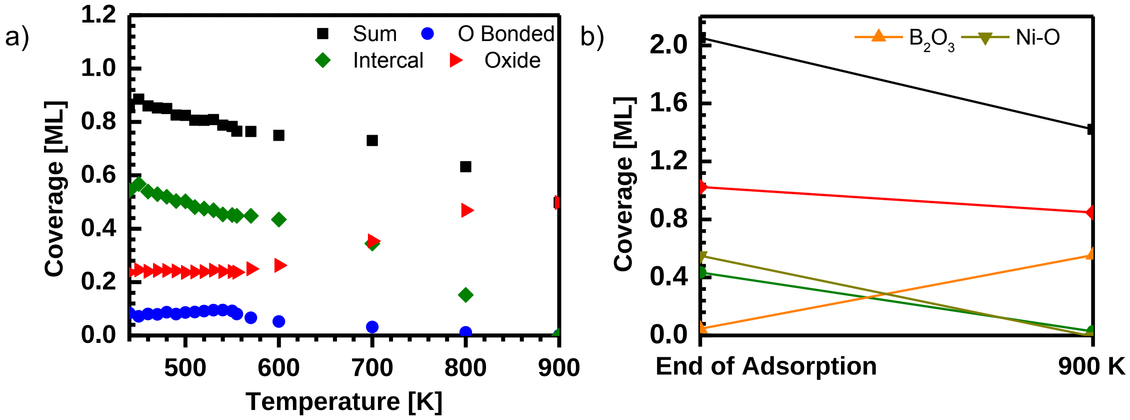

Figure 6.5 (a) Quantitative analysis of the temperature-programmed experiment, performed after adsorbing oxygen at 440 K in the O 1s core level. (b) quantitative analysis of the heating experiment of h-BN exposed to oxygen at 600 K. First data point is the last spectrum of the adsorption, last data point is the analysis of the O 1s core level data obtained after heating to 900 K.

6.3 Discussion

The adsorption at a substrate temperature of 440 K leads to the formation of three different oxygen species. One of them is bonded oxygen at 531.5 eV, as already discussed for the adsorption at 290 K in Chapter 5. Two further contributions at 533.1 and 531.4 eV (red and green in Figure 6.1d)) are observed. To further elude the origin of the other two species, boron K-edge NEXAFS data are discussed (Figure 6.3a): two major changes occur, when comparing the bonding of oxygen and the adsorption at 440 K. One is the strong increase of feature a_0 accompanied by a decrease of the interlayer states (193-195 eV)[97,139] indicating a quasi-free-standing character of h-BN. Moreover, the formation of the features a_1 is observed, showing that now oxygen is incorporated into the h-BN layer[205], i.e. boron oxide formation. The nitrogen K-edge (Figure 6.3b) further corroborates the quasi-free-standing character, with the increase of (I), as this was observed, in hydrogen intercalated, quasi-free-standing h-BN[139]. From NEXAFS, we conclude that the h-BN sheet shows a quasi-free-standing character due to oxygen intercalation and is (partially) oxidized. From these conclusions, we assign the species found in the O 1s as: bonded oxygen (531.5 eV), intercalated oxygen (531.4 eV, with a larger full width at half maximum, as discussed above) leading to a quasi-free-standing character and boron oxide (533.1 eV). We assign the feature at 531.4 eV to intercalated oxygen, because its binding energy is closer to that of chemisorbed oxygen on bare Ni(111) at 529.5 eV[214]. The species at 533.1 eV is assigned as boron oxide, due to the high electron deficiency of boron, resulting in a higher binding energy. Our interpretation of the data for the B 1s and N 1s core levels is similar to what is discussed above. The overall shift of all contributions towards lower binding energy is assigned to doping and the quasi-free-standing character of the h-BN sheet[97] and the electron withdrawing character of oxygen. The second effect on the binding energy that is the splitting of the peaks is due to geometric reasons: h-BN is intercalated by 0.6 ML of oxygen (likely more, as it is concentrated in the intercalated patches, and bonded oxygen and oxidized parts of h-BN are also present, and at these parts oxygen intercalation is not expected). Thereby, about half of the boron and nitrogen atoms are in closer contact to intercalated oxygen leading to two contributions in each core level. The B 1s core level is, again, less sensitive to its surrounding, resulting in a peak with increased FWHM as compared to pristine h-BN, at 190.2 eV. The increased FWHM indicates different chemical species contributing to the peak. However, we cannot assign a species in the B 1s and N 1s unambiguously to a certain geometry (i.e. close or further to intercalated oxygen).

We interpret species from 191 to 192 eV in the B 1s core level as various boron oxides, inside the h-BN lattice (Figure 6.2a), not reported in literature before, likely due to their complex chemical surrounding. Together with the observed single oxygen neighbor of boron observed in NEXAFS (feature a_1), and the quantitative analysis, which shows that 0.3 ML oxygen and 0.3 ML of B^{x+} (i.e. boron in various oxidation states), we can conclude that the overall stoichiometry of boron oxide is BO. The above described asymmetry of the lower binding energy peak in the N 1s core level is attributed to nickel nitrate at 397 eV[109,110,122]. The observed shift in the valence band is well in line with intercalation resulting in a quasi-free-standing character[97]. For the nitrogen K-edge, we observe an increase of the interlayer states, indicating that the oxidation of h-BN introduces defects, and that the oxygen bonding deforms h-BN. The increase of state (I) at 401 eV further corroborates the quasi-free-standing character upon oxygen exposure at 440 K. It is interesting to observe that the quantitative analysis reveals that bonding of oxygen is the first bonding motive to occur. However, as the amount of bonded oxygen decreases subsequently, we reason that intercalated h-BN can no longer bind oxygen, as the necessary h-BN Ni(111) interaction is no longer possible.

For adsorption at 600 K, we begin the interpretation with the boron K-edge. We observe, similar to the 440 K adsorption that the feature a_0 is large, and the interlayer states are small, indicating a quasi-free-standing character (Figure 6.3a). Moreover, features a_{1-3} have increased further, indicating that the h-BN layer is more oxidized as compared to the adsorption at 440 K. In the nitrogen K-edge spectra only a decrease of the overall signal intensity is found. This would indicate that patches of intact h-BN are oxygen intercalated, but the sheet shows many defects, due to nitrogen loss. The shift of the σ* -transitions in the boron K-edge towards higher photon energies (see Figure 6.3a) further corroborates the formation of boron-oxygen bonds[205]. The findings of the nitrogen K-edge spectra are well reproduced in the N 1s core level: The same species are found, compared to the adsorption at 440 K, including the nickel nitrate (397 eV binding energy[109,110,122]). The species at 397.6 eV is now larger compared to the one at 398.3 eV. In the B 1s core level, we still observe the broad feature at 190.2 eV, attributed to intercalation (see Figure 6.2a). Thus, the intact patches of h-BN show a similar reactivity towards oxygen, as compared to the adsorption at 440 K, in that they are intercalated. However, the oxidation and nitrogen loss of the sheet are more rapid and more advanced. In the B 1s, we find several species, which we attribute to oxygen binding to boron, i.e. BO_x formation in a 2D fashion, from ~191 to 194 eV.

However, it is not possible, from our data to elude the exact stoichiometry on the surface: NEXAFS gives direct information on the number of oxygen neighbors of boron, i.e. one to three for a_1 to a_3. However, XPS is more sensitive to the chemical state of boron, i.e. also the bond to nitrogen needs to be considered. Thus we refrain from interpreting the exact stoichiometry without further extensive calculations. The same issues arise from the O 1s core level, which shows peaks above 532 eV that we assign to oxides, while further peaks for bonded oxygen and oxygen adsorbed on Ni(111) coexist. A clear identification is not possible due to these coexisting adsorbates and the assignment needs to be considered as tentative. In the valence band, we observe the same shifts for intercalated h-BN. Additionally, the intensity of the oxygen peaks found at ~7 and 26 eV, increased due to the higher oxygen coverage.

To further characterize the systems, their thermal stability is investigated by temperature programmed XPS. For the sample, where oxygen is adsorbed at 440 K, we find that the bonded oxygen desorbs and reacts in a similar temperature region, as described in Chapter 5. This we interpret as a further indication of the formation of domains (intercalated parts and oxygen bonded parts), because the desorption temperature of bonded oxygen is not affected by the presence of other species. For the intercalated oxygen, we find that at 700 K 50% of the intercalated oxygen has desorbed. Moreover, we observe that further oxygen reacts to boron oxide. Roughly 40% of the intercalated and bonded oxygen react to boron oxide.

When heating the sample, which was exposed to oxygen at 600 K, to 900 K, we observe in the O 1s core level only two oxygen species remain. The one at 533.8 eV, is attributed to B_2O_3, in line with literature, and goes along with the peak at 193.6 eV in the B 1s core level[205]. The second species is, attributed to different boron oxides. From the data gathered in the B 1s core level after heating to 900 K, we find that 0.4 ML of boron are oxidized and 1 ML of oxygen are on the sample (and B_2O_3). We thus we conclude that the overall stoichiometry of the oxide is ~BO_2.

In all cases, the annealing experiments lead to a band structure and also to core levels that are similar to what is observed for h-BN before oxygen adsorption (but with loss of nitrogen) and the additional oxide features. This behavior depends on the amount of oxygen adsorbed before heating.

We like to note here that the same experiment was also performed for the graphene/Ni(111) system. However, graphene seems to interact more strongly with the Ni(111) substrate, preventing intercalation. Even elevated temperatures do not lead to an intercalation or oxygen bonding. Only increased temperatures and orders of magnitude higher oxygen pressure result in intercalation[81,208], indicating that a kinetic hindrance is the reason for the not observed intercalation with our experimental procedure. However, when oxygen intercalation of graphene is achieved, the Ni(111) surface is subsequently also oxidized, when the preparation route via near ambient pressures is taken. This is not the case for this preparation route that was chosen for the reaction of h-BN, as nickel always is metallic as deduced from the Ni 2p spectra.

6.4 Conclusion

To conclude, we find that we can populate three different regimes of oxygen interaction with h-BN on Ni(111), when the sample is exposed to oxygen with a kinetic energy of ~ 0.7 eV. For oxygen adsorption at 440 K, we observe as the main species intercalated oxygen. Moreover, we find already oxidized parts of the h-BN sheet, which are identified to be mostly a substitution of nitrogen by oxygen, and minor amounts of bonded oxygen. At an adsorption temperature of 600 K, we mainly find the oxidation of h-BN, which results is BO_x ($x = 1, 2, 3$). The three different regimes of interaction is further verified with NEXAFS.

The functionalization of h-BN with oxygen and hydrogen as described in the previous chapters, lead to the question whether oxygen and hydrogen can also react together on h-BN. The reaction both from oxygenated to hydrogenated h-BN and vice versa will be discussed in the next chapter.

7 Reaction of hydrogen and oxygen on h-BN

As the reactivity of h-BN towards atomic hydrogen and highly energetic oxygen was investigated in detail in the previous three chapters, here the co-adsorption of hydrogen and oxygen is investigated. For this, h-BN is exposed to atomic hydrogen (highly energetic oxygen) and subsequently highly energetic oxygen (atomic hydrogen) is dosed. When dosing atomic hydrogen after exposing h-BN to oxygen, a desorption of oxygen is observed, while simultaneously atomic hydrogen binds to h-BN. During the reaction, h-BN is never pristine, but a mixture of adsorbed oxygen and hydrogen is found. For high atomic hydrogen exposure, all oxygen desorbs. If atomic hydrogen is first dosed and subsequently h-BN is exposed to oxygen, we find that oxygen also desorbs hydrogen, however the reaction is incomplete. Also the sticking coefficient of oxygen is lower, when hydrogen is adsorbed on h-BN and the maximum oxygen coverage is decreased. As the reaction can be stopped at any point, we are able to shift the valence band, as well as the core levels, to lower binding energies, anywhere between the shift of hydrogenated h-BN and oxygen functionalized h-BN.

7.1 Introduction

2D materials have become a wide field of fundamental research in the last decade. Due to the discovery of many new 2D materials, such as stanene[215] and blue phosphorus[216], the field of research is still growing. However, fundamental research of the functionalization of 2D materials is still rather limited to the wet-chemical functionalization of graphene. Hexagonal boron-nitride[141,142, 169,197], a hexagonal, alternating arrangement of boron and nitrogen atoms, with a lattice constant of 0.25 nm[217], has already been proposed for several applications, such as gas-barriers for oxygen[218,219] to protective coatings[147]. It was shown that CO_2 and N_2 or H_2 and CH_4 are well separated[220–222] with patterned h-BN membranes. As a protective coating, it is impermeable, even to hydrogen. It is used, to prevent, e.g. oxidation of reactive metal surfaces. The uniform coating of h-BN is also used as a friction reduction layer[147]. Further potential chemical applications are e.g. as a micro reactor[223]: For this, h-BN is grown on e.g. single crystals, or nano-particles[69, 140,224]. Then the reactants are intercalated and the substrate acts as the catalyst [187,225], often leading to an increased activity[209,210,225,226]. Moreover, 2D materials such as graphene and h-BN are used as a template to facilitate ordered growth of nano-particles or clusters[53, 67,227,228]. Here, h-BN is interesting, as it forms Moiré patterns on substrates with a lattice mismatch, leading to deep potential-wells. This facilitates the growth of well-ordered particles and even single molecules can be trapped[68,229].

The rise in 2D materials as fascinating research objects and the interest in new applications also lead to the tuning of their properties by covalent functionalization, although h-BN and graphene are mostly considered to be inert. However, first studies showed that hydrogen and oxygen may bond to the 2D materials and thus be stored, leading to a change of its band structure and reactivity, as also shown in Chapter 4-6. DFT results predict catalytic activity for h-BN on various metal substrates, or for hetero atom doped h-BN[230–233]. Thus, we found it interesting to investigate the chemical bonding and the reaction of chemically bound species on h-BN. Oxygen and hydrogen functionalized h-BN have been studied previously on several substrates[79, 139, 172, 205, 225, 229,234], nevertheless the full potential of switching the functionality has not been shown, or any reaction of the functionalization on supported 2D materials.

We herein report on the reaction of oxygen chemically bound to h-BN and its subsequent reaction by atomic hydrogen and the reverse reaction. We study the system with high-resolution X-ray photoelectron spectroscopy (XPS), near edge X-ray adsorption fine structure (NEXAFS) and temperature programed XPS (TPXPS). We find that all oxygen that is bonded to h-BN reacts with atomic hydrogen, with low amounts of oxygen bonded to defects remaining on the sheet. Interestingly the reverse reaction of bonded hydrogen with oxygen from a supersonic molecular beam is also possible, albeit with significantly lower reaction rate.

7.2 Results and Discussion

In the following, we will present two experiments, in which we react oxygen bound to the h-BN basal plane with atomic hydrogen, and in a second set of experiments we show the reverse reaction of hydrogenated h-BN with molecular oxygen from a supersonic molecular beam.

Reaction of oxygenated h-BN with atomic hydrogen

We first exposed the sample to molecular oxygen with a kinetic energy of ~0.7 eV at a sample temperature of 240 K for 480 s. For oxygen without the additional energy from the supersonic molecular beam no adsorption was found. This exposure results in a single O 1s peak at 531.4 eV and a coverage of ~0.36 ML oxygen bound to the h-BN sheet. Oxygen does not dissociate, but is bonded to two boron atoms in a side on motive. This was shown in earlier experimental and theoretical studies[207] and in Chapter 5.

We then exposed the oxygenated h-BN stepwise to atomic hydrogen. This leads to a decrease in the O 1s intensity, see Figure 7.1 and inset in Figure 7.1a. The oxygen intensity drops nearly linear in the first 3 L, and for higher exposures the rate reduces continuously. The decrease of the O 1s intensity is due to the reaction of molecular oxygen bound to h-BN with atomic hydrogen. We interpret the reduced reaction probability at higher hydrogen exposures as a statistical process, i.e. the reaction becomes less likely for lower oxygen coverages. We do not find any surface intermediates such as OH or H_2O. The reaction occurs most likely through the adsorption at sites close to oxygen, leading to a destabilization of the h-BN oxygen bond. As we will show in the following, the reaction does not proceed via an oxygen and hydrogen free h-BN sheet, but proceeds directly via a partly oxygenated and hydrogenated h-BN.

To further analyze the system, we also gathered data from the N 1s core level, shown in Figure 7.1b. The experiment starts with the N 1s region showing the typical signature of oxygen bound to the h-BN sheet, with two peaks at 397.5 and 398.1 eV, due to a different chemical surrounding of nitrogen atoms in the oxygenated h-BN sheet, as shown in Chapter 5. Upon exposure to atomic hydrogen, we observe a shift of the two peaks to higher binding energy, after the first 0.5 L of exposure. While the signal at 397.5 eV is larger than the one at 398.1 for oxygenated h-BN, we find a gradual change and the peak at higher binding energies becomes larger yielding ~ 2:1 ratio at an atomic hydrogen exposure of 16 L. This N 1s peak shape is typical for h-BN functionalized with hydrogen[139] shown in Chapter 4. The two nitrogen peaks shift continuously to 397.7 and 398.5 eV. In the B 1s core level depicted in Figure 7.1d, the spectrum shows a peak at 190 eV that is typical for oxygen bound to h-BN[235]. Upon hydrogen adsorption, we observe that the B 1s peak shifts to higher binding energy, with a final binding energy of 190.3 eV, being in line with the B 1s binding energy of hydrogenated h-BN. The second contribution that arises during H atom exposure at 189.3 eV, allows us to estimate the hydrogen coverage, although hydrogen itself cannot be observed by XPS. This contribution at 189.2 eV increases constantly during exposure and is thus consequently attributed to boron atoms bound to hydrogen. It reaches a coverage of 0.12 ML at the end of the experiment, see Figure 7.1a for fit. Again, the first spectrum upon exposure of 0.5 L hydrogen shifts towards lower binding energy by 50 meV. For both the N 1s and B 1s core levels, a gradual shift to higher binding energies is found.

This hydrogenated layer was heated to 650 K, in a TPXPS experiment depicted in Figure 7.2a and the quantitative analysis Figure 7.2b, shows that heating the sample results in pristine h-BN. Demonstrating that hydrogen desorbs according to Chapter 4[139]. The spectra in the B 1s and N 1s region in Figure 7.3 show that at no point in the reaction from oxygenated to hydrogenated h-BN the clean surface is present as the spectra of pristine h-BN with N 1s and B 1s peaks at 398.5 and 190.5 eV, respectively are not found. Thus the reaction proceeds via a mixed oxygenated and hydrogenated layer. The results and the assignments to hydrogenated and oxygenated h-BN as well as the intermediate states are also supported by additional NEXAFS measurements.

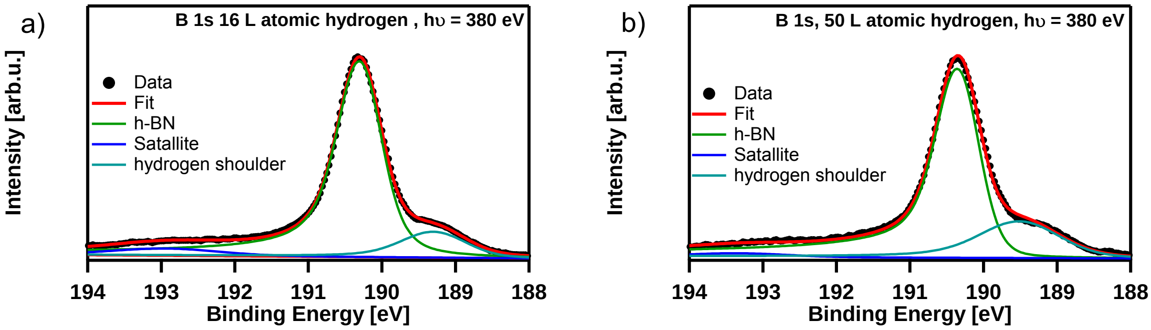

Figure 7.1 Fits of the B 1s core level. (a) 0.12 ML of hydrogen adsorbed on h-BN after desorbing oxygen. (b) 0.2 ML of hydrogen adsorbed on h-BN after an initial exposure of 50 L

For the first 0.5 L of atomic hydrogen, in the N 1s and B 1s in Figure 7.3a and 7.3b core level shifts towards lower binding energies by ~50 meV are found. The peak at lower binding energy increases in intensity and the peak at higher binding energy decreases. In the N 1s region, even the relative peak area changes towards a higher contribution at lower binding energies. We interpret as a coadsorption of hydrogen and oxygen on h-BN. The oxygen coverage of 0.32 ML does not fully saturate the h-BN surface and hydrogen is bound to free sites. We reason that this leads to an additional doping of the h-BN sheet. This results in a peak shift towards lower binding energy, and increase the contributions for sp^3-configured boron neighbors for the nitrogen atoms. For the B 1s spectra, we observe the formation of the shoulder attributed to hydrogen bonding in line with the above argumentation.

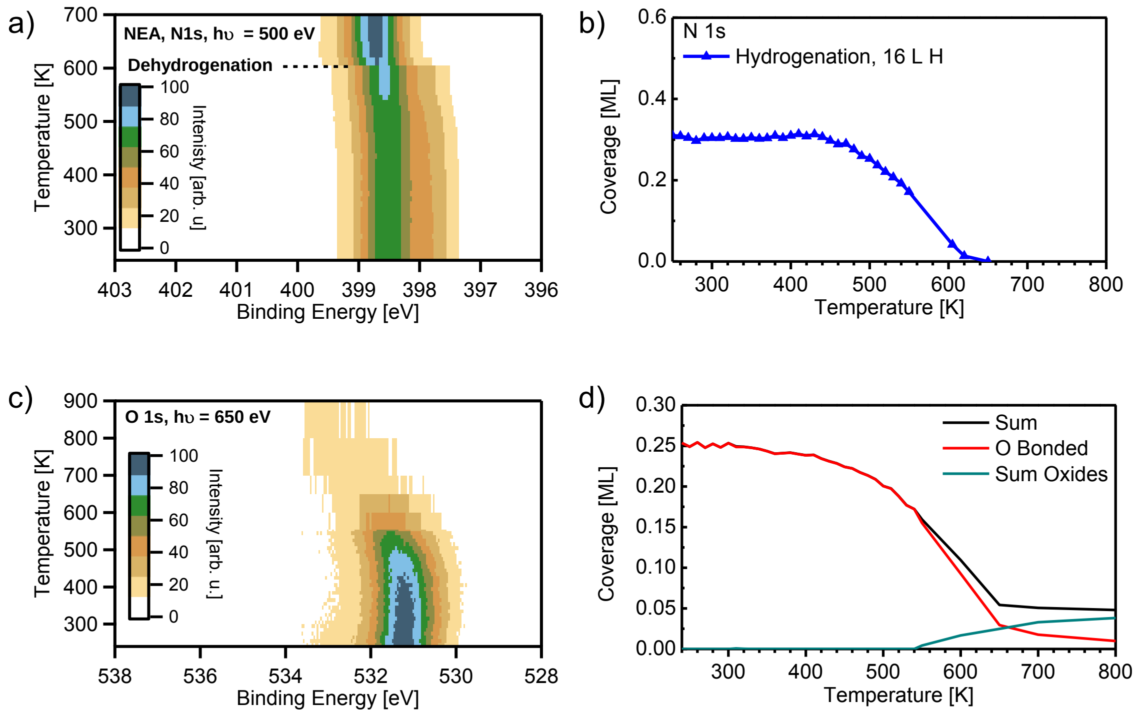

Figure 7.2 (a): Color-coded density plot of the TPXPS experiment conducted in the N 1s core level after reacting oxygenated h-BN to hydrogenated h-BN. The dehydrogenation temperature is marked. (b) quantitative analysis of the experiment shown in (a). (c) Color-coded density plot of the TPXPS experiment conducted in the O 1s core level after hydrogenated h-BN was oxygenated. (d) Quantitative analysis of the TPXPS experiment shown in (c).

In a subsequent TP XPS experiment, the layers formed in the hydrogenation, oxygenation procedures are tested towards their thermal stability.

In Figure 7.4a and 7.4b the TPXPS of hydrogenated h-BN formed by hydrogenation of oxygenated h-BN is shown. The dehydrogenation temperature is within the error the same as in earlier experiments[139]. For the TPXPS of oxygenated h-BN formed by oxygen exposure to hydrogenated h-BN the reaction temperature, i.e. desorption of 50% of the adsorbed oxygen at ~ 570 K, are again the same as reported earlier[235]. We interpret this as an indication that although oxygen is coadsorbed with 0.12 ML hydrogen no adsorbate-adsorbate interactions are observed

Next, we want to discuss the impact of the reaction of atomic hydrogen with oxygenated h-BN on the valence structure of h-BN, as determined by UPS at 75 eV (Figure 7.1c). After oxygen adsorption, we obtain a spectrum with the π-band at a binding energy of 8.9 eV and the σ band that is split at binding energies of 21.5 and 24.3 eV, in agreement with literature[235]. Upon hydrogen exposure, we find that the π- and σ-band continuously shift towards higher binding energies. The final energy of 9.5 eV of the π-band (22.2 eV for the σ-band) corresponds to that of hydrogenated h-BN. Upon heating to 650 K the band structure of pristine h-BN is restored, showing with the π-band at 9.9 eV and the σ-band at 23 eV. This shows that we can continuously shift the band structure of h-BN over 1 eV by a controlled reaction of oxygen with hydrogen. Temperature programmed XPS reveals that the thermal stability of hydrogenated h-BN is identical to that reported in Chapter 4, see Figure 7.2a, 7.2b.

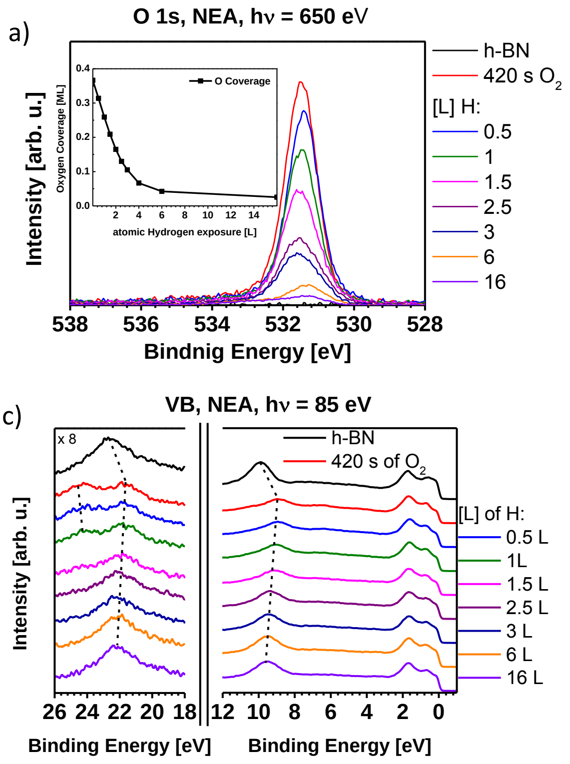

Figure 7.3: Reaction of oxygenated h-BN with atomic hydrogen. (a) O 1s, (b) N 1s, (c) valence band and (d) B 1s region. Red spectrum, oxygenated h-BN with Θ_O=0.32 ML and subsequent hydrogen adsorption steps until only residual oxygen is left on the surface (violet). Inset in (a): quantitative analysis showing the oxygen coverage diminishing with subsequent hydrogen exposure steps.

Reaction of hydrogenated h-BN with molecular oxygen from a supersonic molecular beam.

In this part, we discuss the reverse reaction of hydrogenated h-BN with molecular oxygen with a kinetic energy of ~0.7 eV from the supersonic molecular beam. Data obtained during this experiment are shown in Figure 7.2. We prepared hydrogenated h-BN by exposing it to 50 L of atomic hydrogen, resulting in bonding of hydrogen [139]. This layer is subsequently exposed to oxygen and the results are gathered in situ.

On the hydrogenated sample the prior to exposure to oxygen, no signal is observed in the O 1s region. Upon exposure, we find the growth of a single species at a binding energy 531.4, shifting to 531.3 eV for higher coverages. A small amount of water is observed on the sample (Θ<0.01 ML) at a binding energy of 532.6 eV. After 2557 s, we stopped the experiment at a coverage of 0.25 ML of oxygen, although no saturation was achieved. In comparison to the adsorption of oxygen on clean h-BN, we find that a higher amount of oxygen bound to h-BN (0.32 ML) was achieved after a shorter time 480 s as compared to 2557 s for the hydrogen coadsorbed h-BN. Thus hydrogenated h-BN shows a significantly slower reaction with oxygen as compared to pristine h-BN. The lower reaction rate is attributed to the presence of hydrogen on the sample, which occupies the same adsorption sites and must be desorbed first.

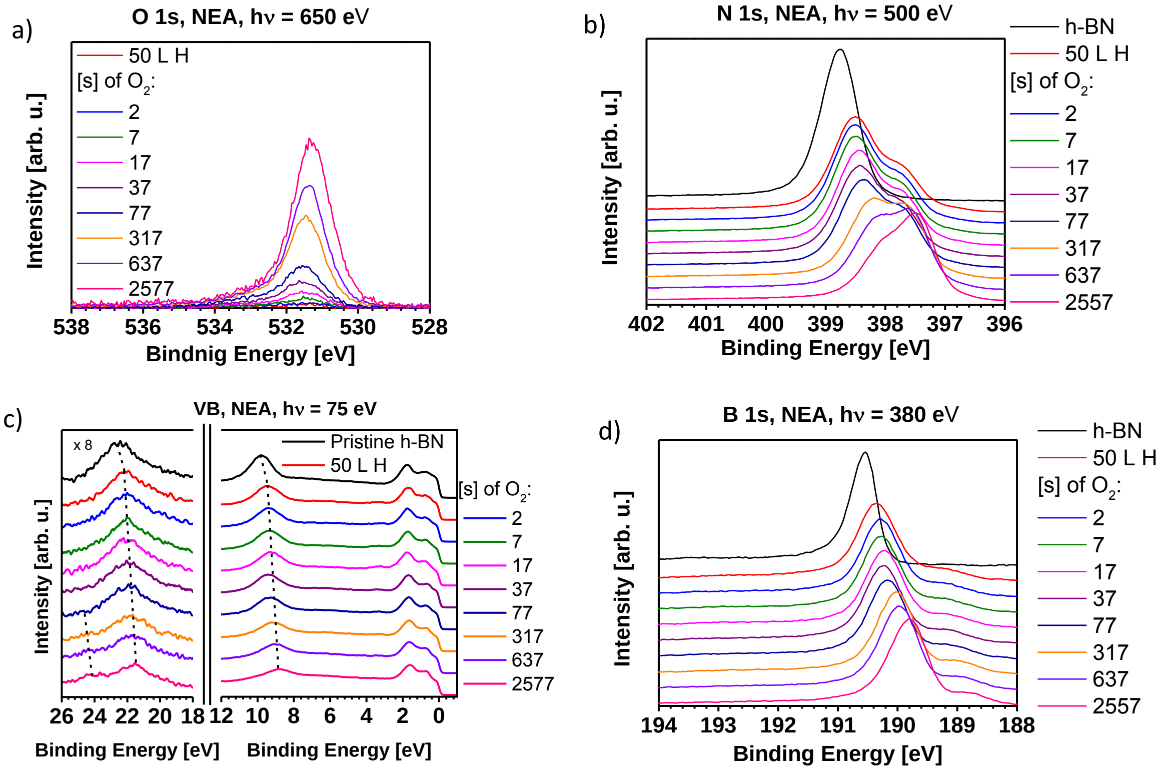

Figure 7.4 Reaction of hydrogenated h-BN with molecular oxygen. (a) O 1s (b) N 1s, (c) valence band and (d) B 1s region. Red: hydrogenated h-BN; violet: after 2557 s of exposure to oxygen, black: pristine h-BN; other: intermediate oxygen exposures.

In the N 1s core level, the experiment starts from two peaks at 398.5 and 397.8 eV with a ratio of ~2:1, i.e. the signature of hydrogenated h-BN[139]. When dosing oxygen, we observe the opposite behavior as described before: the two peak structure remains and the relative intensity changes towards a value below 1. During adsorption, a continuous shift to lower binding energies by ~400 meV occurs, see Figure 7.2b. The B 1s core level at the start of the experiment shows peaks at 190.3 eV and the peak assigned to hydrogen boron bonds at 189.5 eV. From the fit, we can estimate the hydrogen coverage to be 0.2 ML, see Figure 7.1. During oxygen adsorption, we find a shift to lower binding energies to 189.8 eV. The B 1s contribution due to the hydrogen boron bond decreases gradually during oxygen exposure from 0.2 to 0.12 ML, i.e. 40% of the initially adsorbed hydrogen have desorbed within the timeframe of our experiment. In the valence band, for hydrogenated h-BN the π-band is found at 9.6 eV and the σ-band to 22.2 eV. With a continuous reaction towards an oxygenated h-BN layer these values shift to lower values: 8.8 and 21.5 eV (24.2 for the second, split contribution) for the π- and σ-band, respectively, after 2557 s of exposure to oxygen.

The binding energy values for both the N 1s the B 1s region and the valence band do not match the values that were obtained for purely oxygenated h-BN and for the product of the hydrogenation of oxygenated h-BN. This is due to the different amounts of hydrogen and oxygen that are bound to the h-BN plane. However, we do not observe any indication for adsorbate-adsorbate interaction, as we find with the TPXPS an identical desorption temperature for the adsorbed oxygen. The corresponding TPXPS experiment is depicted as a color-coded density plot in Figure 7.2c and the corresponding quantitative analysis in 7.2d.

For graphene, the effect of doping and the resulting shifts in the valence band region and the C 1s core level and its line shape[181] were discussed in detail. It was observed that a rigid band model can be applied, for low doping concentrations, e.g. achievable with hydrogen or oxygen intercalation, while for stronger dopants additional effects are observed. Herein we find that for h-BN the two core levels and the π-band show different binding energy shifts, throughout the two experiments. This is an indication that a rigid band model may be not suitable for h-BN.

We have shown that hydrogenated h-BN can be reacted towards oxygenated h-BN, shown in the second part and that oxygenated h-BN can be reacted to hydrogenated h-BN. With the shown shifts, for both core levels, as well as the valence band, we are now able to conclude that we are able to shift these bands and core levels back and forth, at will, only by changing the adsorbate coverages, without the need to prepare a new sample, or to desorb one adsorbate.

NEXAFS measurements of the coadsorption experiments

To further substantiate our findings presented above NEXAFS measurements were conducted during the two experiments.

Here only the changes observed in NEXAFS spectra during the reaction of oxygenated h-BN to hydrogenated h-BN and vice versa are discussed. The spectra for pristine h-BN are identical to those in literature. For a more detailed description of NEXAFS spectra from hydrogenated h-BN see [139] and Chapter 4. For oxygenated h-BN see Chapter 5[235]. For h-BN, we focus only on the peaks that show changes upon adsorption and reaction. For the boron K-edge (Figure 7.5b, d, f) these features are: the main absorption feature of h-BN at 192 eV, the so-called interlayer states, indicating the h-BN substrate interaction at 193-195 eV (the higher the absorption in this region, the larger the interaction[98,149], and Chapters 4 to 6.) that are a broad absorption feature, indicated with a red double arrow. In the region of the σ^* transitions, two features at 197.5 and 198.5 eV are observed[205]. For the nitrogen K-edge (Figure 7.5a, c, e) the feature, we want to discuss are the interlayer states from 396.5 to 398.5 eV (marked with a red double arrow), as these show clear changes upon reaction and the σ^* transitions at 408.5 and 415 eV that show typical intensities depending on the adsorbate on h-BN.

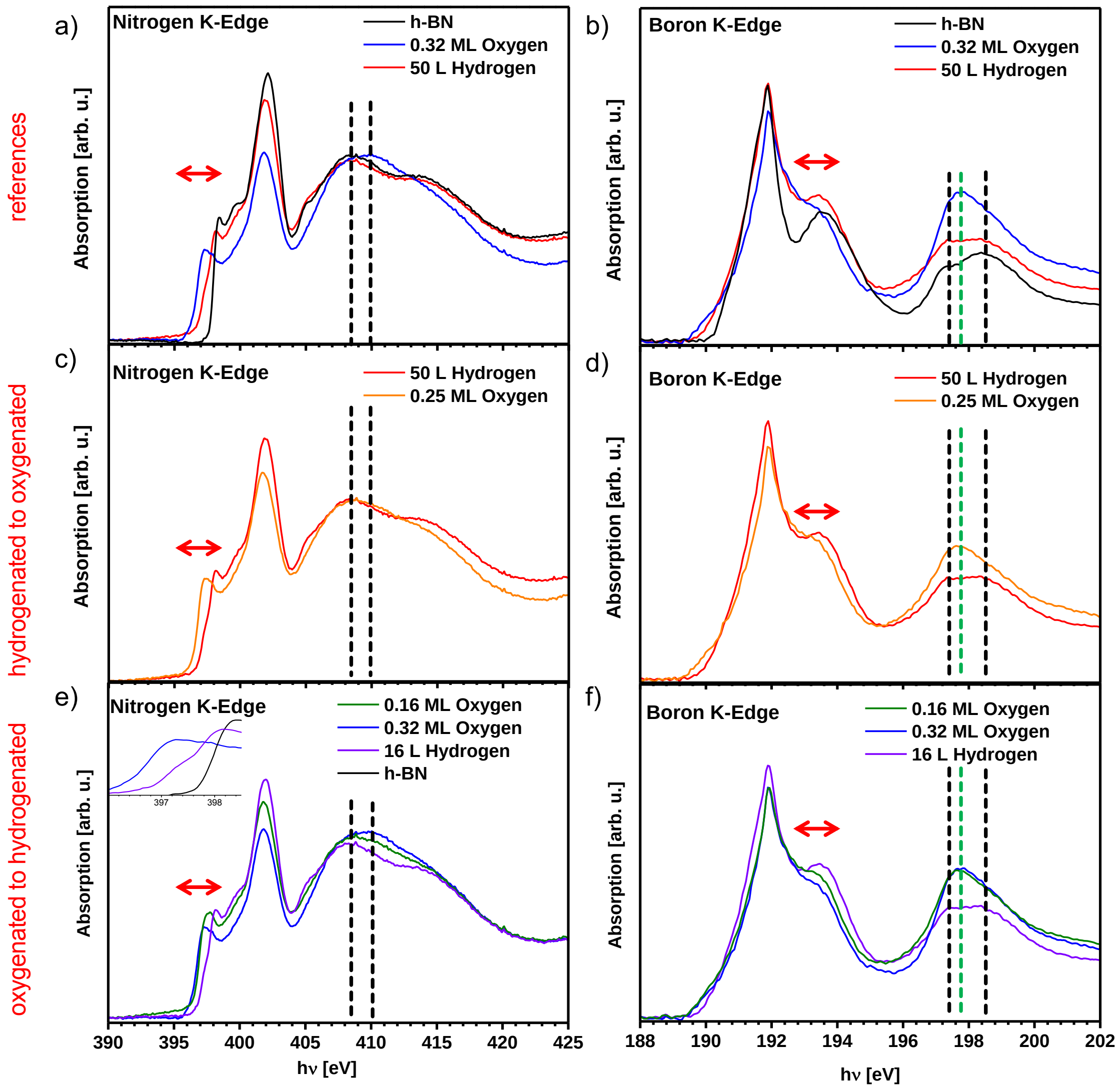

Figure 7.5 NEXAFS spectra of the (a) boron K-edge and (b) nitrogen K-edge of pristine h-BN (black), hydrogenated h-BN (red) and oxygenated h-BN (blue). The preparations are according to the experiments discussed. Oxygen adsorption on hydrogenated h-BN is shown in (c) for the N K-edge and in (d) for the B K-edge. Red: hydrogenated h-BN; Hydrogenated h-BN with an additional 0.25 ML of oxygen. Atomic hydrogen adsorption on the oxygenated h-BN is shown in (e) for the N K-edge and (f) for the B K-edge. Blue: oxygenated h-BN; Green: Oxygenated h-BN after ~3 L of atomic hydrogen with Θ_O=0.16 ML; Violet: after the reaction, with 16 L hydrogen dosed.

Figure 7.5a, 7.5b depicts the NEXAFS spectra obtained for the starting points of the experiments, i.e. hydrogenated h-BN, oxygenated h-BN and pristine h-BN. At the N K-edge pristine h-BN shows features starting at ~ 398 eV followed by the π* transition at 402 eV. The σ* star region shows two absorption features at 408.5 and 415 eV. Hydrogenation leads to an increase in intensity in the interlayer state region, leading to an onset at ~ 397.5 eV. The π* transition is slightly less intense, while the σ* star region is unaffected by hydrogenation. Oxygenation leads to an stronger shift in the absorption onset to 397 eV. The intensity of the π* transition is lower, compared to hydrogenation and in the σ* star region only an asymmetric peak at 408.5 eV is observed.

At the B K-edge for pristine h-BN, the π* transition is located at 192 eV followed by the interlayer region, which is indicative for the interaction of h-BN with the substrate. At 197.5 and 198.7 eV, a double peak of the σ* star region is found, while the peak at lower photon energies shows lower. For hydrogenated h-BN, the interlayer states increase in intensity and an increase of the peak at 197.5 eV in the σ* star region is observed, which leads to two peaks with a similar height. In the case of oxygenated h-BN, the peak attributed to the interlayer states shifts to lower photon energies by 1 eV and becomes less resolvable. Furthermore, in the σ* star region only one asymmetric peak at 197.7 eV is found.

For the reaction of hydrogenated h-BN (exposed to 50 L hydrogen) with oxygen, the NEXAFS spectra are shown in Figure 7.5c and d. These show characteristic changes, similar to these observed for pristine h-BN exposed to oxygen, as shown in Chapter 5. At the N K-edge, the interlayer region for h-BN with 0.25 ML of oxygen shows significant changes, in particular the onset of the absorption shifts to lower photon energies by ~1 eV. This lower onset is a fingerprint of oxygen – h-BN bond formation, as shown in Chapter 5. Furthermore, the contribution in the σ* star region at 415 eV shows a lower intensity, leading to the asymmetric peak at 408.5 eV typical for oxygenated h-BN. Similarly, changes at the B K-edge are observed: a decreased contribution in the interlayer region and a shift of this absorption feature towards lower photon energies. Moreover, in the σ* star region, a change from the two peaks of hydrogenated h-BN at 197.5 and 198.7 eV to an asymmetric contribution at 197.7 eV is present. This shows that the characteristic spectral features of hydrogenated h-BN change to the features of oxygenated h-BN. Thus a reaction from oxygenated to hydrogenated h-BN is observed.

The reverse reaction, i.e. the hydrogenation of oxygenated h-BN is shown in Figure 7.5e and f. The experiment begins now with oxygenated h-BN, with an oxygen coverage of

0.32 ML. During the experiment, at an oxygen coverage of 0.16 ML additional NEXAFS spectra are recorded. In the end of the experiment, after 16 L of atomic hydrogen were adsorbed, also NEXAFS spectra were recorded. At the N K-edge, the onset of the absorption in the interlayer state region shifts to lower photon energies, with decreasing oxygen coverage. When 16 L of hydrogen are adsorbed only a shoulder is found in the interlayer region, see inset in Figure 7.5e. This is a characteristic fingerprint for hydrogenated h-BN. The intensity of the main π* transition, at 402 eV, increases continuously during the experiment. In the σ* star region, at 0.16 ML we find only a slight decrease in intensity, while the complete removal of oxygen leads to the formation of two clearly distinguishable peaks at 408.5 and 415 eV, typical for hydrogenated h-BN, as shown in Chapter 4.

At the B K-edge, the reaction of oxygenated h-BN to hydrogenated h-BN leads to a gradual increase of absorption in the interlayer region, which is marked with the red double arrow. In the σ* star region (197 to 200 eV) no changes are observed after desorbing 0.16 ML of oxygen and only after complete removal of oxygen the two absorption features at 197.5 and 198.7 with the same intensity are seen. As discussed above, this is a fingerprint for hydrogenated h-BN.

This strongly indicates that the reaction is possible in both directions from hydrogenated h-BN to oxygenated h-BN and vice versa, as deduced here by NEXAFS, and above from XPS.

7.3 Conclusion

In summary, we find the reaction of oxygenated h-BN with hydrogen and hydrogenated h-BN with oxygen is possible. The reaction of oxygenated h-BN with atomic hydrogen results in a complete desorption of oxygen. The subsequently obtained h-BN layer is hydrogenated and during the reaction a mixed hydrogenated and oxygenated layer is present. From this we conclude that hydrogen adsorbs both on empty adsorption sites with a high initial sticking coefficient, and reacts with oxygen in a statistical manner. From the recoded core level shifts in the N 1s, B 1s and valence band regions, we are able to show that a rigid band model may not be adequate for h-BN. For the reaction of hydrogenated h-BN with oxygen, with a kinetic energy of 0.7 eV, we are able to observe that oxygen most likely binds first to free adsorption sites. Subsequently a slow reaction begins, resulting in desorption of hydrogen. Furthermore, the results show that with the arbitrarily exchangeable adsorbates hydrogen and oxygen, it is possible to shift the core level binding energies and the valence bands of h-BN, depending on the amount and type of adsorbate, while h-BN is largely functionalized during the experiment. We interpret the in here gathered results a step forward, towards the design of band structure of 2D materials.

8 Covalent functionalization of 2D materials with methyl iodide

h-BN is exposed to a beam of highly energetic methyl iodide (MeI). Upon exposure, the formation of a short lived iodine species, and polyiodines in the I 4d core level is observed. In the C 1s region, several species, which are attributed to MeI multilayers, and two species for CH_3 bonded to nitrogen and boron in h-BN, are found. The former desorbs in a temperature programmed experiment, while the later starts to lose hydrogen during heating, resulting in CH_2 CH and C, all bonded to boron. In the I 4d core level, it is observed that during heating the polyiodine species decompose to iodine (I_2) and desorb, with small amounts of iodine intercalate. In the B 1s and N 1s core levels, these reactions only result in a small shoulder at lower binding energy. The same experiment was repeated for graphene on Ni(111). Here, also indications for the same type of reaction were observed; however, a detailed observation of the CH_3 fragment of MeI is impossible due to the large contribution of the carbon backbone of graphene, present at a similar binding energy. Subsequently, the sample is heated and temperature programmed XPS reveals the stability of the bonded species. For h-BN, we observe iodine species on the sample up to 850 K and carbon species up to 750 K. For graphene, we observe iodine containing species up to 450 K and are able to indirectly identify bonded species to the carbon backbone of graphene up to 350 K. From these high desorption temperatures and characteristic reaction behavior, we conclude that we have achieved a covalent functionalization in a clean, ultra-high vacuum approach.

8.1 Introduction:

Graphene and *hexagonal* boron-nitride (h-BN) have been extensively studied, due to their unique physical and chemical properties such as endurance of high strain[11], gas impermeability[28] protective coating[115, 147,209] - with various results - gas separation[26,27], gas sensing[21,236,237]. Graphene is a semi-metal, with theoretically zero charge carrier density at the Dirac point, however, without a bandgap[73, 129,238–240]. On the other hand, although isoelectronic to graphene, h-BN is an insulator with a wide band gap of theoretically 5.4 eV in its free standing form[77,140]. Already from these properties, combined with the ballistic electron transport in graphene, one can immediately see, the potential these materials hold for the future of the semi-conducting industry as a semiconductor and dielectric. However, one must be able to tune and design their electronic properties as needed[241,242]. This is especially interesting, since it was shown that graphene can be grown on h-BN[97,145]. The tuning of the electronic structure for both 2D-materials has advanced greatly over the last years. Intercalation of various alkali and earth alkali metals beneath graphene[189,243] and h-BN[194, 197,198,244,245] has proven to be a powerful tool to manipulate the electronic structure. Intercalation of hydrogen and gold on various metal surfaces gives both 2D-materials a free standing character, which is stable over a wide temperature range[42, 44, 109, 193,246–248]. Adsorption of various organic molecules or incorporation of donor atoms into the lattice proved to dope graphene substantially, making it more interesting for semiconducting applications[110, 122, 176, 182,249]. More recently, chemical covalent functionalization under controlled condition, i.e. ultra-high vacuum (UHV), has been reported, with various functional groups. This covalent functionalization is a route, which provides both a wide range of possible molecules to attach and a high thermal stability, due to the formation of a chemical bond. Hydrogenation, which proved to be highly dependent on the substrate supporting the 2D-material has been shown for graphene, for example on Ni(111)[42,109], Ir(111)[129] and many other surfaces[43, 121, 138, 158,250]. The interaction of atomic hydrogen with h-BN has also been extensively studied on Ni(111)[139]. Fluorination is also achieved for graphene, changing the electronic structure dramatically[251]. Methylation has also been shown recently, however, not under UHV condition[9,49], or with transferred samples[252]. Very recently, porphyrin-functionalized graphene has been reported, induced via current injection with a scanning tunneling microscope tip[65]. However, methylation under UHV conditions with an in situ grown 2D-material has not been achieved, to our knowledge.

In this work, we use methyl iodide (MeI) as a reagent to react with graphene and *hexagonal* boron-nitride (h-BN). As the carbon-iodine bond is weak due to its elongated and non-covalent nature, we hope to easily induce a breaking of the bond either homolytically to form a methyl and iodine radical, or in a hetorolytic manner to form a positive charged CH_3^+ species and an I^- species. We expose the Ni(111) single-crystal that is covered either with graphene or h-BN to a MeI beam fed through a heated, seeded, supersonic molecular beam (SSMB). The adsorption is monitored in-situ with high-resolution X-ray photoelectron spectroscopy (XPS). We observe the accumulation of various iodine and carbon containing species. Subsequently, we heat the sample to probe the thermal stability of the adsorbed species with temperature programmed XPS (TPXPS). We find that for graphene, iodine- and carbon-containing species desorb before 550 K, while for h-BN we find iodine species up to 800 K and carbon species up to 750 K.

8.2 Results and discussion

MeI adsorption on h-BN:

h-BN was exposed to the seeded molecular beam of MeI. During the exposure, we probe each core level (C 1s, I 4d, N 1s and B 1s) in a separate experiment. In the following the C 1s and I 4d core level will be discussed in detail, as will be the quantitative analysis of these core level spectra. Characteristic spectra of the N 1s core level are shown in Figure 8.1.

Adsorption of MeI onto h-BN (MeI/h-BN/Ni(111))

C 1s core level

Selected data of the C 1s level, for the adsorption of MeI are shown in Figure 8.1a.

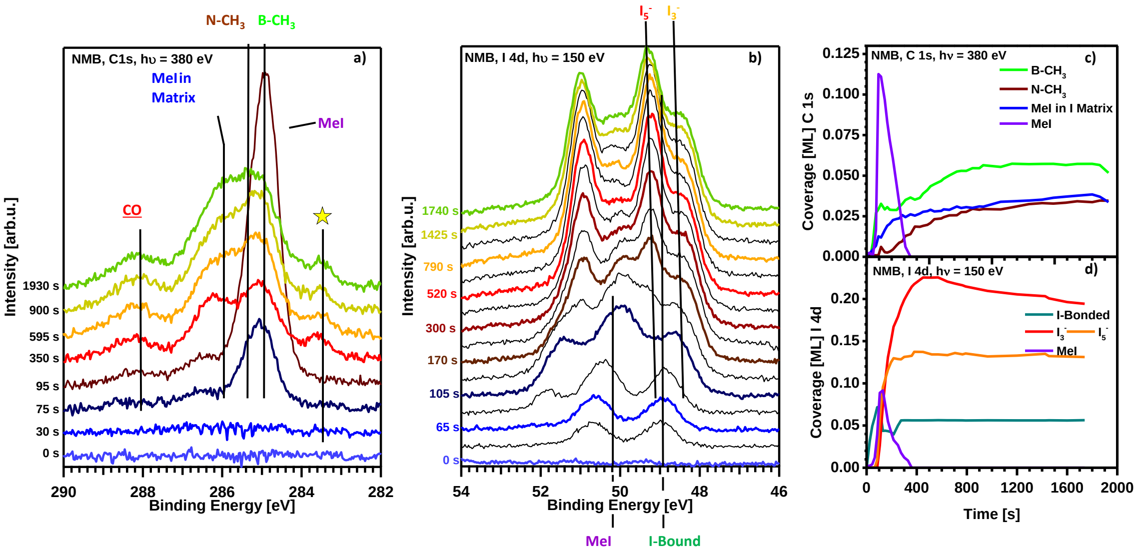

Figure 8.1: Adsorption of MeI on h-BN monitored with high-resolution XPS: (a) selected spectra of the C 1s region. Irradiation-induced fragments marked with a yellow star. (b) selected spectra of the I 4d core level. The solid lines indicate the binding energy of the observed species. Please note that the I 4d signals are spin-orbit split. (c) Quantitative analysis of the data shown in (a); (d) quantitative analysis of the data shown in (b). For the quantitative analysis the coverage in the C 1s core level was referenced to a closed layer of graphene on Ni(111) consisting of 2 ML carbon per nickel unit cell. The amount of iodine was calculated by taking into account the photoionization cross section of the I 4d core level.

The following changes are observed during adsorption. After 75 s, we observe the formation of two peaks at 285.1 and 286.5 eV. These peaks form only after iodine is found on the sample, see discussion of the I 4d data. The peak at 285.1 eV increases until 95 s (brown spectrum in Figure 8.1a, then it reaches saturation and subsequently decreases sharply, until it completely vanishes after 350 s. This decrease is well observable in the spectra taken at 95 s, when the peak is the main contribution to the spectrum, while at 350 s it is completely gone. This is also reflected in the quantitative analysis in Figure 8.1c. This species is not stable without the high MeI flux of the SSMB, additionally it vanishes, depending on the adsorbates on the surface. This strongly suggests that MeI is physisorbed and that in the beginning of the experiment iodine species on the surface have a significant stabilizing effect. The second species, again only stable in the presence of iodine is assigned to MeI on h-BN, as the thermal stability suggests no covalently bound species, see discussion of the TPXPS data.

Starting at 75 s, two additional species derived of MeI become stable on the surface at binding energies of 285.2, and 285.7 eV. From their thermal stability and their relative binding energy we conclude that these are assigned to CH_3 bonded to boron (B-CH_3) and nitrogen (N-CH_3), respectively. The chemical shift is expected due to the relative electronegativity of boron and nitrogen.

A quantitative analysis of the adsorption experiment was performed: see Figure 8.1c. The first species to bond to the surface is B-CH_3, which is in line with Chapter 4, 5, 6 and 7 that showed that functionalization occurs preferably at boron atoms on h-BN on Ni(111). After 75 s, the species, we identified as physisorbed MeI is found in addition to the B-CH_3 groups, with a coverage of 0.03 ML. B-CH_3 populates in the beginning of the experiment, and is also the dominant species at the end of the adsorption; this indicates that it is the energetically most favorite species. Previous calculations for the adsorption of hydrogen by Koswattage et al[98,149]. and Späth et al.[139] (Chapter 4) show that the most stable adsorption site is unambiguously the B-CH_3 (B-H calculated) adsorption species, which fits well to our observations here. Furthermore, in the TPXPS data we find a chemical conversion of this species, while all other species desorb due to their only weak interaction.

This physisorbed MeI further increases rapidly, until it reaches a maximum coverage after 95 s, with a coverage of 0.11 ML and subsequently vanishes completely until 350 s. The B-CH_3 (green) species increases rapidly in the first 75 s, however, stays constant at a coverage of 0.03 ML, unaffected by the amount of MeI on the surface. Subsequently, it increases further after all MeI is desorbed, to 0.05 ML, until the end of the experiment. MeI interacting with adsorbed iodine (blue) shows an increasing coverage in the beginning of the experiment to 0.03 ML at 350 s, and then slowly increases to 0.04 ML, until the end of the experiment. The species attributed to N-CH_3 shows a similar behavior and displays the same saturation coverage, as MeI interacting with iodine. The formation of N-CH_3 becomes possible due to the formation of highly reactive MeI fragments, thus decreasing the selectivity of the reaction dramatically, thereby also less favorable adsorption sites can be populated, especially when the surface becomes more crowded and the preferred adsorption sites cannot be accessed anymore.

Furthermore, we find two more species at 283.7 and 288.1 eV that are due to radiation-induced fragmentation (marked with a yellow Star) and the adsorption of CO. The formation of synchrotron light induced reactions was studied intensively. The adsorption of CO from the residual gas and minor impurities from the SSMB is unusual at 170 K. This shows that the modification of the surface with iodine species also allows for the adsorption of molecular species such as CO. Further support for the adsorption of CO comes from XPS data in the O 1s region. The latter two species are omitted for clarity in Figure 8.1c; their coverage stays below 0.015 ML and 0.01ML, respectively, throughout the experiment.

I 4d core level

Next, we want to discuss the I 4d core level spectra. Please note, that due to the character of the probed core level, a spin orbit splitting of the signals is observed, with a splitting of 1.7 eV, thus doubling the amount of peaks observed. In the beginning of the experiment, as seen in Figure 8.1b, for the spectrum recorded at 65 s, we find exclusively one species at 49.0 (50.7) eV that we assign to iodine bonding to h-BN. In the quantitative analysis shown in Figure 8.1d, we find a strong increase up to 85 s and a coverage of 0.07 ML. Interestingly, no corresponding carbon species is found in the first 30 s, suggesting that an adsorption of iodine is necessary for further adsorption and reaction. Moreover, either C_xH_y species desorb from the surface after cracking of MeI, or it partly decomposes in the SSMB, liberating iodine species that stick to the h-BN surface.

After 100 s, three additional species appear at 48.5 (50.2) 49.3 (51.0), and 49.9 (51.6) eV, see Figure 8.1d. The species at 48.5 (50.2) and 49.3 (51.0) eV are attributed to polyiodides, namely I_3^- and I_5^-, respectively. The polyiodides form due to the increased iodine coverage (concentration) on the surface, as is also known from solution chemistry, and was also predicted from theory[253]. The calculations also predict the experimentally found behavior that only after a certain surface concentration of iodine is reached polyiodides form. Theory predicts that at least 12.5% (i.e. 0.25 ML) of graphene have to be covered with iodine, to start the formation of polyiodides. However, we observe the formation of polyiodides, in particular I_3^-, already at a coverage of 3.6% (0.072 ML). The lower value is attributed to the fact that we use supported h-BN sheet and that further adsorbates such as CH_3 are on the surface. This leads to a confinement and additional electron density that facilitates the formation of polyiodines. The assignment of the I_3^- and I_5^- species is due to their respective relative charge per iodine atom, i.e. the higher the charge, the lower the binding energy (more reduced) and the fact that a higher concentration of iodine allows for the formation of larger polyiodine molecules. Thus, I_3^- is at a lower binding energy and is found at lower iodine coverages, compared to I_5^-, which is found at higher binding energies and requires a higher iodine coverage to from.

The polyiodides saturate at 215 s (I_3^-) and 450 s (I_5^-) at a coverage of 0.23 and 0.13 ML, respectively. The species at 49.9 (51.6) eV behaves similar during adsorption (see Figure 8.1c and d, which leads to the assignment to iodine from physisorbed MeI. A further support to the assignment to physisorbed MeI is the fact that the signal of bonded Iodine is damped by the physisorbed MeI, while the dampening is lifted upon desorption of the physisorbed MeI. After the adsorption experiment, we find 2.5 times the amount of iodine on the surface as compared to carbon. Please note that small amounts of oxygen are bonded to h-BN under the conditions of the SSMB. For the discussed experiments ~ 0.05 ML of oxygen were found, which did not have a significant influence on the surface chemistry MeI on h-BN.

N 1s core level

In the N 1s core level a shift of the main peak of h-BN upon adsorbing MeI for 335 s by 0.24 eV is observed and by 0.33 eV at the end of the experiment, as shown in Figure 8.2. A shoulder at a binding energy of 397.9 eV forms during the experiment. This shoulder is attributed to MeI interacting with h-BN. The signal intensity at the end of the adsorption experiment decreased to 48%, attributed mainly to damping of the photoelectrons by adsorbed iodine.

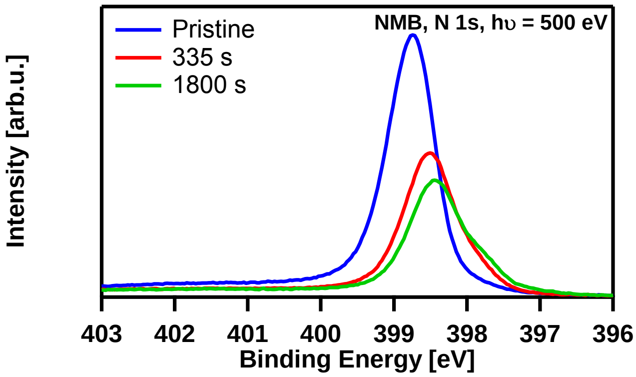

Figure 8.2 Characteristic spectra recorded in the N 1s core level region of h-BN adsorbed on Ni(111) recorded during MeI adsorption.

Temperature programmed XPS (TPXPS) of MeI adsorbed onto h-BN

To further characterize the surface species and determine their thermal stability we performed temperature programmed XPS (TPXPS) measurements. Such experiments allow for investigating the stability of the functionalization that is important for potential applications. Additionally, further information on the species is gained, needed to verify our assignments.

C 1s core level

Spectra recorded in the C 1s core level are depicted in Figure 8.3a and the corresponding quantitative analysis is depicted in Figure 8.3c. Beginning at 200 K, the contribution for MeI interacting with Iodine, i.e. physisorbed, at 286.4 eV (blue in Figure 8.3c) decreases and desorbs completely until 230 K. This desorption occurs simultaneously with the desorption of the polyiodides from the surface, thereby the stabilization from the polyiodided for this species is not present anymore, see discussion of the I 4d core level below. Along with this desorption, N-CH_3 at 285.7 eV (bright green in Figure 8.3c) shows the same behavior. This suggests that also N-CH_3 is a weakly bonded species that needs lateral interactions with iodine to be stable on the surface. No spectral evidence for a further reaction of N-CH_3 is found.

Beginning at 210 K, also the contribution for B-CH_3 decreases rapidly and vanishes completely at 230 K. At 240 K we obtain a single, asymmetric peak located at 285.2 eV, which we assign to B-CH (green in Figure 8.3c). We also considered other reaction pathways, e.g. formation of B_2-C_2H_4, B-C_2H_4-N or only the loss a single hydrogen; a reaction to B-CH_2. However, these are unlikely reaction products. Formation of C_2H_4 was only observed on bare Ni(111)[254], while a CH_2 intermediate is also not stable on Ni(111). Please also note that any carbon fragments that could form on Ni(111), such as C_yH_x ($y = 1, 2$; $x = 0,1,3,4$) have a different binding energy and desorption temperature. The maximum coverage of this species observed is 0.07 ML. With increasing temperature, this single peak observed at 240 K starts to shift to higher binding energy, which we attribute to the formation of carbon bound to boron in the h-BN layer, i.e. B-C. An additional shift in binding energy is expected due to the desorption of iodine at the reaction temperature.

B-C is the only remaining carbon species on the surface above 450 K with a coverage of ~0.05 ML. It is observed on the surface until 780 K. Whether this carbon is incorporated into the 2D lattice of h-BN, as a dopant or, if it is bonded to the vacuum side cannot be determined. However, as carbon is most likely not desorbing from the surface, it has to diffuse into the Ni(111) bulk. This will be further discussed in the interpretation of the UP spectra.

From our data, we conclude that a similar reaction of CH_3 adsorbed onto h-BN occurs, as on metal surfaces, e.g., on, Pt(111) or Pd(111).

I 4d core level

The spectra recorded during TPXPS experiment, are shown in Figure 8.3b and c, the corresponding quantitative analysis in e. During the heating experiment, we observe that the two poly iodine species, I_3^- and I_5^- (48.4 eV and 49.3 eV), start desorbing at 190 K and vanish completely at 300 K. This desorption leads to an apparent increase in bonded iodine coverage to 0.06 ML, because the polyiodides do not damp the signal anymore. After 310 K, the contribution for the bonded iodine species decreases, i.e. desorption is observed and the binding energy shifts to 49.5 (51.2) eV (dark green in Figure 8.3e). The coverage now is only 0.02 ML, thus 2/3 of the iodine desorbs. This bonded iodine is highly temperature stable and observed up to 850 K. It shows a different binding energy and thermal stability as iodine adsorbed on Ni(111), which is observed up to 970 K. This also shows that the h-BN layer is still intact. A table for the observed species is given below in Table 8.1.

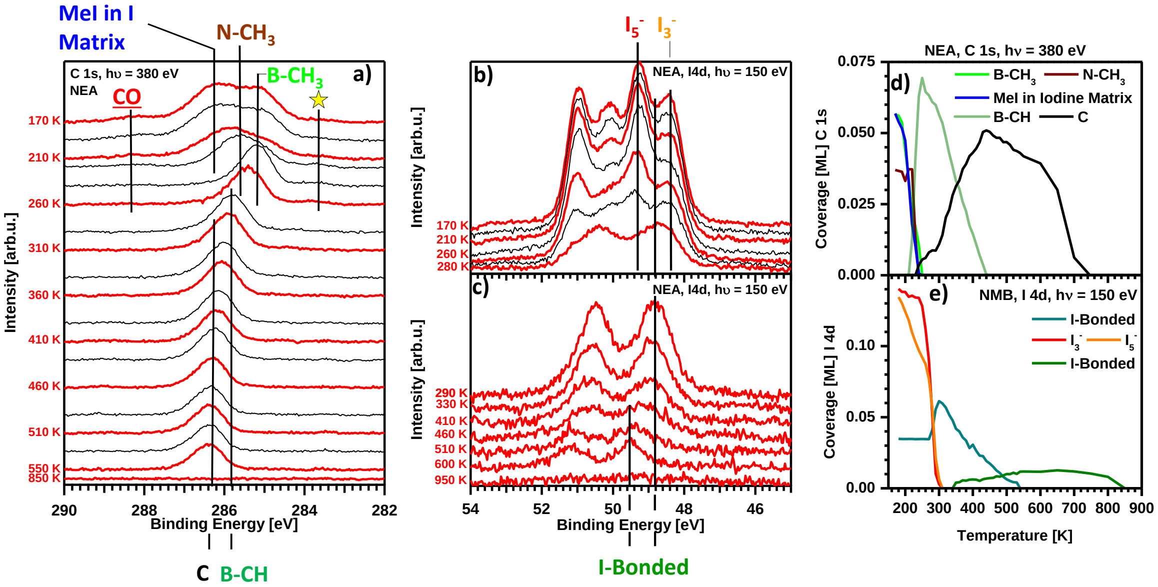

Figure 8.3: Selected spectra of the heating experiment of MeI adsorbed onto h-BN/Ni(111) and the quantitative analysis. (a) C 1s region. Irradiation induced fragments are marked with a yellow star. (b) I 4d region up to 280 K; (c) I 4d region above 290 K. Results of the quantitative analysis for the C 1s core level in (d) and for the I 4d core level in (e).

To conclude the findings in the I 4d core level region: Upon exposure of the sample to accelerated MeI the following is observed: First, reactive iodine species are generated, binding to h-BN (I-bonded, dark green Figure 8.1d. Subsequently, we find physisorption of molecular MeI. Then, due to the high iodine concentration on the surface both I_3^- and I_5^- are formed. However, upon formation of these polyiodine species the physisorbed MeI species starts to desorb, so that after adsorption experiment only poly iodine and bonded iodine is found in the I 4d core level spectra. When the sample is subsequently heated, we find the following changes: I_3^- starts to desorb, beginning at 190 K. At 230 K also I_5^- desorbs and the signal attributed to the bonded iodine is de-damped. Beginning at 310 K, also the bonded Iodine starts to desorb; however 1/3 reacts to a species, with a distinctively different higher binding energy. This species is temperature stable up to 850 K and is more oxidized.

We like to shortly compare the I 4d and C 1s core level: The quantitative analysis shows that both core levels display a different reaction behavior during the adsorption, as well as, during the TPXPS experiment. The only species found on the surface that contains both iodine, and carbon is the meta-stable MeI species observed shortly during the adsorption. For all other species the obtained data indicates that they are separately bound. We also find a large excess of iodine on the surface in the form of poly iodine. However, it should be noted that the contributions for the poly iodine likely also contain the signal of MeI interacting with iodine in the I 4d core level. However, an unambiguous deconvolution is not possible, as this signal should be rather small, when considering the amount observed in the C 1s core level region.

Table 8.1 Observed species ordered by binding energy, from low to high for the C 1s and I 4d core level.

C 1s		I 4d	
Species	Binding Energy [eV]	Species	Binding Energy [eV]
Beam Damage	283.7	I_3^-	48.4
MeI	284.9	Bound I (1)	48.9
B-CH_3	285.0	I_5^-	49.3
B-CH	285.3 - 285.9	Bound I (2)	49.5
N-CH_3	285.7	MeI	49.9
MeI in I Matrix	286.3		
C	286.3 - 286.5		
CO	288.1		

Valence band spectra (UPS)

For additional spectroscopic insight, we used ultraviolet photoelectron spectroscopy in a temperature dependent manner to study the electronic structure of the functionalized of the h-BN layer. Selected spectra recorded at the Γ-point are shown in Figure 8.4.

From 0 to 3 eV, the Ni(111) metal d-orbital states appear in the spectrum. The σ-band region of h-BN is located between 3 to 7 eV in the spectra -marked in green- and the π-band region is located from 8 to 12 eV, marked in brown. Upon adsorption of MeI, the following changes in the UP spectra are observed: The spectra are damped to 60% of their intensity, compared to pristine h-BN. In the region of the σ-band, we find an additional peak at 4.2 eV (marked (I)), located at lower binding energy, than the pristine σ-band. We do not observe any new features or a large shift to lower binding energy in the π-band region, thus making intercalation unlikely. Upon heating from 170 to 250 K, feature (I) shifts to 3.6 eV (II). Upon further heating, (II) diminishes, until at 470 K, when it is no longer observable. With the decrease of (II) a feature in the π-band region is observed (marked as (III)), located at 8.4 eV. (III) is observed form 438 until 700 K and vanishes completely between 700 to 750 K. The spectrum of pristine h-BN at low temperature is similar to that taken at 850 K, after all carbon and iodine containing groups have desorbed from the surface.

We like to note here that UPS data is not easily interpretable, as the new states have not been studied further. However, the temperatures, at which reactions were observed in the UP spectra fit to those described above observed, in the C 1s core level: The shift from (I) to (II), occurring from 170 to 250 K, also occurs in the C 1s core level, as the reaction from B-CH_3 to B-CH. The reaction of (II) to (III) from 438 to 490 K fits to the reaction of B-CH to B-C. Lastly, the temperature, when (III) vanishes fits to the disappearance of the B-C species in the C 1s. The formation of (III) together with the remaining single peak in the C 1s region, leads us to believe that we more likely observe the formation of a quasi-free-standing graphene – like structure, i.e., graphene on h-BN, instead of doped h-BN.

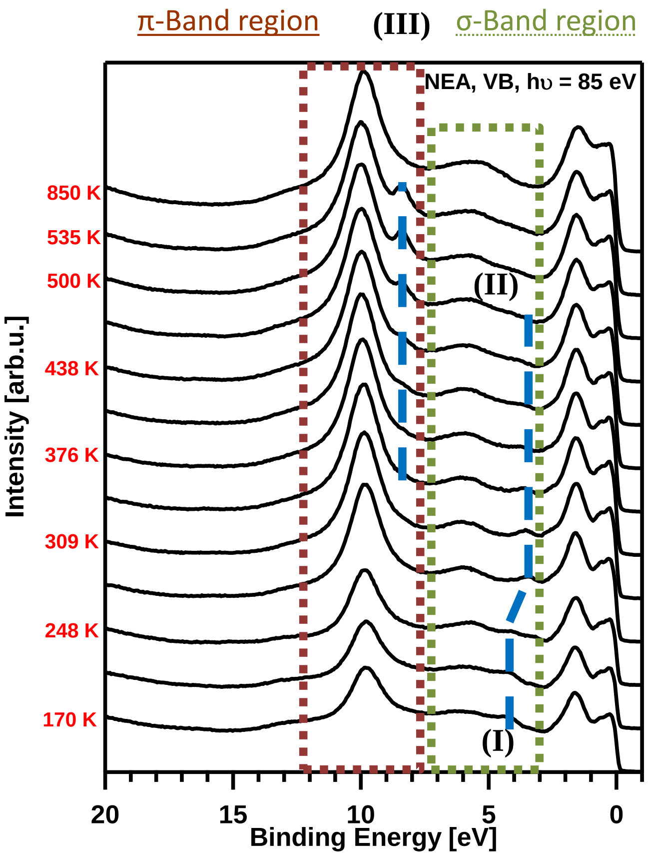

Figure 8.4: TPUPS spectra of MeI adsorbed on h-BN. The σ-band region is marked in green; the π-band region is marked in brown. The additional peaks found, not observed for pristine h-BN are marked with blue dashed lines and roman numerals. The reaction from (I) to (II) is observed from 248 to 470 K. (III) starts to form at 438 K.

Adsorption of MeI on graphene

Graphene is grown on Ni(111) by chemical vapor deposition of propylene. Subsequently it was exposed to MeI from the supersonic molecular beam, also with an energy of 0.25 eV similar to the experiments with h-BN. Please note that graphene on Ni(111) shows three contributions in XPS, namely one peak for the bridge top adsorption geometry, located at 284.9 eV and two peaks for top fcc adsorption geometry, located at 285.0 and 284.5 eV[50]. We will discuss spectra taken before and after the adsorption of MeI for 5 min. The functionalized graphene surface was then heated with a linear heating of 0.5 K/s ramp and spectra were recorded every 10 K.

C 1s core level region:

A spectrum recorded before (denoted pristine), after the adsorption (Figure 8.5a, 150 K) and selected spectra recorded during the heating experiment are shown in Figure 8.5a. The analysis of the data is challenging, as the strong signal of graphene is overlaying the new, small signals.

In the C 1s core level spectra, we observe the formation of a shoulder at lower binding energy. This shoulder was identified in earlier work as carbon atoms in a sp^3 configuration, i.e. the formation of a covalent bond to graphene[42,109]. These earlier studies described the formation of C-H bonds, but as the binding to CH_3-groups, is very similar we assign this peak to the formation of methyl functionalized graphene. Furthermore, a contribution of the CH_3-group at higher binding energies, similarly to h-BN is expected (B-CH_3: 285.0 eV, N-CH_3: 285.7 eV, or CH_3 on SiC: 284.9 eV), but cannot be resolved, due to the larger contribution of graphene. However, the shoulder at 284.4 eV is an indirect indication of covalent bonds formed during the adsorption Additionally, the entire spectrum shifts to a lower binding energy by 0.1 eV. We attribute this to the additional electron density, the adsorbed species provide, shielding the generated core hole, during the XP process. During heating with a linear heating ramp of 0.5 K/s we find that the shoulder at 284.4 eV stays constant up to 200 K. Subsequently, it slowly decreases, until 345 K, when it completely vanishes, and the signal of pristine graphene is restored. This is also supported by the quantitative analysis shown in Figure 8.5c. However, the quantification is challenging due to damping of adsorbed iodine, as well as the changes in the peak shape of graphene during annealing, as described in[50]. The quantitative analysis however, gives a lower limit with 0.18 ML of sp^3 carbon, which are obtained, when neglecting the damping of the signals. This amount also includes possible covalently bound iodine. During heating, the entire spectrum of graphene shifts back to its pristine position, further indicating that all adsorbed species have desorbed when reaching 550 K.

I 4d core level region:

Data recorded in the I 4d core level is shown in Figure 8.5b and the respective quantitative analysis in Figure 8.5d. In the I 4d core level region, we observe similar species, as for MeI on h-BN: Two spin orbit split main contributions, identified as I_3^- and I_5^-, located at 48.4 (50.1) and 49.2 (50.9) eV, respectively. An additional contribution is located at 49.7 eV (51 eV). Due to the very similar binding energy as the physisorbed MeI at h-BN, we believe that this is MeI, interacting with iodine on the surface. Upon heating, both poly-iodine species start to decrease from 200 K on. The decrease becomes faster at 270 K and the two polyiodine species have completely vanished at 360 K. They remain 40 K longer on the surface than on h-BN. The contribution for the species of bonded MeI stays constant from 150 to 200 K; subsequently the desorption of the polyiodines leads to an increase of intensity as damping is lifted. It starts to desorb beginning at 240 K and has desorbed and partially reacted at 290 K. The reaction product is found at 50.0 eV (51.7 eV), appearing at 290 K and remaining on the surface of the sample until 490 K. Due to this thermal stability, we assume that this is again a chemically bonded iodine species. However, the coverage never exceeds 0.01 ML.

Thus for graphene, we again observe polyiodine species, however, no bound iodine at 48.9 eV, as was observed for h-BN. Instead, we find an additional chemisorbed species at 49.7 eV and a slightly higher thermal stability of all the physisorbed species. We observe a chemisorbed species, which reacts at 290 K and desorbs until 490 K.

Graphene shows a similar total coverage for iodine and we were able to indirectly prove that graphene shows the formation of a covalently bonded CH_3 group. However, the thermal stability is again lower than on h-BN. Moreover, UPS did not show any new bands.

As a conclusion, the reaction pathway is shown in Figure 8.6 for both h-BN in Figure 8.6a and graphene in Figure 8.6b, on the basis of our TPXPS experiments. We find on both the h-BN/Ni(111), and graphene/Ni(111) distinguishable reaction steps, which are best described for h-BN as the step-wise dehydrogenation of the adsorbed CH_3-species, from “CH_3” to “CH” to “C” and a restoration of the pristine h-BN sheet. For graphene the reaction is depicted in Figure 8.6b. Here we only find desorption of the adsorbed species, with the exception of the formation of minor amounts of bonded iodine. If a dehydrogenation or other reaction occurs cannot be resolved in the C 1s core level, due to the large graphene contribution. Bonded iodine also desorbed before 500 K.

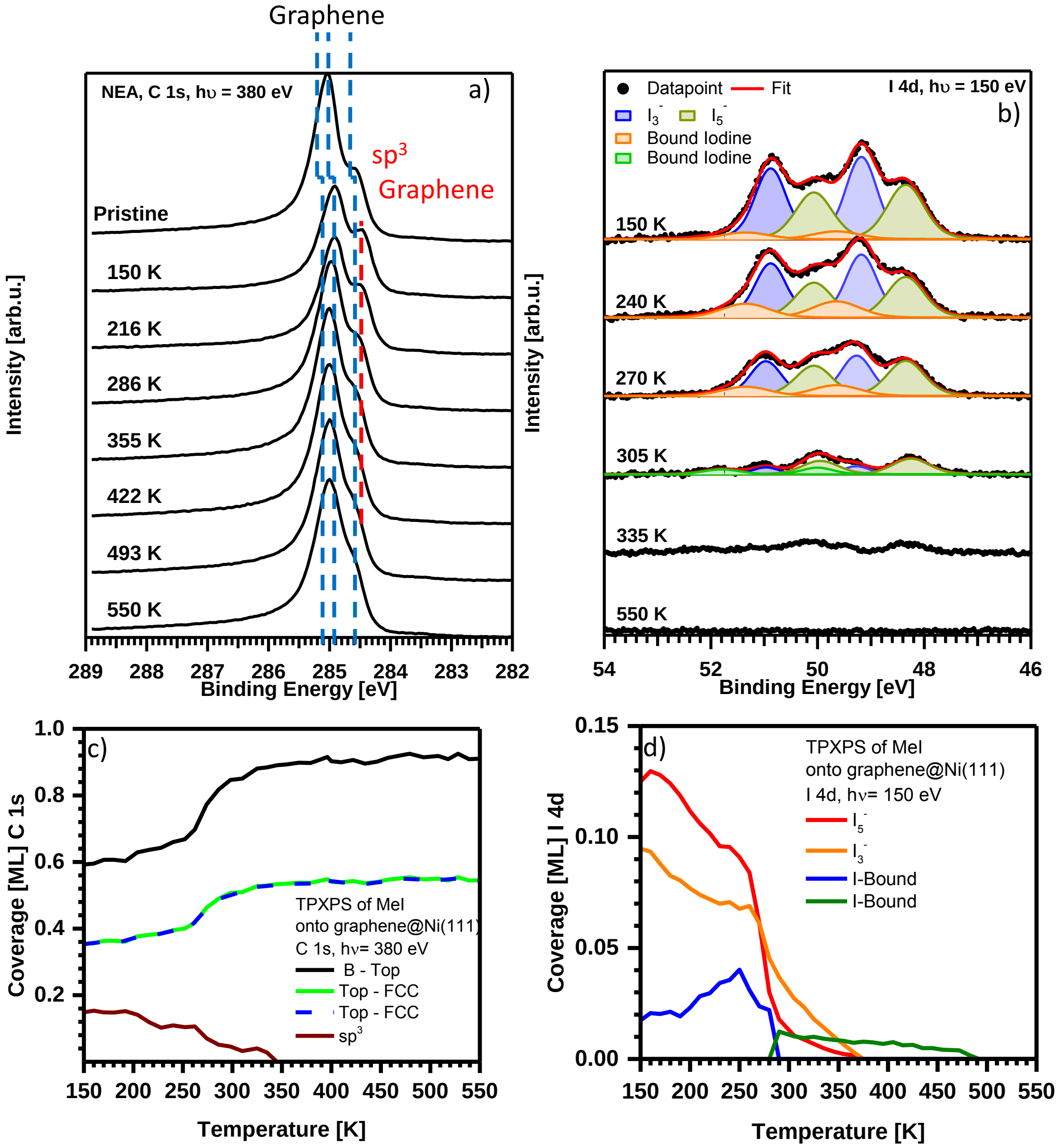

Figure 8.5: XPS data of the functionalization of graphene on Ni(111) and the corresponding TPXPS experiments. (a) 150 K: C 1s spectrum obtained after adsorption. Subsequent spectra obtained during TPXPS. The three contributions for graphene are marked. The contribution for sp^3 carbon in the graphene backbone is marked in red. (b) I 4d spectrum at 150 K obtained after adsorption. Subsequent spectra are recorded during TPXPS. (c) Quantitative analysis of the C 1s region. (d) Quantitative analysis of the I 4d region.

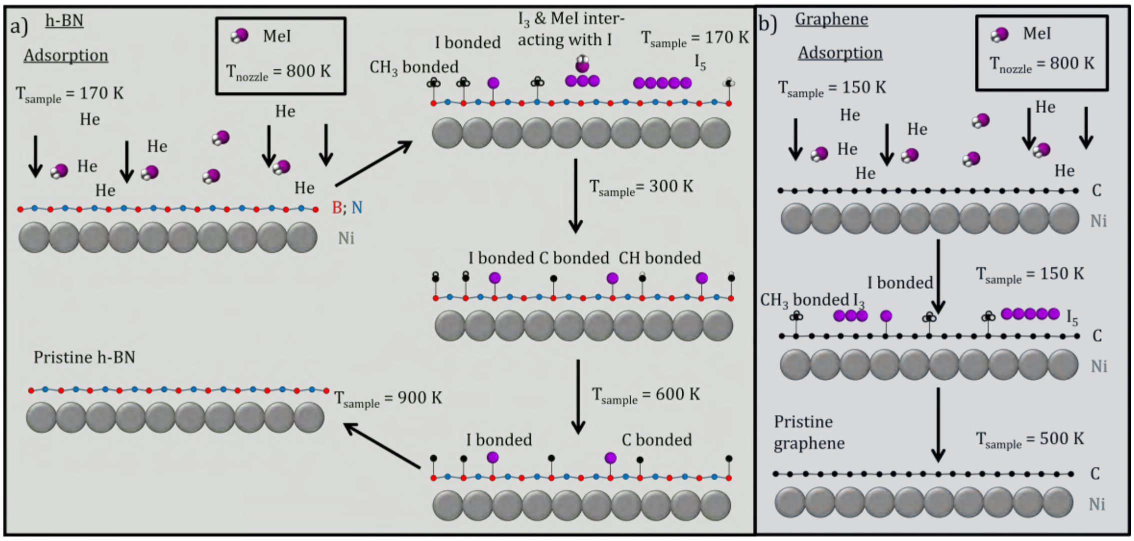

Figure 8.6: Reaction scheme: (a) reaction observed for h-BN. We use the characteristic intermediates observed in the C 1s core level to divide the reaction into steps: adsorption, mainly CH on the surface, C on the surface and restoration of pristine h-BN. (b): reaction observed for graphene: adsorption, CH_3 and iodine on the surface, and desorption of all physisorbed and chemisorbed species and restoration of pristine graphene.

8.3 Conclusion:

To conclude, we are able to adsorb methyl iodide (MeI) through a supersonic molecular beam seeded with helium, with a heated nozzle onto *hexagonal*-boron nitride and graphene. The adsorption takes place at a temperature, where molecular MeI does not stick to the surface. XPS reveals several species adsorbed on the surface. For h-BN, these are: CH_3, I_3^- I_5^-, MeI interacting with iodine. Furthermore, we are able to distinguish two different CH_3-species, namely bonded to boron or nitrogen in h-BN. Temperature programmed experiments reveal the thermal stability of the adsorbed species. We find that the B-CH_3 species is stable and reacts to B-CH and B-C, with the carbon dissolving into the Ni(111) bulk at 750 K. No other carbon-containing species was found to be stable. For the iodine species, we find that the poly iodines, and physisorbed MeI desorb at elevated temperatures. However, chemically bonded iodine is found on h-BN up to 850 K.

Graphene on Ni(111) shows a rather different reactivity: In the C 1s core level, we can only indirectly conclude that we find CH_3-groups bonded to graphene but we are able to observe sp^3-hybridized carbon atoms of graphene. However, it is not possible to observe any evidence of a reaction of possible adsorbed CH_3 groups. In addition, the stability of the adsorbed iodine groups differs. While the adsorbed polyiodines show a slightly higher thermal stability, only minor amounts of chemically bonded iodine groups are found. These are only stable up to 500 K.

The last chapter of the results of this thesis deals with the intercalation of graphene with argon. This leads to the formation of freestanding graphene over argon bubbles with a significant pressure. This can be understood as a functionalization of graphene, but not from the top side, but from the bottom side, although maybe different gases would lead to a stronger change in the band structure as the used argon.

9 Argon intercalation of graphene

The results in this chapter have already been published and the text has been adopted from this publication:

Keeping argon under a graphene lid - Argon intercalation between graphene and nickel(111), F. Späth, K. Gotterbarm, M. Amende, U. Bauer, C. Gleichweit, O. Höfert, H.-P. Steinrück, and C. Papp, *Surf. Sci.* 2016, *643*, 222–226[196].

Graphene on Ni(111) is an example of a strong interaction between the 2D material and the substrate. Thus intercalation of gases is difficult to achieve under high-vacuum conditions. Herein, the novel approach of pre-implanting gases in the substrate, which partly desorb during preparation of the 2D material, was chosen. For this purpose argon was sputtered into the Ni(111) surface, and subsequently graphene was grown on the argon containing substrate. During the preparation of graphene, argon diffuses from the Ni(111) bulk towards the surface and is captured by the graphene over-layer. The formation of argon blisters was indirectly observed with XPS, as two argon species were found. One argon species was attributed to argon only in contact with neighboring argon atoms, while the second species was attributed to argon in contact with Ni(111) and graphene. From this model, a size of the argon blisters was determined, as the intercalated graphene shows also a different binding energy in the C 1s region. From heating experiments, a higher thermal stability of graphene above argon was observed. Moreover, graphene shows very little interaction with the argon underneath, giving it a more quasi-free standing character.

9.1 Introduction

Graphene, the hexagonal 2D carbon allotrope with semi-metallic properties, has gained great attention over the last years, in particular in its free standing form[111,112,255–257]. It is proposed as a future substitute for silicon in semiconductor industries. Another potential application field is gas sensors, due to graphene's specific electronic structure that can easily be manipulated by adsorption. Here, changes for very low concentrations, in the ppb region and below were observed[21]. By covalent functionalization, e.g. the attachment of OH or H groups, the electronic structure and resistivity of graphene can significantly be altered, or even changed from semi-metallic to semi-conducting[247,258]. Besides its electronic structure, also the mechanical and chemical properties of graphene are of interest: The atomic structure of graphene that is, close packed six membered rings of carbon atoms, is proposed to be helium leak tight, and it was therefore suggested to be used as a gas barrier[28]. In this context, applications for gas containment, gas separation[117,259,260], or protective coatings are discussed[116, 209,261]. Gas separation with modified graphene membranes was proposed to allow helium separation from other gases, and helium isotope separation[26,27]. Porous two-layer graphene membranes with various pore sizes, prepared by focused ion beam etching and photo lithography, exhibit good separation ratios for CO_2 and H_2 for pore diameters below 10 nm. Furthermore, strong improvements in the permeance of water, water vapor and oxygen were achieved, as compared to current state-of-the-art membranes[262]. However, the preparation of well-defined pores for very high separation ratios is still challenging, as it requires manipulation of graphene on an atomic scale and sometimes special edge termination[117,263].

Several groups investigated the properties of graphene as membrane for gas containment, and for corrosion inhibition with various techniques; one example is a micro chamber etched into a SiO_2 substrate sealed with transferred graphene that was investigated with atomic force microscopy (AFM)[28]. A similar approach used graphene membranes that were transferred onto a patterned SiO_2 substrate[264], leading to graphene-sealed cavities. These structures show characteristic, switchable shapes, depending on the pressure difference within the cavity and applied external pressure. For graphene-sealed chambers, the leak rates are measured with mass spectrometry and weighing[265]. Furthermore, the use of graphene as corrosion-inhibiting material has been proposed and model systems of graphene protective coatings were studied by Raman spectroscopy, scanning tunneling microscopy (STM), scanning electron microscopy (SEM), or optical microscopy[266,267].

Despite these efforts, experiments regarding the properties of graphene in possible applications as membrane or as gas-containing material in a controlled surface science environment, i.e., under ultra-high vacuum conditions investigated with high resolution X-ray photoelectron spectroscopy (XPS), are still missing. Furthermore, up to now, researchers mostly used either graphene prepared with the scotch tape method[28], transferred graphene (which was grown on other substrates)[261], or graphene grown at high pressures in inert atmosphere[266]. Thus, the results obtained up to now may be influenced by defects, the limited size of the flakes, by regions exhibiting double- or multilayer graphene, and by contaminations from the transfer.

Herein, we report on the intercalation of argon under a graphene layer on Ni(111). Using a surface science approach allows for studying single layer graphene as a membrane for gas containment under UHV conditions over a wide temperature range. Well-defined conditions result in a very clean and single layer of graphene with a low density of defects[267]. Argon is implanted into the Ni(111) crystal before graphene growth. During the preparation of graphene at elevated temperatures, argon then diffuses to the surface and is caught under the graphene layer instead of desorbing to the vacuum. We further report an increased stability of graphene on top of the intercalated argon, as compared to graphene on Ni(111), as no interaction with the underlying chemically active nickel is possible. We further conclude from these results that the intercalated graphene has a quasi-free standing-like character.

9.2 Results and Discussion

Preparation of Argon under Graphene

The sample was prepared in the following way: It was sputtered at 170 K with argon with a kinetic energy of 1 keV for 30 minutes. During sputtering an ion current 3 µA was measured on the 1 cm diameter, round sample. The pressure of argon during sputtering was 2x10^{-6} mbar. After sputtering, the sample was annealed to 900 K. Upon reaching this temperature, preparation of graphene was started: We use a supersonic molecular beam of propylene that yields, with the chosen parameters, a pressure of ~2x10^{-6} mbar on the sample surface[108], while maintaining a low background pressure in the chamber. Growth of graphene and the accumulation of argon underneath graphene were examined by in-situ high resolution XPS.

In Figure 9.1a and 9.1b, we show C 1s and the Ar 2p spectra, respectively, recorded during preparation of graphene at 900 K. In the first 300 s, we find a strong increase of a C 1s peak at a binding energy of 285.0 eV, which is assigned to the formation of graphene on Ni(111)[50, 55,268]. The quantitative analysis in Figure 9.1c (blue symbols) shows saturation of the C 1s signal after ~300 s, at a coverage of 2.0 ± 0.1 ML, which corresponds to a closed layer of graphene with two carbon atoms per nickel surface unit cell. To avoid slow decomposition of the graphene layer at 900 K (which would occur under vacuum conditions at this temperature) and to keep a closed graphene layer during the accumulation of argon, we continuously supplied the precursor propylene at 2x10^{-6} mbar. After each C 1s spectrum, we recorded Ar 2p spectra that are shown in Figure 9.1b. During graphene growth, we observe the formation of two spin-orbit-split doublets in the Ar 2p region. The first Ar $2p_{3/2}$ and $2p_{1/2}$ doublet is located at 241.8 and 243.9 eV, respectively and the second at 242.3 and 244.5 eV. The spin-orbit splitting of the two doublets is similar, considering the error bars of ± 0.05 eV of the denoted binding energies. In the following we will only discuss the larger Ar $2p_{3/2}$ contribution. After 5400 s we find a saturation of the Ar 2p signals. The quantitative analysis of the argon spectra, recorded during the growth of graphene, is shown in Figure 9.1c as red and black symbols. We like to add here that at this stage of the experiment, it is not possible to observe any notable differences in the C 1s signal in comparison to the graphene/Ni(111) system due to the small contribution of graphene intercalated by Ar.

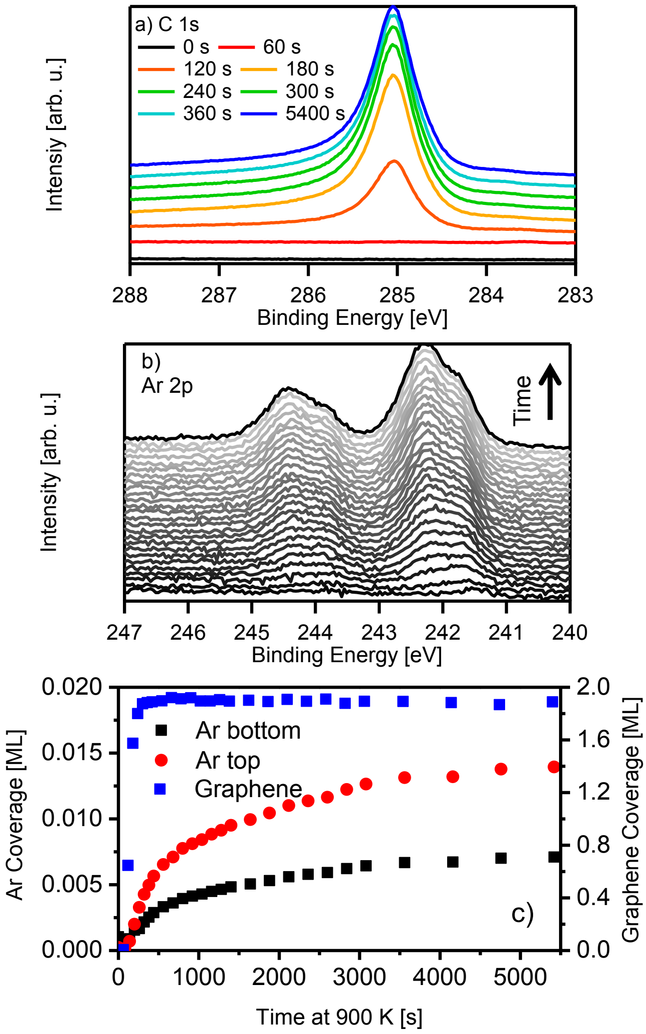

Figure 9.1: Preparation of graphene and accumulation of Ar at the graphene/Ni(111) interface. (a) Selected C 1s spectra, collected during graphene growth (graphene is saturated after 360 s); the last spectrum is recorded after 5400 s. (b) Waterfall plot of the Ar 2p spectra recorded as a function of time; hv = 380 eV. (c) Quantitative analysis of the spectra in (a) and (b) after peak fitting: left axis Ar coverage, right axis carbon coverage. Damping of the signal from Ar by the graphene layer and self-dampening of Ar were not taken into account.

The two argon species show a different growth behavior: below 200 s, the species at 241.8 eV denoted as $\mathrm{Ar}^{\mathrm{bottom}}$ dominates during graphene growth (140 s: $\Theta_{\mathrm{Ar}}{}^{\mathrm{top}}=7*10^{-4}$ ML vs. $\Theta_{\mathrm{Ar}}{}^{\mathrm{bottom}}=9*10^{-4}$ ML); the second Ar species at 242.3 eV, $\mathrm{Ar}^{\mathrm{top}}$, is the dominant contribution from 200 seconds on (200 s: $\Theta_{\mathrm{Ar}}{}^{\mathrm{top}}= 2.0*10^{-3}$ ML vs. $\Theta_{\mathrm{Ar}}{}^{\mathrm{bottom}}=1.5*10^{-3}$ ML), until the end of the experiment; see Figure 9.1b and 9.1c. During the experiment, we observe a binding energy shift for the both Ar species towards higher binding energies by 0.2 to 0.3 eV. As evident from Figure 9.1b, first Ar^{bottom} is populated and subsequently Ar^{top} increases. Within the accuracy of our experiment, the growth behavior of graphene was not influenced by Ar, as it accumulates under graphene only after a part of the graphene layer has formed. In a similar experiment, we only implanted argon into a clean Ni(111) crystal that is, without a graphene layer on top. This experiment shows that at 900 K no argon is detectable in the near surface region (see Figure 9.2), with a detection limit of ~ $1x10^{-4}$ ML. This is in line with argon TPD spectra, which show that argon desorption from the surface-near region is completed at this temperature, when Ar is implanted with 1 keV kinetic energy[269].

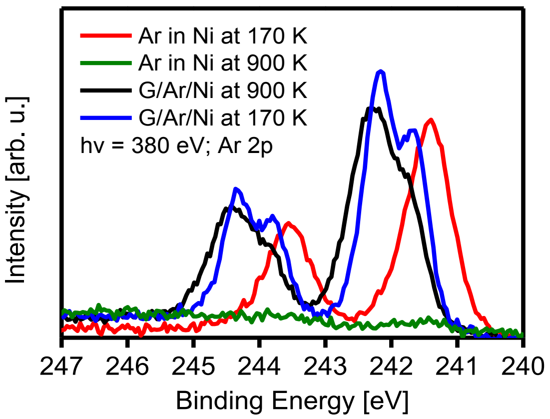

Figure 9.2: Ar 2p XP spectra of Ar in nickel and Ar under graphene. Red spectrum: Ar in Nickel after Ar sputtering of clean surface at 170 K; green spectrum: after Ar sputtering of the clean surface at 900 K; black spectrum: Ar under graphene after a total annealing time of 5400 s at 900 K (last spectrum of Figure 9.1b; blue spectrum: after Ar intercalation at 900 K, measured at 170 K.

Figure 9.2 shows Ar 2p spectra after implanting Ar into a clean Ni(111) surface at 170 K (red) and 900 K (green); for comparison, also spectra of the preparation of argon under graphene at 900 K (black) and at 170 K (blue) are depicted. The latter show clear chemical shifts of 0.4 and 1.0 eV towards higher binding energies with respect to argon in clean Ni(111), clearly demonstrating that the two intercalated argon species are in a very different local environment than Ar implanted in Ni(111).

During the initial formation of the graphene layer at 900 K, no intensity is observed in the first Ar 2p spectrum (after approx. 80 seconds), which indicates that Ar diffuses to the partly uncovered surface at this elevated temperature and immediately desorbs; therefore, the amount of Ar within the information depth of XPS is below the detection limit of ~ $1\text{x}10^{-4}$ ML. The information depth (ID) is defined as 3 times the inelastic mean free path for Ar 2p photoelectrons in nickel, and is estimated to ~3 nickel layers at a kinetic energy of approx. 140 eV[90]. We thus conclude that the implanted Ar, which diffused to the surface at later stages of the experiment, must be dissolved deeper in the nickel crystal, beyond the XPS information depth. This is in agreement with TPD results for similar implantation energies, where minor diffusion-limited desorption from deep lying argon is found at 900 K[269]. Interestingly, upon heating a clean Ni(111) sample sputtered at 170 K (Figure 9.2, red spectrum), we observed only one Ar 2p contribution, until it vanishes at 900 K (green spectrum). From this observation, we rule out the formation of sub-surface argon bubbles or argon filled cavities, as described for other materials such as ruthenium[270,271], aluminum or silicon[272,273], where two Ar contributions are found in XPS.

Thermal stability of argon under graphene

To investigate the stability of argon under graphene, we carried out XPS measurements while heating the sample from 170 K (after cooling down from the preparation temperature of 900 K) to 1100 K. In Figure 9.3a we show selected spectra of a heating experiment in the Ar 2p region, and the corresponding quantitative analysis is depicted in Figure 9.3c. In Figure 9.3b, we show the corresponding C 1s spectra of the same experiment, and in d an enlargement of the C 1s spectrum taken at 1050 K is displayed. During heating to 1000 K, we find a constant total argon coverage, indicating that graphene acts as a leak tight gas barrier up to this temperature. Interestingly, however, the relative abundance of the two argon species changes, which might be due to ripening of the Ar agglomerates, as will be discussed below. At the same time, up to 900 K, only a small loss in carbon intensity is observed. Thereafter, the carbon signal steeply decreases, indicating the dissolution of carbon into the bulk of the Ni(111) crystal.

Above 950 K, simultaneously to the onset of the decomposition of the graphene sheet (see Figure 9.3b and 9.3c), a considerable and abrupt shift of 0.45 ± 0.05 eV and 0.43 ± 0.05 eV towards higher binding energy is observed for Ar^{top} and Ar^{bottom} species, respectively. The C 1s spectra in Figure 9.3b show that at 1050 K the carbon peaks have more or less disappeared and only a small peak at 284.5 ± 0.1 eV remains; see the enlarged spectrum in Figure 9.3d. Interestingly, the C 1s signal is lowered to only ~2.5% of the original intensity, while the Ar 2p intensity is still ~72%.

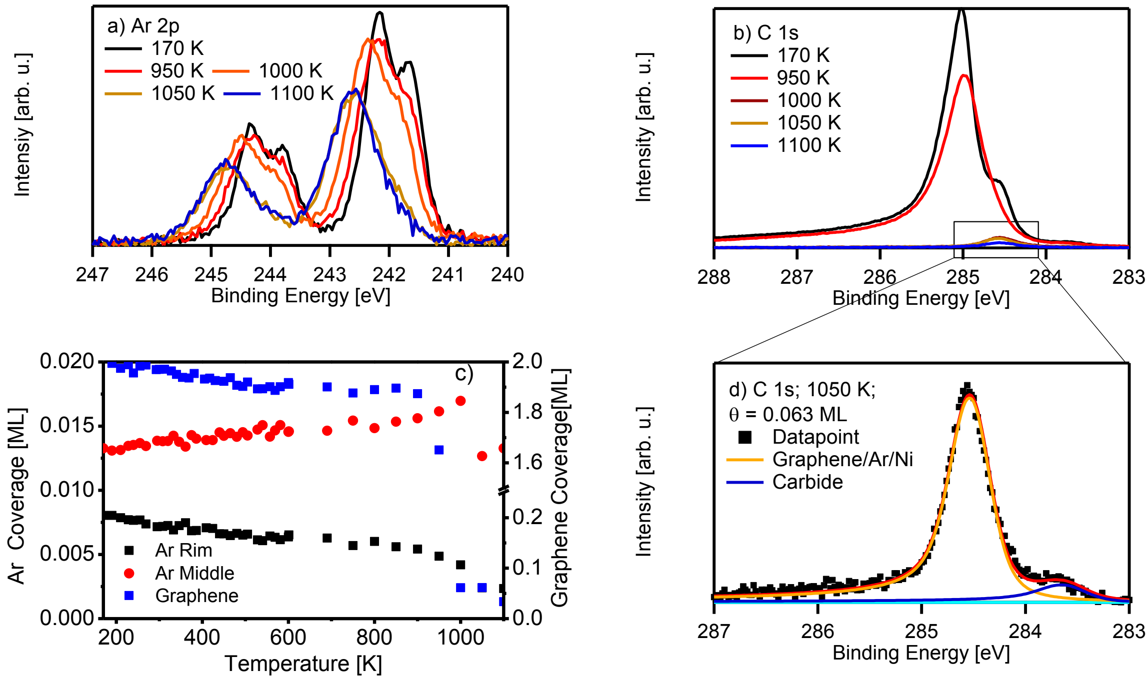

Figure 9.3: Heating of graphene to 1100 K: (a) Selected Ar 2p spectra. (c) Quantitative analysis of the heating experiment. Axis on the left for argon, on the right for graphene. (d) Deconvolution of the C 1s spectra of graphene recorded at 1100 K and shown in comparison to the spectrum recorded at 170 K (b).

From Figure 9.3b and 9.3d, we conclude that in the graphene spectra at 170 K (black) and 950 K (red, Θ_C= 1.7 ML), the C 1s signal at 284.6 eV contain two contributions, one from the graphene carbon in an top-fcc geometry[50] and one from graphene above argon (G/Ar). This latter contribution is the small peak left after heating the sample to above 1000 K (see Figure 9.3d), which due to its low intensity can only be discerned at high temperatures, when the other contributions have disappeared due to dissolution of the rest of the graphene sheet into the nickel bulk. This C 1s signal at 284.5 ±0.1 eV is further denoted as G/Ar and is ascribed to graphene above argon, or as argon-intercalated graphene. The binding energy of G/Ar is very close to that of quasi-free-standing graphene (284.30 eV), as obtained e.g. by gold intercalation on Ni(111)[122]. The quasi free-standing-like character is attributed to the inert character of the noble gas argon, as compared to the Ni(111) substrate.

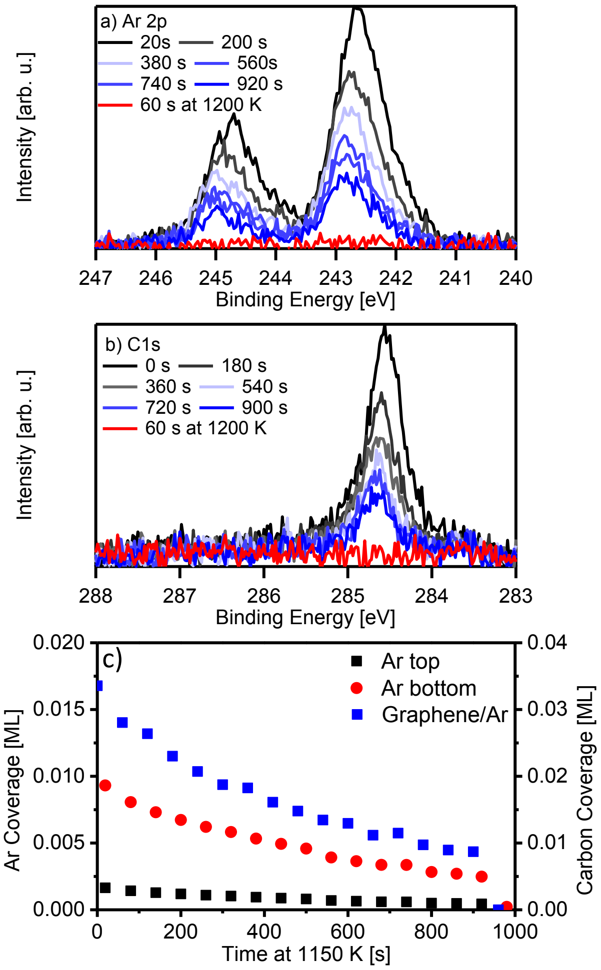

Figure 9.4: Isothermal decomposition of Ar underneath graphene at 1150 K. (a) and (b) selected Ar 2p and C 1s spectra, respectively, recorded as a function of time. (c) Quantitative analysis of the data in (a) and (b); note that the last data point was obtained after flashing the sample to 1200 K for 60 s. hv = 380 eV.

When the temperature is further increased to 1150 K, the intercalated Ar species and the G/Ar species are found to decrease exponentially with time, as seen in Figure 9.4. The ratios of Ar^{top} to Ar^{bottom}, and of carbon to the two argon species stay constant during this period. After 900 s, the sample was heated to 1200 K for 60 seconds, which led to the complete disappearance of all signals in the Ar 2p and C 1s core level regions, as seen in the red spectra in Figure 9.4a andb, and also in the quantitative analysis in Figure 9.4c (last data point at ~950 s). This behavior shows that those regions of graphene that are stable at 1150 K, are responsible for the containment of argon. Vice versa, it also shows that non-intercalated graphene on Ni(111) is less stable than argon-intercalated graphene. This is attributed to the catalytic properties of the nickel surface that are needed to break up and successively dissolve the graphene sheet, as compared to the situation on top of the intercalated chemically inert argon. Thus, in regions, which are not intercalated by Ar, graphene becomes instable above 900 K and diffuses into the bulk of the Ni(111) crystal, while the other carbon atoms which are not bound to nickel exhibit a higher thermal stability. It is important to note that some of the carbon atoms of the graphene sheet, which cover the intercalated argon regions, must be still bound to the Ni(111) surface, to keep the graphene “lid” closed[267]. We like to stress here that the decoupling of the graphene sheet from the Ni is also the reason for the stability of these hemispheres: argon keeps graphene from dissolving completely into the nickel bulk, while graphene keeps argon from desorbing into the vacuum. Thus, the two components of these hemispheres stabilize each other, making a thermodynamically very unstable system possible.

Our findings are in line with results from Mu et al., who found CO intercalated between graphene and Pt(111) to desorb at higher temperature than from the bare Pt(111)[187]. Also, a higher desorption temperature was found for water under graphene on mica[274]. Other examples are OH/H_2O filled graphene nano bubbles on diamond (100)[275] and O_2-filled graphene nano bubbles on Ru(001)[276]. Interestingly, hexagonal boron nitride (h-BN) on Rh(111) intercalated with Ar shows quite different results: Ar was found at weakly interacting regions of the Moiré pattern and XPS shows only one Ar species. Moreover, a lower thermal stability for the Ar-intercalated parts of the h-BN sheet was observed[277].

9.3 Model of Argon under Graphene

Next, we want to discuss a model for the origin of the two argon species found in the experiment and that allows us to obtain a rough estimate of the pressure in the three dimensional argon structures. For a single argon atom, which represents the beginning of the growth of all possible argon ensembles under graphene, we expect only one peak in the Ar 2p core level region. This is the contribution found during the beginning of the growth of graphene. We thus assign the Ar^{bottom} peak to such single argon atoms between graphene and the Ni surface, and also to two-dimensional ensembles of argon atoms that exist at the argon/nickel interface. Ar^{bottom} atoms have a stronger interaction with the surface (are better screened) than Ar^{top} atoms that are in contact with graphene or with argon, leading to peaks at lower binding energies. Our assignment, in terms of binding energy shifts, is in line with work by Trischberger et al.[278] for xenon on a hydrogen-terminated Pt(110) surface and by Weinelt for xenon in Pt trenches[279].

One possible arrangement would be a graphene hemisphere filled with Ar atoms, with Ar^{bottom} atoms at the nickel interface and the Ar^{top} atoms filling the rest of the hemisphere. This certainly is a strong simplification and results in a structure with a very high aspect ratio (width to height (w/h) of 2). While such heights are typically not reported for graphene bubbles on Pt (w/h ~3) and Ru (w/h ~20), the model nevertheless allows us to obtain some insight. When modeling such a hemisphere we consider the experimental ratios of Ar^{bottom} : Ar^{top} : graphene of 1 : 5.3 : 26 that we find at 1050 K in Figure 9.3c, where we can quantify the amount of graphene above the argon atoms. If Ar is statistically distributed, this leads to a graphene hemisphere that has a bottom to volume ratio of 1 : 6.3 (1+5.3, as the volume is given by the Ar^{bottom} + Ar^{top}). Since for a hemisphere, the volume (amount of Ar^{top}+ Ar^{bottom}) grows as $2/3r^3\pi$, while the interface area to the substrate (amount of Ar^{bottom}) grows as $r^2\pi$, this yields a unique ratio for its size; for this ratio of 1: 6.3 one obtains 21.000 carbon atoms, enclosing a volume of ~1775 nm^3. From the above ratio, we then calculate ~800 Ar atoms at the nickel interface and ~4300 Ar atoms in the rest of the hemisphere. When applying the ideal gas law, the total number of ~5100 Ar atoms in this hemisphere results a pressure of 417 bar at

1050 K. This value has to be considered as a rough estimate of the pressure of argon under graphene in view of the applied assumptions and from the fact that argon at such temperatures (1050 K) and pressures is supercritical. In comparison, for graphene layers on SiO_2 a pressure of 7 bar was deduced by Boddeti et al.[264]. Lim et al. found a pressure, using a similar calculation as applied herein, of 10,000 bar for OH/H_2O-filled graphene nano bubbles on Diamond (100)[275].

When discussing the application of graphene as a gas barrier, the influence of defects has to be discussed: defects might allow diffusion of argon through the graphene layer into vacuum. Jacobson et al. have shown that for graphene prepared on Ni(111) at 925 K - close to our 900 K preparation temperature - only Stone Wells defects (alternating 7- and 5-membered rings) and rarely single carbon vacancies are observed[267]. Considering the van der Waals diameter of a single argon atom (376 pm) and the lattice constant of graphene on Ni(111) (246 pm), it seems unlikely that argon can diffuse through such defects in the graphene lattice. Even defects of up to 6 carbon atoms seem sufficient to avoid diffusion through the graphene layer for molecules with about a similar size as argon[22,280]. While the graphene sheet is still bond to the nickel surface, carbon atoms at vacancies are proposed to bind particularly strong to the substrate, and thus prevent argon from desorbing through such vacancies[267].

Finally, we address the change of the relative concentration of Ar^{bottom} and Ar^{top} upon heating (Figure 9.3c), at a constant total Ar coverage. We attribute this finding at a ripening of the argon agglomerates under graphene for temperatures below 1000 K, when graphene is still stable. Within our model, the relative increase of the Ar^{top} species indicates a change towards larger bubbles, which might be due to Ostwald ripening. At temperatures above 1000 K, when graphene is no longer stable, we find a different behavior: the total Ar coverage significantly drops, by ~22% for the Ar^{top} species and about 51% for the Ar^{bottom} species. The stronger decrease of the latter indicates a lower stability of smaller bubbles.

9.4 Conclusions

In conclusion, we presented the intercalation of graphene with argon via the novel approach of pre-implanting the intercalated species in the substrate on which graphene is grown, namely Ni(111). We can differentiate between argon atoms within the inner part of the formed bubbles and in contact with graphene, and those argon atoms in contact with the Ni(111) substrate; the latter show a lower binding Ar 2p binding energy. The intercalation of argon leads to a decoupling of graphene from the nickel surface, as deduced from the binding energy and the thermal stability of the graphene sheet. We find a ripening of the argon agglomerates under graphene up to temperatures of 1000 K, and a different growth mechanism at temperatures above. For the bubbles formed at 1050 K, we estimated the pressure in the bubble by assuming a hemispherical shape.

10 Conclusion

The 2D materials graphene and h-BN are promising materials for many future applications. Graphene shows ballistic electron transport, while the isostructural and isoelectronic h-BN has a bandgap of 5.4 eV. Graphene may further be used as a gas separating membrane, while h-BN may be a universal coating for the prevention of oxidation. However, suitable ways to tailor the electronic structure as well as the chemical properties, either through intercalation or chemical functionalization are still scarce in literature.

In the first part of this thesis, it was shown that nitrogen doped graphene readily reacts with atomic hydrogen. Here it was observed that both species of nitrogen in graphene, namely pyridinic and graphitic (substitutional) nitrogen, bind to hydrogen. Moreover, it was shown that the reaction of the carbon back-bone of graphene is completely unaffected by doping. For pyridinic nitrogen, it was shown that, although this nitrogen is only in a twofold bonding configuration, the dehydrogenation temperatures are very similar to carbon in graphene, indicating a similar desorption mechanism. For graphitic nitrogen, only one desorption maximum was observed, at a similar temperature as the first desorption maxima of pyridinic nitrogen. Thus, although the three-fold bonding of this nitrogen is similar to carbon in graphene, a different dehydrogenation mechanism is likely.

As hydrogenation was found to be a promising route for bandgap manipulation, and the hydrogenation of graphene and nitrogen doped graphene on Ni(111) is well understood, the reactivity of h-BN towards atomic hydrogen was investigated. TPD experiments revealed similar desorption temperatures of hydrogen, as in the case of graphene, with also two desorption maxima. By NEXAFS experiments, it was deduced that the desorption maxima at 570 K stems from hydrogen bonded to the basal plane of h-BN. From DFT calculations, it was determined that bonded hydrogen is a meta-stable state. When increasing the atomic hydrogen exposure, a desorption maximum at 300 K was populated. NEXAFS measurements showed that the h-BN-Ni(111) interaction is minimized upon populating this adsorption state. Thus, hydrogen intercalates between h-BN and the Ni(111) crystal. Also from DFT calculations, this was confirmed to be the thermodynamically most stable configuration. This chapter showed that h-BN has a distinctively different reactivity towards atomic hydrogen that is strongly exposure-dependent. This is in contrast to graphene on Ni(111). Moreover, it was shown that quasi freestanding h-BN could be prepared for the first time via hydrogen intercalation on Ni(111).

In a further step to investigate the interaction of h-BN with ambient gases, the activated molecular adsorption of oxygen achieved by exposing h-BN to oxygen from the supersonic molecular beam was studied. A considerable effect of the substrate temperature was found. When adsorbing oxygen at a substrate temperature of 290 K, a single oxygen species is observed in XPS. From NEXAFS, we find a slight increase in h-BN substrate interaction and a strong angular anisotropy, thus indicating oxygen bonding to h-BN, with the oxygen-oxygen intact. DFT reveals that oxygen binds side on with bonds to two boron atoms from the surface.

In the following chapter, the adsorption of molecular oxygen was further investigated with the aim to study the strong dependence on the substrate temperature of the reaction pathway. At 440 K, we observe the formation of two additional oxygen species in XPS, while the species observed at 290 K is only present in the beginning of the experiment. The two additional species are attributed to oxygen intercalating h-BN and oxygen oxidizing h-BN. This conclusion is further confirmed by NEXAFS measurements. Oxygen adsorption at 600 K results in the oxidation of h-BN. Here, several distinct oxygen bonding motives from BO to BO_3 are observed. Annealing results in oxygen desorption, deintercalation and formation of B_2O_3, for an adsorption temperature of 290, 440 and 600 K, respectively. For 290 and 440 K, also oxidation of h-BN upon annealing is observed as a minor reaction pathway.

To further understand the reactivity of the h-BN Ni(111) system, both oxygen and hydrogen were co-adsorbed. When oxygen is pre-adsorbed on h-BN and atomic hydrogen is subsequently adsorbed, the loss of oxygen is observed. During hydrogen exposure, h-

BN is never pristine, as hydrogen already co-adsorbs with oxygen. After the complete desorption of oxygen, hydrogenated h-BN is found. For the hydrogen pre-covered h-BN, it is observed that oxygen adsorption is substantially hindered and thus much slower. However, during the experiment, desorption of 50% of the adsorbed hydrogen was found, and an oxygen coverage of ~ 50% of the maximum coverage observed for pristine h-BN. TPXPS experiments reveal that no interaction that would influence the desorption temperature of oxygen is observed when the sample is loaded with oxygen and hydrogen. A second experiment shows that the hydrogen-displacing oxygen is bonded to h-BN and not intercalated.

The methods used to functionalize h-BN with oxygen indicate that 2D materials are rather unreactive and harsh conditions have to be applied, to achieve functionalization. With the aim to functionalize the system with organic molecules, the exposure to high energetic methyl iodide was studied. For both graphene and h-BN a reaction was observed. During the adsorption, a complex metastable state, with multilayer of methyl iodine, can shortly be populated, as long as the SSMB is operated; subsequently, upon adsorption following species were found for h-BN: the formation of B-CH_3 and N-CH_3 groups upon exposure, as well as multilayers were observed. Moreover, the formation of poly-iodine is found, which is also observed for graphene. Upon heating, a reaction from B-CH_3 to B-CH to B-C is observed, while all other carbon-containing fragments desorb. Iodine, which formed upon adsorption poly-iodine due to the confinement on the surface, decomposes upon heating to iodine and desorbs, while minor amounts intercalate. For graphene only the presence of sp^3 bonds is observed, as an indirect indication for functionalization.

Besides the functionalization of graphene on the vacuum side a further ansatz is to tune the system by intercalation. But as graphene on Ni(111) is an example of a very strong interaction of the 2D material with its substrate, the intercalation of gases is difficult and usually only achieved through pressures exceeding pressures that are UHV compatible. The novel intercalation method to pre-implant argon, with a sputter gun, into the Ni(111) bulk, was applied in here, for the first time. Upon preparation of graphene, the argon diffuses from the bulk to the surface and accumulates underneath graphene, giving it a quasi-free-standing character. In a temperature programmed XPS experiment, we observed ripening of the argon clusters, and that portions of graphene on top of argon structures are more temperature persistent. In an isothermal experiment, the dissolution of these structures was observed. As two distinctively different argon species were identified, namely, argon inside the argon bubble and in contact to graphene and Ni(111). Furthermore, the geometry of the argon bubbles was determined. From further simple calculations, a pressure inside the bubble of roughly 400 bar was determined, showing the immense tensile strength of graphene and the graphene Ni(111) interaction.

11 Zusammenfassung

Die beiden 2D Materialien Graphen und h-BN sind vielversprechend für viele zukünftige Anwendungen. Graphen zeigt ballistischen Elektronentransport und das isoelektronische und isostrukturelle h-BN hat eine Bandlücke von 5,4 eV. Graphen könnte weiterhin als Membran zur Gastrennung eingesetzt werden, und h-BN als universaler Schutz vor Oxidation. Jedoch sind passende Wege um ihre elektronischen und chemischen Eigenschaften maßzuschneidern bisher kaum in der Literatur zu finden.

Im ersten Teil dieser Arbeit wurde gezeigt, dass Stickstoff dotiertes Graphen leicht mit atomarem Wasserstoff reagiert. Es wurde festgestellt, dass beide Typen von Stickstoffen, der graphitische (substituierende) und pyridinische Stickstoff, Wasserstoff binden. Des Weiteren konnte gezeigt werden, dass Dotierung die Reaktivität des Kohlenstoffgerüsts nicht beeinflusst. Pyridinischer Stickstoff zeigt eine sehr ähnliche Dehydrierungstemperatur wie der Kohlenstoff in undotiertem Graphen, obwohl er nur zweifach an das Kohlenstoffgerüst gebunden ist. Dies weist auf einen ähnlichen Desorptionsmechanismus hin. Für graphitischen Stickstoff wurde nur ein Desorptionsmaximum gefunden. Dies ist beachtlich, da graphitischer Stickstoff auch dreifach koordiniert ist, genauso wie der Kohlenstoff in Graphen. Deshalb zeigt er wahrscheinlich einen anderen Dehydrierungsmechanismus.

Die Hydrierung ist ein vielversprechender Weg, um die Bandstruktur zu manipulieren. Diese Reaktion ist bei Graphen und Stickstoff-dotiertem Graphen adsorbiert auf Ni(111) bereits gut verstanden. Nun wurde auch die Reaktion von h-BN mit atomarem Wasserstoff auf Ni(111) untersucht. TPD Experimente zeigen zwei Desorptionsmaxima, bei ähnlichen Temperaturen wie für Graphen. Durch NEXAFS Experimente konnte gezeigt werden, dass das Desorptionsmaximum bei 570 K durch Wasserstoff, der an h-BN gebunden ist, verursacht wird. DFT Rechnungen zeigten, dass dies ein metastabiles Minimum ist. Sobald mehr atomarer Wasserstoff angeboten wird, wird der Zustand des Desorptionsmaximums bei 300 K besetzt. NEXAFS Experimente zeigen, dass wenn dieser besetzt wird, die h-BN - Ni(111) Wechselwirkung minimiert wird. Deshalb wird auf Wasserstoffinterkalation rückgeschlossen. Auch DFT Rechnungen zeigen, dass dies die stabilste Form des Adsorptionssystems ist. Somit wurde gezeigt, dass h-BN anders reagiert als Graphen und es wurde erstmals auf Ni(111) freistehendes h-BN mittels Wasserstoffinterkalation hergestellt.

Um die Wechselwirkung von h-BN mit Umgebungsgasen besser zu verstehen, wurde die aktivierte Sauerstoffadsorption untersucht. Dazu wurde Sauerstoff mittels eines Überschallmolekularstrahls auf h-BN adsorbiert. Es wurde festgestellt, dass die Substrattemperatur einen starken Einfluss auf das Adsorptionsverhalten hat: Bei 290 K wird mittels XPS eine einzige Sauerstoffspezies beobachtet. Durch NEXAFS konnte eine erhöhte Wechselwirkung von h-BN mit dem Substrat festgestellt werden, was auf eine Sauerstoff-h-BN Bindung deutet. DFT Rechnungen zeigten, dass die Bindung seitlich erfolgt, mittels je einer Bindung von einem Sauerstoffatom zu einem Bor. Im darauffolgenden Kapitel wurde die Adsorption von Sauerstoff weiter untersucht, mit dem Ziel den starken Einfluss der Substrattemperatur besser zu verstehen. Bei einer Substrattemperatur von 440 K beobachtet man in den XP Spektren zwei weitere Sauerstoffspezies, wohingegen die Spezies, welche bei 290 K gefunden wurde, nur zu Beginn des Experiments beobachtet wurde. Die zwei weiteren Spezies werden als interkalierter Sauerstoff und als h-BN Oxid identifiziert. Diese Schlussfolgerungen werden durch NEXAFS Messungen gestützt. Sauerstoff Adsorption bei einer Substrattemperatur von 600 K führt zu einer Oxidation des h-BN, mit mehreren verschiedenen Sauerstoffspezies, welche unter den allgemeinen Strukturen BO bis BO_3 zusammengefasst werden können. Das Heizen der Probe führt zu einer Desorption, Deinterkalation und der Bildung von B_2O_3, für Adsorptionstemperaturen von 290, 440 und 600 K, respektive. Bei 290 und 440 K wird zusätzlich, als Nebenreaktion, die Oxidation von h-BN beim Heizen beobachtet.

Um die Reaktivität von h-BN besser zu verstehen, wurden Wasserstoff und Sauerstoff ko-adsorbiert. Dazu wurde zuerst Sauerstoff adsorbiert und daraufhin atomarer Wasserstoff dosiert. Dadurch wurde die Desorption von Sauerstoff beobachtet. Es wurde des Weitern festgestellt, dass während der Desorption von Sauerstoff h-BN nie unfunktionalisiert vorliegt, da der Wasserstoff ebenfalls an die Oberfläche bindet. Sobald aller Sauerstoff desorbiert ist, liegt hydriertes h-BN vor. Wird Wasserstoff zuerst adsorbiert, wurde festgestellt, dass die Sauerstoffadsorption signifikant gehindert und verlangsamt ist. Im Verlauf des Experiments konnte jedoch noch ca. 50% der maximalen Sauerstoffmenge adsorbiert werden. Ein TPXPS Experiment zeigte, dass es zu keiner Interaktion zwischen Wasserstoff und Sauerstoff kommt, welche die Desorptionstemperatur des Sauerstoffs beeinflussen würde.

Wegen der geringen Reaktivität von 2D Materialien müssen harsche Bedingungen für eine Funktionalisierung gegeben sein. Ein Ziel ist es 2D Materialen mit organischen Molekülen im Ultrahochvakuum zu funktionalisieren. Der Beschuss mit hoch energetischem Iodmethan führt zu einer Reaktion sowohl mit h-BN als auch mit Graphen. Währen der Adsorption bildet sich eine meta-stabile Multilage von Iodmethan, solange der Überschallmolekularstrahl in Betrieb ist, aus. Des Weiteren werden auf h-BN folgende kohlenstoffhaltige Spezies beobachtet: B-CH$_3$, N-CH$_3$ und eine MeI Multilage. Auch wurden verschiedene Polyiod Spezies auf h-BN und Graphen gefunden. Durch Heizen kann eine Reaktion von B-CH$_3$ zu B-CH, zu B-C auf h-BN beobachtet werden. Andere Kohlenstoffhaltige Iodmethan Fragmente desorbieren. Iod, welches durch die Beengung auf der Oberfläche zu Polyiod reagierte zerfällt beim Heizen wieder zu Iod und desorbiert. Ein kleiner Teil interkaliert. Für Graphen kann die Funktionalisierung nur indirekt beobachtet werden, durch die Entstehung einer Schulter in den XP Spektren, welche auf sp^3 Kohlenstoff hinweist.

Das Graphen - Ni(111) Adsorptionssystem ist ein Beispiel für ein 2D Material, welches sehr stark mit seinem Substrat wechselwirkt. Deshalb ist es äußerst schwierig, unter UHV-Bedingungen Gase zu interkalieren. Um trotzdem quasi-freistehendes Graphen zu erhalten wird im Normalfall Gold interkaliert. In dieser Arbeit wurde der neue Ansatz, Argon vor dem Wachsen von Graphen, mittels einer Suptterionenquelle in das Substrat zu implantieren, angewendet. Während der Präparation von Graphen diffundiert das implantierte Argon aus dem Ni(111)-Bulk an die Oberfläche und bleibt unter Graphen. In einem temperaturprogrammierten Experiment wurden dann die Reifung der Argonansammlungen und eine erhöhte thermische Stabilität des Graphen, welches die Argonansammlungen zurückhält, beobachtet. In einem isothermen Experiment konnte die langsame Zerstörung der Argonansammlungen beobachtet werden. Es wurden zwei Argonspezies gefunden: eine in Kontakt mit Ni(111) und Graphen und eine nur in Kontakt mit anderen Argonatomen. Da des Weiteren die Menge an Kohlenstoffatomen, welche das Argon am desorbieren hindern gemessen werden konnte, wurde eine durchschnittliche Größe der Argonansammlungen und ein Druck darin berechnet. Dieser beträgt ungefähr 400 bar. Somit lässt sich zeigen wie extrem widerstandfähig Graphen ist.

12 Literature

[1] S. Bae, H. Kim, Y. Lee, X. Xu, J.-S. Park, Y. Zheng, J. Balakrishnan, T. Lei, H. Ri Kim, Y. Il Song, Y.-J. Kim, K. S. Kim, B. Özyilmaz, J.-H. Ahn, B. H. Hong, S. Iijima, *Nat. Nanotechnol.* 2010, *5*, 574–578.

[2] T.-H. Han, Y. Lee, M.-R. Choi, S.-H. Woo, S.-H. Bae, B. H. Hong, J.-H. Ahn, T.-W. Lee, *Nat. Photonics* 2012, *6*, 105–110.

[3] F. Wang, Z. Wang, Q. Wang, F. Wang, L. Yin, K. Xu, Y. Huang, J. He, *Nanotechnology* 2015, *26*, 292001.

[4] A. Gupta, T. Sakthivel, S. Seal, *Prog. Mater. Sci.* 2015, *73*, 44–126.

[5] K. S. Novoselov, A. K. Geim, S. V. Morozov, D. Jiang, Y. Zhang, S. V. Dubonos, I. V. Grigorieva, A. A. Firsov, *Science* 2004, *306*.

[6] Y. Gamo, A. Nagashima, M. Wakabayashi, M. Terai, C. Oshima, *Surf. Sci.* 1997, *374*, 61–64.

[7] K. S. Novoselov, Z. Jiang, Y. Zhang, S. V. Morozov, H. L. Stormer, U. Zeitler, J. C. Maan, G. S. Boebinger, P. Kim, A. K. Geim, *Science* 2007, *315*.

[8] X. Du, I. Skachko, F. Duerr, A. Luican, E. Y. Andrei, *Nature* 2009, *462*, 192–195.

[9] L. Liao, H. Peng, Z. Liu, *J. Am. Chem. Soc.* 2014, *136*, 12194–12200.

[10] R. Larciprete, S. Colonna, F. Ronci, R. Flammini, P. Lacovig, N. Apostol, A. Politano, P. Feulner, D. Menzel, S. Lizzit, *Nano Lett.* 2016, *16*, 1808–1817.

[11] C. Lee, X. Wei, J. W. Kysar, J. Hone, *Sci. Mag.* 2008, *321*, 385–388.

[12] K. Xue, Z. Xu, *Appl. Phys. Lett.* 2010, *96*, 63103.

[13] K. I. Bolotin, K. J. Sikes, Z. Jiang, M. Klima, G. Fudenberg, J. Hone, P. Kim, H. L. Stormer, *Solid State Commun.* 2008, *146*, 351–355.

[14] B. Chen, Q. Bi, J. Yang, Y. Xia, J. Hao, *Tribol. Int.* 2008, *41*, 1145–1152.

[15] J. Eichler, C. Lesniak, *J. Eur. Ceram. Soc.* 2008, *28*, 1105–1109.

[16] P. Karamanis, N. Otero, C. Pouchan, *J. Phys. Chem. C* 2015, *119*, 11872–11885.

[17] H. L. Zhuang, A. K. Singh, R. G. Hennig, *Phys. Rev. B* 2013, *87*, 165415.

[18] M. Ashton, J. Paul, S. B. Sinnott, R. G. Hennig, *Phys. Rev. Lett.* 2017, *118*, 106101.

[19] W. S. Hummers, R. E. Offeman, *J. Am. Chem. Soc.* 1958, *80*, 1339–1339.

[20] P. R. Wallace, *Phys. Rev.* 1947, *71*, 622–634.

[21] F. Schedin, A. K. Geim, S. V. Morozov, E. W. Hill, P. Blake, M. I. Katsnelson, K. S. Novoselov, *Nat. Mater.* 2007, *6*, 652–5.

[22] L. W. Drahushuk, M. S. Strano, *Langmuir* 2012, *28*, 16671–16678.

[23] Y. S. Dedkov, M. Fonin, U. Rüdiger, C. Laubschat, *Phys. Rev. Lett.* 2008, *100*, 107602.

[24] X. Wang, H. Dai, *Nat. Chem.* 2010, *2*, 661–665.

[25] M. Y. Han, B. Özyilmaz, Y. Zhang, P. Kim, *Phys. Rev. Lett.* 2007, *98*, 206805.

[26] A. W. Hauser, J. Schrier, P. Schwerdtfeger, *J. Phys. Chem. C* 2012, *116*, 10819–10827.

[27] J. Schrier, *J. Phys. Chem. Lett.* 2010, *1*, 2284–2287.

[28] J. S. Bunch, S. S. Verbridge, J. S. Alden, A. M. Van Der Zande, J. M. Parpia, H. G. Craighead, P. L. McEuen, *Nano Lett.* 2008, *8*, 2458–2462.

[29] J. M. Englert, K. C. Knirsch, C. Dotzer, B. Butz, F. Hauke, E. Spiecker, A. Hirsch, *Chem. Commun.* 2012, *48*, 5025.

[30] J. M. Englert, C. Dotzer, G. Yang, M. Schmid, C. Papp, J. M. Gottfried, H.-P. Steinrück, E. Spiecker, F. Hauke, A. Hirsch, *Nat. Chem.* 2011, *3*, 279–286.

[31] S. Eigler, M. Enzelberger-Heim, S. Grimm, P. Hofmann, W. Kroener, A. Geworski, C. Dotzer, M. Röckert, J. Xiao, C. Papp, O. Lytken, H.-P. Steinrück, P. Müller, A. Hirsch, *Adv. Mater.* 2013, *25*, 3583–3587.

[32] A. Dimiev, D. V. Kosynkin, L. B. Alemany, P. Chaguine, J. M. Tour, *J. Am. Chem. Soc.* 2012, *134*, 2815–2822.

[33] S. Eigler, A. Hirsch, *Angew. Chemie Int. Ed.* 2014, *53*, 7720–7738.

[34] D. Yu, Y. Yang, M. Durstock, J.-B. Baek, L. Dai, *ACS Nano* 2010, *4*, 5633–5640.

[35] H. Yang, C. Shan, F. Li, D. Han, Q. Zhang, L. Niu, *Chem. Commun.* 2009, *0*, 3880.

[36] H. Sun, Z. Xu, C. Gao, *Adv. Mater.* 2013, *25*, 2554–2560.

[37] J. R. Lomeda, C. D. Doyle, D. V. Kosynkin, W.-F. Hwang, J. M. Tour, *J. Am. Chem. Soc.* 2008, *130*, 16201–16206.

[38] H.-X. Wang, K.-G. Zhou, Y.-L. Xie, J. Zeng, N.-N. Chai, J. Li, H.-L. Zhang, *Chem. Commun.* 2011, *47*, 5747.

[39] Y. Lin, T. V. Williams, W. Cao, H. E. Elsayed-Ali, J. W. Connell, *J. Phys. Chem. C* 2010, *114*, 17434–17439.

[40] J. T. Robinson, J. S. Burgess, C. E. Junkermeier, S. C. Badescu, T. L. Reinecke, F. K. Perkins, M. K. Zalalutdniov, J. W. Baldwin, J. C. Culbertson, P. E. Sheehan, E. S. Snow, *Nano Lett.* 2010, *10*, 3001–3005.

[41] H. Yang, M. Chen, H. Zhou, C. Qiu, L. Hu, F. Yu, W. Chu, S. Sun, L. Sun, *J. Phys. Chem. C* 2011, *115*, 16844–16848.

[42] W. Zhao, J. Gebhardt, F. Späth, K. Gotterbarm, C. Gleichweit, H. P. Steinrück,

A. Görling, C. Papp, *Chem. - A Eur. J.* 2015, *21*, 3347–3358.

[43] D. C. Elias, R. R. Nair, T. M. G. Mohiuddin, S. V Morozov, P. Blake, M. P. Halsall, A. C. Ferrari, D. W. Boukhvalov, M. I. Katsnelson, A. K. Geim, K. S. Novoselov, *Science* 2009, *323*, 610–613.

[44] D. Haberer, D. V. Vyalikh, S. Taioli, B. Dora, M. Farjam, J. Fink, D. Marchenko, T. Pichler, K. Ziegler, S. Simonucci, M. S. Dresselhaus, M. Knupfer, B. Büchner, A. Grüneis, *Nano Lett.* 2010, *10*, 3360–3366.

[45] M. Z. Hossain, M. A. Walsh, M. C. Hersam, *J. Am. Chem. Soc.* 2010, *132*, 15399–15403.

[46] J. J. Navarro, F. Calleja, R. Miranda, E. M. Pérez, A. L. Vázquez de Parga, *Chem. Commun.* 2017, *53*, 10418–10421.

[47] J. J. Navarro, S. Leret, F. Calleja, D. Stradi, A. Black, R. Bernardo-Gavito, M. Garnica, D. Granados, A. L. Vázquez de Parga, E. M. Pérez, R. Miranda, *Nano Lett.* 2016, *16*, 355–361.

[48] R. A. Bueno, J. I. Martínez, R. F. Luccas, N. R. del Árbol, C. Munuera, I. Palacio, F. J. Palomares, K. Lauwaet, S. Thakur, J. M. Baranowski, W. Strupinski, M. F. López, F. Mompean, M. García-Hernández, J. A. Martín-Gago, *Nat. Commun.* 2017, *8*, 15306.

[49] M. Z. Hossain, M. B. A. Razak, H. Noritake, Y. Shiozawa, S. Yoshimoto, K. Mukai, T. Koitaya, J. Yoshinobu, S. Hosaka, *J. Phys. Chem. C* 2014, *118*, 22096–22101.

[50] W. Zhao, S. M. Kozlov, O. Höfert, K. Gotterbarm, M. P. A. Lorenz, F. Viñes, C. Papp, A. Görling, H. P. Steinrück, *J. Phys. Chem. Lett.* 2011, *2*, 759–764.

[51] G. B. Grad, P. Blaha, K. Schwarz, W. Auwärter, T. Greber, *Phys. Rev. B* 2003, *68*, 1–7.

[52] W. Auwärter, M. Muntwiler, J. Osterwalder, T. Greber, *Surf. Sci.* 2003, *545*, 735–740.

[53] K. Gotterbarm, F. Späth, U. Bauer, C. Bronnbauer, H. P. Steinrück, C. Papp, *ACS Catal.* 2015, *5*, 2397–2403.

[54] M. Hupalo, E. H. Conrad, M. C. Tringides, *Phys. Rev. B* 2009, *80*, 41401.

[55] A. Grüneis, K. Kummer, D. V. Vyalikh, *New J. Phys.* 2009, *11*, 73050.

[56] X. Li, W. Cai, L. Colombo, R. S. Ruoff, *Nano Lett.* 2009, *9*, 4268–4272.

[57] A. Dahal, M. Batzill, *Nanoscale* 2014, *6*, 2548.

[58] J. Wintterlin, M. L. Bocquet, *Surf. Sci.* 2009, *603*, 1841–1852.

[59] X. Li, W. Cai, L. Colombo, R. S. Ruoff, *Nano Lett.* 2009, *9*, 4268–4272.

[60] A. Varykhalov, J. Sánchez-Barriga, A. M. Shikin, C. Biswas, E. Vescovo, A. Rybkin, D. Marchenko, O. Rader, *Phys. Rev. Lett.* 2008, *101*, 157601.

[61] G. Bertoni, L. Calmels, A. Altibelli, V. Serin, *Phys. Rev. B* 2005, *71*, 75402.

[62] A. B. Preobrajenski, A. S. Vinogradov, N. Mårtensson, *Phys. Rev. B* 2004, *70*, 165404.

[63] J. Gebhardt, F. Viñes, A. Görling, *Phys. Rev. B* 2012, *86*, 195431.

[64] T. Balgar, H. Kim, E. Hasselbrink, *J. Phys. Chem. Lett.* 2013, *4*, 2094–2098.

[65] S. J. Altenburg, M. Lattelais, B. Wang, M. L. Bocquet, R. Berndt, *J. Am. Chem. Soc.* 2015, *137*, 9452–9458.

[66] N. A. Vinogradov, K. Schulte, M. L. Ng, A. Mikkelsen, E. Lundgren, Ma, A. B. Preobrajenski, *J. Phys. Chem. C* 2011, *115*, 9568–9577.

[67] D. Franz, S. Runte, C. Busse, S. Schumacher, T. Gerber, T. Michely, M. Mantilla, V. Kilic, J. Zegenhagen, A. Stierle, *Phys. Rev. Lett.* 2013, *110*, 65503.

[68] T. Brugger, S. Günther, B. Wang, J. H. Dil, M. L. Bocquet, J. Osterwalder, J. Wintterlin, T. Greber, *Phys. Rev. B* 2009, *79*, 45407.

[69] A. B. Preobrajenski, M. L. Ng, A. S. Vinogradov, N. Mårtensson, *Phys. Rev. B* 2008, *78*, 73401.

[70] M. Morscher, M. Corso, T. Greber, J. Osterwalder, *Surf. Sci.* 2006, *600*, 3280–3284.

[71] D. C. Elias, R. V Gorbachev, A. S. Mayorov, S. V Morozov, A. A. Zhukov, P. Blake, L. A. Ponomarenko, I. V Grigorieva, K. S. Novoselov, F. Guinea, A. K. Geim, *Nat. Phys.* 2011, *7*, 701–704.

[72] A. H. Castro Neto, F. Guinea, N. M. R. Peres, K. S. Novoselov, A. K. Geim, *Rev. Mod. Phys.* 2009, *81*, 109–162.

[73] A. S. Mayorov, R. V. Gorbachev, S. V. Morozov, L. Britnell, R. Jalil, L. A. Ponomarenko, P. Blake, K. S. Novoselov, K. Watanabe, T. Taniguchi, A. K. Geim, *Nano Lett.* 2011, *11*, 2396–2399.

[74] X. Du, I. Skachko, A. Barker, E. Y. Andrei, *Nat. Nanotechnol.* 2008, *3*, 491–495.

[75] F. Schwierz, *Nat. Publ. Gr* 2010, *5*, 487–496.

[76] A. Nagashima, N. Tejima, Y. Gamou, T. Kawai, C. Oshima, *Phys. Rev. B* 1995, *51*, 4606–4613.

[77] K. Watanabe, T. Taniguchi, H. Kanda, *Nat. Mater.* 2004, *3*, 404–409.

[78] G. Cassabois, P. Valvin, B. Gil, *Nat. Photonics* 2016, *10*, 262–266.

[79] M. Wei, Q. Fu, H. Wu, A. Dong, X. Bao, *Top. Catal.* 2016, *59*, 543–549.

[80] E. Grånäs, J. Knudsen, U. A. Schröder, T. Gerber, C. Busse, M. A. Arman, K. Schulte, J. N. Andersen, T. Michely, *ACS Nano* 2012, *6*, 9951–9963.

[81] Y. Dedkov, W. Klesse, A. Becker, F. Späth, C. Papp, E. Voloshina, *Carbon* 2017, *121*, 10–16.

[82] K. W. Kolasinski, *Surface Science: Foundations of Catalysis and Nanoscience*, Wiley, 2012.

[83] P. Willmott, *An Introduction to Synchrotron Radiation: Techniques and Applications*, Wiley, 2011.

[84] S. Suga, A. Sekiyama, *Photoelectron Spectroscopy*, Springer Berlin Heidelberg, Berlin, Heidelberg, 2014.

[85] “BESSY II Ring,” can be found under https://www.helmholtz-berlin.de/media/media/zentrum/grossgeraete/bessy/ring01_1.jpg, n.d.

[86] H. Hertz, *Ann. der Phys. und Chemie* 1887, *267*, 983–1000.

[87] T. L. Barr, *Modern ESCAThe Principles and Practice of X-Ray Photoelectron Spectroscopy*, Taylor & Francis, 1994.

[88] C. Papp, L. Plucinski, J. Minar, J. Braun, H. Ebert, C. M. Schneider, C. S. Fadley, *Phys. Rev. B* 2011, *84*, 45433.

[89] B. J. Bandy, D. R. Lloyd, N. V. Richardson, *Surf. Sci.* 1979, *89*, 344–353.

[90] M. P. Seah, W. A. Dench, *Surf. Interface Anal.* 1979, *1*, 2–11.

[91] D. Briggs, M. P. Seah, *Practical Surface Analysis, Auger and X-Ray Photoelectron Spectroscopy*, Wiley, 1990.

[92] S. Hüfner, *Photoelectron Spectroscopy: Principles and Applications*, Springer-Verlag Berlin Heidelberg, 1995.

[93] D. A. Shirley, *Phys. Rev. B* 1972, *5*, 4709–4714.

[94] S. Tougaard, *Surf. Interface Anal.* 1988, *11*, 453–472.

[95] J. Stöhr, *NEXAFS Spectroscopy*, Springer Berlin Heidelberg, 2013.

[96] D. A. Outka, J. Stöhr, W. Jark, P. Stevens, J. Solomon, R. J. Madix, *Phys. Rev. B* 1987, *35*, 4119–4122.

[97] D. Usachov, V. K. Adamchuk, D. Haberer, A. Grüneis, H. Sachdev, A. B. Preobrajenski, C. Laubschat, D. V. Vyalikh, *Phys. Rev. B* 2010, *82*, 75415.

[98] K. R. Koswattage, I. Shimoyama, Y. Baba, T. Sekiguchi, K. Nakagawa, *Appl. Surf. Sci.* 2011, *258*, 1561–1564.

[99] H. Schlichting, Methoden Und Mechanismen Der Thermischen Desorption, Technische Universität München, 1990.

[100] V. Rakić, L. Damjanović, 2013, pp. 131–174.

[101] P. A. Redhead, *Vacuum* 1962, *12*, 203–211.

[102] P. Feulner, D. Menzel, *J. Vac. Sci. Technol.* 1980, *17*, 662–663.

[103] M. Kinne, Kinetische Untersuchen von Oberflächen Mittels Hochaufgelöster Röntgen-Photoelektornenspektroskopie - Oxidation von CO Auf Pt(110) Und Zugehörige Elementarschritte, Friedrich Alexander Universität Erlangen-

Nürnberg, 2004.

[104] H. Pauly, *Atom, Molecule, and Cluster Beams I: Basic Theory, Production and Detection of Thermal Energy Beams*, Springer, 2000.

[105] S. DePaul, D. Pullman, B. Friedrich, *J. Phys. Chem.* 1993, *97*, 2167–2171.

[106] S. Kneitz, Adsorption- Und Streumessungen von CO an Ultradünnen Metallschichtsystemen Mittels Eines Überschalldüsen-Molekularstrahls, Julius-Maximilian-Universität Würzburg, 1998.

[107] G. Scoles, *Atomic and Molecular Beam Methods*, Oxford University Press, 1988.

[108] R. Denecke, M. Kinne, C. M. Whelan, H.-P. Steinrück, *Surf. Rev. Lett.* 2002, *9*, 797–801.

[109] F. Späth, W. Zhao, C. Gleichweit, K. Gotterbarm, U. Bauer, O. Höfert, H. P. Steinrück, C. Papp, *Surf. Sci.* 2015, *634*, 89–94.

[110] W. Zhao, O. Höfert, K. Gotterbarm, J. F. Zhu, C. Papp, H. P. Steinrück, *J. Phys. Chem. C* 2012, *116*, 5062–5066.

[111] A. K. Geim, *Science* 2009, *324*, 1530–1534.

[112] A. K. Geim, K. S. Novoselov, *Nat. Mater.* 2007, *6*, 183–191.

[113] P. E. Trevisanutto, C. Giorgetti, L. Reining, M. Ladisa, V. Olevano, *Phys. Rev. Lett.* 2008, *101*, 226405.

[114] P. Blake, P. D. Brimicombe, R. R. Nair, T. J. Booth, D. Jiang, F. Schedin, L. A. Ponomarenko, S. V. Morozov, H. F. Gleeson, E. W. Hill, A. K. Geim, K. S. Novoselov, *Nano Lett.* 2008, *8*, 1704–1708.

[115] L. Nilsson, M. Andersen, R. Balog, E. Lægsgaard, P. Hofmann, F. Besenbacher, B. Hammer, I. Stensgaard, L. Hornekær, *ACS Nano* 2012, *6*, 10258–10266.

[116] E. Sutter, P. Albrecht, F. E. Camino, P. Sutter, *Carbon* 2010, *48*, 4414–4420.

[117] H. Du, J. Li, J. Zhang, G. Su, X. Li, Y. Zhao, *J. Phys. Chem. C* 2011, *115*, 23261–23266.

[118] W. Yuan, G. Shi, *J. Mater. Chem. A* 2013, *1*, 10078.

[119] Z. M. Ao, Q. Jiang, R. Q. Zhang, T. T. Tan, S. Li, *J. Appl. Phys.* 2009, *105*, 74307.

[120] J. O. Sofo, A. S. Chaudhari, G. D. Barber, *Phys. Rev. B* 2007, *75*, 153401.

[121] Z. Luo, T. Yu, K. J. Kim, Z. Ni, Y. You, S. Lim, Z. Shen, S. Wang, J. Lin, *ACS Nano* 2009, *3*, 1781–1788.

[122] R. J. Koch, M. Weser, W. Zhao, F. Viñes, K. Gotterbarm, S. M. Kozlov, O. Höfert, M. Ostler, C. Papp, J. Gebhardt, H. P. Steinrück, A. Görling, T. Seyller, *Phys. Rev. B* 2012, *86*, 75401.

[123] Z. H. Sheng, L. Shao, J. J. Chen, W. J. Bao, F. Bin Wang, X. H. Xia, *ACS Nano*

2011, *5*, 4350–4358.

[124] H. M. Jeong, J. W. Lee, W. H. Shin, Y. J. Choi, H. J. Shin, J. K. Kang, J. W. Choi, *Nano Lett.* 2011, *11*, 2472–2477.

[125] A. L. M. Reddy, A. Srivastava, S. R. Gowda, H. Gullapalli, M. Dubey, P. M. Ajayan, *ACS Nano* 2010, *4*, 6337–6342.

[126] Y. Wang, Y. Shao, D. W. Matson, J. Li, Y. Lin, *ACS Nano* 2010, *4*, 1790–1798.

[127] L. Qu, Y. Liu, J. B. Baek, L. Dai, *ACS Nano* 2010, *4*, 1321–1326.

[128] D. Usachov, O. Vilkov, A. Grüneis, D. Haberer, A. Fedorov, V. K. Adamchuk, A. B. Preobrajenski, P. Dudin, A. Barinov, M. Oehzelt, C. Laubschat, D. V. Vyalikh, *Nano Lett.* 2011, *11*, 5401–5407.

[129] R. Balog, M. Andersen, B. Jørgensen, Z. Sljivancanin, B. Hammer, A. Baraldi, R. Larciprete, P. Hofmann, L. Hornekær, S. Lizzit, *ACS Nano* 2013, *7*, 3823–3832.

[130] K. Gotterbarm, W. Zhao, O. Höfert, C. Gleichweit, C. Papp, H.-P. Steinrück, *Phys. Chem. Chem. Phys.* 2013, *15*, 19625.

[131] N. P. Bellafont, D. R. Mañeru, F. Illas, *Carbon* 2014, *76*, 155–164.

[132] C. Papp, In-Situ Investigations of Adsorbed Hydrocarbons - Model Systems Od Heterogeneous Catalysis , Universität Erlangen-Nürnberg, 2007.

[133] C. Gleichweit, M. Amende, S. Schernich, W. Zhao, M. P. A. Lorenz, O. Höfert, N. Brückner, P. Wasserscheid, J. Libuda, H.-P. Steinrück, C. Papp, *ChemSusChem* 2013, *6*, 974–977.

[134] J. M. Gottfried, K. Flechtner, A. Kretschmann, T. Lukasczyk, H. P. Steinrück, *J. Am. Chem. Soc.* 2006, *128*, 5644–5645.

[135] C. Papp, H.-P. Steinrück, *Surf. Sci. Rep.* 2013, *68*, 446–487.

[136] Y. Yamada, J. Kim, S. Matsuo, S. Sato, *Carbon* 2014, *70*, 59–74.

[137] K. D. Rendulic, A. Winkler, H. P. Steinrück, *Surf. Sci.* 1987, *185*, 469–478.

[138] R. Balog, B. Jørgensen, J. Wells, E. Lægsgaard, P. Hofmann, F. Besenbacher, L. Hornekær, *J. Am. Chem. Soc.* 2009, *131*, 8744–8745.

[139] F. Späth, J. Gebhardt, F. Düll, U. Bauer, P. Bachmann, C. Gleichweit, A. Görling, H. P. Steinrück, C. Papp, *2D Mater.* 2017, *4*, 35026.

[140] L. Song, L. Ci, H. Lu, P. B. Sorokin, C. Jin, J. Ni, A. G. Kvashnin, D. G. Kvashnin, J. Lou, B. I. Yakobson, P. M. Ajayan, *Nano Lett.* 2010, *10*, 3209–3215.

[141] W. Auwärter, T. J. Kreutz, T. Greber, J. Osterwalder, *Surf. Sci.* 1999, *429*, 229–236.

[142] V. L. Solozhenko, A. G. Lazarenko, J. P. Petitet, A. V. Kanaev, *J. Phys. Chem. Solids* 2001, *62*, 1331–1334.

[143] L. Britnell, R. V. Gorbachev, R. Jalil, B. D. Belle, F. Schedin, A. Mishchenko, T.

Georgiou, M. I. Katsnelson, L. Eaves, S. V. Morozov, N. M. R. Peres, J. Leist, A. K. Geim, K. S. Novoselov, L. A. Ponomarenko, *Science* 2012, *335*, 947–950.

[144] S. J. Kang, G.-H. Lee, Y.-J. Yu, Y. Zhao, B. Kim, K. Watanabe, T. Taniguchi, J. Hone, P. Kim, C. Nuckolls, *Adv. Funct. Mater.* 2014, *24*, 5157–5163.

[145] Z. Liu, L. Song, S. Zhao, J. Huang, L. Ma, J. Zhang, J. Lou, P. M. Ajayan, *Nano Lett.* 2011, *11*, 2032–2037.

[146] Y. Lin, T. V. Williams, J. W. Connell, *J. Phys. Chem. Lett.* 2010, *1*, 277–283.

[147] X. Li, J. Yin, J. Zhou, W. Guo, *Nanotechnology* 2014, *25*, 105701.

[148] G. Mpourmpakis, G. E. Froudakis, *Catal. Today* 2007, *120*, 341–345.

[149] K. R. Koswattage, I. Shimoyama, Y. Baba, T. Sekiguchi, K. Nakagawa, *J. Chem. Phys.* 2011, *135*, 14706.

[150] M. Ohtomo, Y. Yamauchi, X. Sun, A. A. Kuzubov, N. S. Mikhaleva, P. V. Avramov, S. Entani, Y. Matsumoto, H. Naramoto, S. Sakai, *Nanoscale* 2017, *9*, 2369–2375.

[151] Y. Wang, *Phys. status solidi - Rapid Res. Lett.* 2010, *4*, 34–36.

[152] S. Tang, Z. Cao, *Chem. Phys. Lett.* 2010, *488*, 67–72.

[153] T. Brugger, H. Ma, M. Iannuzzi, S. Berner, A. Winkler, J. Hutter, J. Osterwalder, T. Greber, *Angew. Chemie Int. Ed.* 2010, *49*, 6120–6124.

[154] A. Bostwick, J. L. McChesney, K. V. Emtsev, T. Seyller, K. Horn, S. D. Kevan, E. Rotenberg, *Phys. Rev. Lett.* 2009, *103*, 56404.

[155] T. Ohta, *Science* 2006, *313*, 951–954.

[156] R. J. Koch, S. Fryska, M. Ostler, M. Endlich, F. Speck, T. Hänsel, J. A. Schaefer, T. Seyller, *Phys. Rev. Lett.* 2016, *116*, 106802.

[157] F. Speck, J. Jobst, F. Fromm, M. Ostler, D. Waldmann, M. Hundhausen, H. B. Weber, T. Seyller, *Appl. Phys. Lett.* 2011, *99*, 122106.

[158] M. L. Ng, R. Balog, L. Hornekær, A. B. Preobrajenski, N. A. Vinogradov, N. Mårtensson, K. Schulte, *J. Phys. Chem. C* 2010, *114*, 18559–18565.

[159] G. Kresse, J. Furthmüller, *Comput. Mater. Sci.* 1996, *6*, 15–50.

[160] P. E. Blöchl, *Phys. Rev. B* 1994, *50*, 17953–17979.

[161] J. P. Perdew, K. Burke, M. Ernzerhof, *Phys. Rev. Lett.* 1996, *77*, 3865–3868.

[162] S. Grimme, J. Antony, S. Ehrlich, H. Krieg, *J. Chem. Phys.* 2010, *132*, 154104.

[163] A. D. Becke, E. R. Johnson, *J. Chem. Phys.* 2005, *123*, 154101.

[164] H. J. Monkhorst, J. D. Pack, *Phys. Rev. B* 1976, *13*, 5188–5192.

[165] J. Neugebauer, M. Scheffler, *Phys. Rev. B* 1992, *46*, 16067–16080.

[166] M. Methfessel, A. T. Paxton, *Phys. Rev. B* 1989, *40*, 3616–3621.

[167] M. Fuentes-Cabrera, M. I. Baskes, A. V. Melechko, M. L. Simpson, *Phys. Rev. B* 2008, *77*, 35405.

[168] M. N. Huda, L. Kleinman, *Phys. Rev. B* 2006, *74*, 75418.

[169] R. Koitz, J. K. Nørskov, F. Studt, *Phys. Chem. Chem. Phys.* 2015, *17*, 12722–12727.

[170] M. Bokdam, G. Brocks, M. I. Katsnelson, P. J. Kelly, *Phys. Rev. B* 2014, *90*, 85415.

[171] X. Sun, A. Pratt, Z. Y. Li, M. Ohtomo, S. Sakai, Y. Yamauchi, *J. Appl. Phys.* 2014, *115*, 17C117.

[172] A. Lyalin, A. Nakayama, K. Uosaki, T. Taketsugu, *J. Phys. Chem. C* 2013, *117*, 21359–21370.

[173] N. Joshi, P. Ghosh, *Phys. Rev. B* 2013, *87*, 235440.

[174] L. Z. Zhang, Q. B. Yan, S. X. Du, G. Su, H. J. Gao, *J. Phys. Chem. C* 2012, *116*, 18202–18206.

[175] R. Laskowski, P. Blaha, K. Schwarz, *Phys. Rev. B* 2008, *78*, 45409.

[176] W. Zhao, J. Gebhardt, K. Gotterbarm, O. Höfert, C. Gleichweit, C. Papp, A. Görling, H.-P. Steinrück, *J. Phys. Condens. Matter* 2013, *25*, 445002.

[177] I. Shimoyama, Y. Baba, T. Sekiguchi, K. G. Nath, *J. Electron Spectros. Relat. Phenomena* 2004, *137–140*, 573–578.

[178] A. B. Preobrajenski, A. S. Vinogradov, N. Mårtensson, *Surf. Sci.* 2005, *582*, 21–30.

[179] R. Franke, S. Bender, J. Hormes, A. A. Pavlychev, N. G. Fominych, *Chem. Phys.* 1997, *216*, 243–257.

[180] L. Gao, Q. Fu, M. Wei, Y. Zhu, Q. Liu, E. Crumlin, Z. Liu, X. Bao, *ACS Catal.* 2016, *6*, 6814–6822.

[181] U. A. Schröder, M. Petrović, T. Gerber, A. J. Martínez-Galera, E. Grånäs, M. A. Arman, C. Herbig, J. Schnadt, M. Kralj, J. Knudsen, T. Michely, *2D Mater.* 2016, *4*, 15013.

[182] J. Gebhardt, R. J. Koch, W. Zhao, O. Höfert, K. Gotterbarm, S. Mammadov, C. Papp, A. Görling, H. P. Steinrück, T. Seyller, *Phys. Rev. B* 2013, *87*, 155437.

[183] S. P. Gao, *Solid State Commun.* 2012, *152*, 1817–1820.

[184] F. Greuter, I. Strathy, E. W. Plummer, W. Eberhardt, *Phys. Rev. B* 1986, *33*, 736–746.

[185] L. Jin, Q. Fu, R. Mu, D. Tan, X. Bao, *Phys. Chem. Chem. Phys.* 2011, *13*, 16655–16660.

[186] A. Winkler, K. D. Rendulic, *Surf. Sci.* 1982, *118*, 19–31.

[187] R. Mu, Q. Fu, L. Jin, L. Yu, G. Fang, D. Tan, X. Bao, *Angew. Chemie Int. Ed.* 2012, *51*, 4856–4859.

[188] L. Liu, Y. P. Feng, Z. X. Shen, *Phys. Rev. B* 2003, *68*, 104102.

[189] M. Petrović, I. Šrut Rakić, S. Runte, C. Busse, J. T. Sadowski, P. Lazić, I. Pletikosić, Z.-H. Pan, M. Milun, P. Pervan, N. Atodiresei, R. Brako, D. Šokčević, T. Valla, T. Michely, M. Kralj, *Nat. Commun.* 2013, *4*, 2772.

[190] L. Jin, Q. Fu, Y. Yang, X. Bao, *Surf. Sci.* 2013, *617*, 81–86.

[191] E. N. Voloshina, A. Generalov, M. Weser, S. Böttcher, K. Horn, Y. S. Dedkov, *New J. Phys.* 2011, *13*, 113028.

[192] C. Riedl, C. Coletti, T. Iwasaki, A. A. Zakharov, U. Starke, *Phys. Rev. Lett.* 2009, *103*, 246804.

[193] A. M. Shikin, G. V. Prudnikova, V. K. Adamchuk, F. Moresco, K. H. Rieder, *Phys. Rev. B* 2000, *62*, 13202–13208.

[194] B. Altintas, C. Parlak, C. Bozkurt, R. Eryiğit, *Eur. Phys. J. B* 2011, *79*, 301–312.

[195] E. Grånäs, T. Gerber, U. A. Schröder, K. Schulte, J. N. Andersen, T. Michely, J. Knudsen, *Surf. Sci.* 2016, *651*, 57–61.

[196] F. Späth, K. Gotterbarm, M. Amende, U. Bauer, C. Gleichweit, O. Höfert, H. P. Steinrück, C. Papp, *Surf. Sci.* 2016, *643*, 222–226.

[197] G. L. Doll, J. S. Speck, G. Dresselhaus, M. S. Dresselhaus, K. Nakamura, S. I. Tanuma, *J. Appl. Phys.* 1989, *66*, 2554–2558.

[198] A. Sumiyoshi, H. Hyodo, K. Kimura, *J. Phys. Chem. Solids* 2010, *71*, 569–571.

[199] A. Lyalin, A. Nakayama, K. Uosaki, T. Taketsugu, *Top. Catal.* 2014, *57*, 1032–1041.

[200] A. H. M. A. Wasey, G. P. Das, C. Majumder, *Chem. Phys. Lett.* 2017, *676*, 124–128.

[201] A. R. Kortan, R. L. Park, *Phys. Rev. B* 1981, *23*, 6340–6347.

[202] F. P. Netzer, T. E. Madey, *J. Chem. Phys.* 1982, *76*, 710–715.

[203] G. Henkelman, B. P. Uberuaga, H. Jónsson, *J. Chem. Phys.* 2000, *113*, 9901–9904.

[204] G. Henkelman, H. Jónsson, *J. Chem. Phys.* 1999, *111*, 7010–7022.

[205] K. A. Simonov, N. A. Vinogradov, M. L. Ng, A. S. Vinogradov, N. Mårtensson, A. B. Preobrajenski, *Surf. Sci.* 2012, *606*, 564–570.

[206] G. Henkelman, A. Arnaldsson, H. Jónsson, *Comput. Mater. Sci.* 2006, *36*, 354–360.

[207] K. Mao, X. Wu, J. Yang, *Phys. Chem. Chem. Phys.* 2017, *19*, 4435–4439.

[208] N. Ligato, L. S. Caputi, A. Cupolillo, *Carbon* 2016, *100*, 258–264.

[209] M. Schriver, W. Regan, W. J. Gannett, A. M. Zaniewski, M. F. Crommie, A. Zettl, *ACS Nano* 2013, *7*, 5763–5768.

[210] F. Zhou, Z. Li, G. J. Shenoy, L. Li, H. Liu, *ACS Nano* 2013, *7*, 6939–6947.

[211] M. Topsakal, H. Şahin, S. Ciraci, *Phys. Rev. B* 2012, *85*, 155445.

[212] P. A. Khomyakov, G. Giovannetti, P. C. Rusu, G. Brocks, J. van den Brink, P. J. Kelly, *Phys. Rev. B* 2009, *79*, 195425.

[213] A. Bozanic, M. Petravic, L.-J. Fan, Y.-W. Yang, Y. Chen, *Chem. Phys. Lett.* 2009, *472*, 190–193.

[214] R. Domnick, G. Held, H.-P. Steinrück, *Surf. Sci.* 2002, *516*, 95–102.

[215] F. Zhu, W. Chen, Y. Xu, C. Gao, D. Guan, C. Liu, D. Qian, S.-C. Zhang, J. Jia, *Nat. Mater.* 2015, *14*, 1020–1025.

[216] J. L. Zhang, S. Zhao, C. Han, Z. Wang, S. Zhong, S. Sun, R. Guo, X. Zhou, C. D. Gu, K. Di Yuan, Z. Li, W. Chen, *Nano Lett.* 2016, *16*, 4903–4908.

[217] L. Liu, Y. P. Feng, Z. X. Shen, *Phys. Rev. B* 2003, *68*, 104102.

[218] Z. Liu, Y. Gong, W. Zhou, L. Ma, J. Yu, J. C. Idrobo, J. Jung, A. H. MacDonald, R. Vajtai, J. Lou, P. M. Ajayan, *Nat. Commun.* 2013, *4*, 2541.

[219] L. H. Li, J. Cervenka, K. Watanabe, T. Taniguchi, Y. Chen, *ACS Nano* 2014, *8*, 1457–1462.

[220] A. Khataee, J. Azamat, F. Sadikoglu, *RSC Adv.* 2016, *6*, 94911–94920.

[221] M. Darvish Ganji, R. Dodangeh, *Phys. Chem. Chem. Phys.* 2017, *19*, 12032–12044.

[222] Y. Zhang, Q. Shi, Y. Liu, Y. Wang, Z. Meng, C. Xiao, K. Deng, D. Rao, R. Lu, *J. Phys. Chem. C* 2015, *119*, 19826–19831.

[223] Q. Fu, X. Bao, *Chem. Soc. Rev.* 2017, *46*, 1842–1874.

[224] G. Odahara, S. Otani, C. Oshima, M. Suzuki, T. Yasue, T. Koshikawa, *Surf. Sci.* 2011, *605*, 1095–1098.

[225] Y. Zhang, X. Weng, H. Li, H. Li, M. Wei, J. Xiao, Z. Liu, M. Chen, Q. Fu, X. Bao, *Nano Lett.* 2015, *15*, 3616–3623.

[226] Y. Yao, Q. Fu, Y. Y. Zhang, X. Weng, H. Li, M. Chen, L. Jin, A. Dong, R. Mu, P. Jiang, L. Liu, H. Bluhm, Z. Liu, S. B. Zhang, X. Bao, *Proc. Natl. Acad. Sci.* 2014, *111*, 17023–17028.

[227] K. Gotterbarm, F. Späth, U. Bauer, H.-P. Steinrück, C. Papp, *Top. Catal.* 2015, *58*, 573–579.

[228] Z. Zhou, F. Gao, D. W. Goodman, *Surf. Sci.* 2010, *604*, L31–L38.

[229] H. Dil, J. Lobo-Checa, R. Laskowski, P. Blaha, S. Berner, J. Osterwalder, T. Greber, *Science* 2008, *319*, 1824–1826.

[230] K. Mao, L. Li, W. Zhang, Y. Pei, X. C. Zeng, X. Wu, J. Yang, *Sci. Rep.* 2014, *4*, 1–7.

[231] P. Zhao, Y. Su, Y. Zhang, S. J. Li, G. Chen, *Chem. Phys. Lett.* 2011, *515*, 159–162.

[232] S. Sinthika, E. M. Kumar, R. Thapa, *J. Mater. Chem. A* 2014, *2*, 12812.

[233] C. Huang, X. Ye, C. Chen, S. Lin, D. Xie, *Comput. Theor. Chem.* 2013, *1011*, 5–10.

[234] Y. Zhang, M. Wei, Q. Fu, X. Bao, *Sci. Bull.* 2015, *60*, 1572–1579.

[235] F. Späth, F. Düll, J. Steinhauer, U. Bauer, P. Bachmann, H.-P. Steinrück, C. Papp, *To be Publ.* 2017.

[236] R. K. Paul, S. Badhulika, N. M. Saucedo, A. Mulchandani, *Anal. Chem.* 2012, *84*, 8171–8178.

[237] M. Shafiei, P. G. Spizzirri, R. Arsat, J. Yu, J. Du Plessis, S. Dubin, R. B. Kaner, K. Kalantar-Zadeh, W. Wlodarski, *J. Phys. Chem. C* 2010, *114*, 13796–13801.

[238] M. Sprinkle, D. Siegel, Y. Hu, J. Hicks, A. Tejeda, A. Taleb-Ibrahimi, P. Le Fèvre, F. Bertran, S. Vizzini, H. Enriquez, S. Chiang, P. Soukiassian, C. Berger, W. A. de Heer, A. Lanzara, E. H. Conrad, *Phys. Rev. Lett.* 2009, *103*, 226803.

[239] S. Reich, J. Maultzsch, C. Thomsen, P. Ordejón, *Phys. Rev. B* 2002, *66*, 35412.

[240] A. Bostwick, T. Ohta, T. Seyller, K. Horn, E. Rotenberg, *Nat. Phys.* 2006, *3*, 36–40.

[241] J. Lee, T. J. Ha, K. N. Parrish, S. F. Chowdhury, L. Tao, A. Dodabalapur, D. Akinwande, *IEEE Electron Device Lett.* 2013, *34*, 172–174.

[242] C. R. Dean, a F. Young, I. Meric, C. Lee, L. Wang, S. Sorgenfrei, K. Watanabe, T. Taniguchi, P. Kim, K. L. Shepard, J. Hone, *Nat. Nanotechnol.* 2010, *5*, 722–726.

[243] S. Watcharinyanon, C. Virojanadara, L. I. Johansson, *Surf. Sci.* 2011, *605*, 1918–1922.

[244] F. Oba, A. Togo, I. Tanaka, K. Watanabe, T. Taniguchi, *Phys. Rev. B* 2010, *81*, 75125.

[245] S. Okada, M. Otani, *Phys. Rev. B* 2010, *81*, 233401.

[246] M. Cattelan, B. Markman, G. Lucchini, P. K. Das, I. Vobornik, J. A. Robinson, S. Agnoli, G. Granozzi, *Chem. Mater.* 2015, *27*, 4105–4113.

[247] A. Castellanos-Gomez, M. Wojtaszek, Arramel, N. Tombros, B. J. Van Wees, *Small* 2012, *8*, 1607–1613.

[248] A. Pakdel, Y. Bando, D. Golberg, *Chem. Soc. Rev.* 2014, *43*, 934–959.

[249] S. Böttcher, M. Weser, Y. S. Dedkov, K. Horn, E. N. Voloshina, B. Paulus, *Nanoscale Res. Lett.* 2011, *6*, 214.

[250] S. Ryu, M. Y. Han, J. Maultzsch, T. F. Heinz, P. Kim, M. L. Steigerwald, L. E. Brus, *Nano Lett.* 2008, *8*, 4597–4602.

[251] Z. Wang, J. Wang, Z. Li, P. Gong, X. Liu, L. Zhang, J. Ren, H. Wang, S. Yang, *Carbon* 2012, *50*, 5403–5410.

[252] L. Gan, J. Zhou, F. Ke, H. Gu, D. Li, Z. Hu, Q. Sun, X. Guo, *NPG Asia Mater.* 2012, *4*, e31.

[253] D. Tristant, P. Puech, I. C. Gerber, *Phys. Chem. Chem. Phys.* 2015, *17*, 30045–30051.

[254] M. P. A. Lorenz, T. Fuhrmann, R. Streber, A. Bayer, F. Bebensee, K. Gotterbarm, M. Kinne, B. Tränkenschuh, J. F. Zhu, C. Papp, R. Denecke, H. P. Steinrück, *J. Chem. Phys.* 2010, *133*, 14706.

[255] Y. Zhang, L. Zhang, C. Zhou, *Acc. Chem. Res.* 2013, *46*, 2329–2339.

[256] R. J. Young, I. A. Kinloch, L. Gong, K. S. Novoselov, *Compos. Sci. Technol.* 2012, *72*, 1459–1476.

[257] K. S. Novoselov, V. I. Fal, L. Colombo, P. R. Gellert, M. G. Schwab, K. Kim, V. I. F. ko, L. Colombo, P. R. Gellert, M. G. Schwab, K. Kim, *Nature* 2013, *490*, 192–200.

[258] H. Tachikawa, T. Iyama, H. Kawabata, *Thin Solid Films* 2014, *554*, 199–203.

[259] D. E. Jiang, V. R. Cooper, S. Dai, *Nano Lett.* 2009, *9*, 4019–4024.

[260] S. Blankenburg, M. Bieri, R. Fasel, K. Müllen, C. A. Pignedoli, D. Passerone, *Small* 2010, *6*, 2266–2271.

[261] Y. Zhao, Y. Xie, Y. Y. Hui, L. Tang, W. Jie, Y. Jiang, L. Xu, S. P. Lau, Y. Chai, *J. Mater. Chem. C* 2013, *1*, 4956–4961.

[262] K. Celebi, J. Buchheim, R. M. Wyss, A. Droudian, P. Gasser, I. Shorubalko, J. Kye, C. Lee, H. G. Park, *Science* 2014, *344*, 289–293.

[263] Y. Tao, Q. Xue, Z. Liu, M. Shan, C. Ling, T. Wu, X. Li, *ACS Appl. Mater. Interfaces* 2014, *6*, 8048–8058.

[264] N. G. Boddeti, X. Liu, R. Long, J. Xiao, J. S. Bunch, M. L. Dunn, *Nano Lett.* 2013, *13*, 6216–6221.

[265] R. R. Nair, H. A. Wu, P. N. Jayaram, I. V. Grigorieva, A. K. Geim, *Science* 2012, *335*.

[266] N. T. Kirkland, T. Schiller, N. Medhekar, N. Birbilis, *Corros. Sci.* 2012, *56*, 1–4.

[267] P. Jacobson, B. Stöger, A. Garhofer, G. S. Parkinson, M. Schmid, R. Caudillo, F. Mittendorfer, J. Redinger, U. Diebold, *J. Phys. Chem. Lett.* 2012, *3*, 136–139.

[268] M. Weser, Y. Rehder, K. Horn, M. Sicot, M. Fonin, A. B. Preobrajenski, E. N. Voloshina, E. Goering, Y. S. Dedkov, *Appl. Phys. Lett.* 2010, *96*, 12504.

[269] D. Edwards, *J. Appl. Phys.* 1975, *46*, 1444–1447.

[270] P. Jakob, M. Gsell, D. Menzel, *J. Chem. Phys.* 2001, *114*, 10075–10085.

[271] L. Jin, Q. Fu, H. Zhang, R. Mu, Y. Zhang, D. Tan, X. Bao, *J. Phys. Chem. C* 2012, *116*, 2988–2993.

[272] M. Schmid, W. Hebenstreit, P. Varga, S. Crampin, *Phys. Rev. Lett.* 1996, *76*, 2298–2301.

[273] A. R. Lahrood, T. De Los Arcos, M. Prenzel, A. Von Keudell, J. Winter, *Thin Solid Films* 2011, *520*, 1625–1630.

[274] K. T. He, J. D. Wood, G. P. Doidge, E. Pop, J. W. Lyding, *Nano Lett.* 2012, *12*, 2665–2672.

[275] C. H. Y. Xuan Lim, A. Sorkin, Q. Bao, A. Li, K. Zhang, M. Nesladek, K. P. Loh, *Nat. Commun.* 2013, *4*, 1556–1558.

[276] J. Lu, A. H. C. Neto, K. P. Loh, *Nat. Commun.* 2012, *3*, 823.

[277] H. Cun, M. Iannuzzi, A. Hemmi, S. Roth, J. Osterwalder, T. Greber, *Nano Lett.* 2013, *13*, 2098–2103.

[278] P. Trischberger, H. Dröge, S. Gokhale, J. Henk, H.-P. Steinrück, W. Widdra, D. Menzel, *Surf. Sci.* 1997, *377–379*, 155–159.

[279] M. Weinelt, H.-P. Steinrück, Bandstruktur Und Elektronische Eigenschaften von Ausgewählten Adsorbatsystemen, Technische Universität München, 1994.

[280] C. R. Reid, I. P. O'Koye, K. M. Thomas, *Langmuir* 1998, *14*, 2415–2425.

13 Danksagung

Zuallererst möchte ich mich bei Herrn Prof. Dr. Steinrück bedanken. Zum einen, dass ich meine Dissertation an seinem Lehrstuhl anfertigen durfte und zum anderen für seine Geduld, seine stets hilfreichen Einfälle und seine pragmatischen Lösungen.

Als nächstes gebührt Herrn PD. Dr. Christian Papp vielen Dank. Er betreute die hier geleistete Arbeit zum einen mit viel Freiraum, aber zum anderen auch mit viel Unterstützung. Bei der Auswertung der Daten war er stets das erste Hindernis, welches es zu überwinden galt und überzeugt werden musste. Er brach vieles auf das Nötige herunter und lieferte wichtige Ideen zum richtigen Zeitpunkt.

Als nächstes gilt es Herrn Mathias Grabau zu Danken. Wenn auch in einem anderen Labor tätig, war er immer ein guter Ratgeber und ein wichtiger Diskussionspartner, der viel zur angenehmen Arbeitsatmosphäre beitrug.

Nun gilt es meinen nächsten Arbeitskollegen zu danken, die Mitstreiter im Alltag waren. Herr Dr. Oliver Höfert, Herr Dr. Christoph Gleichweit, Frau Dr. Karin Gotterbarm Herr Udo Bauer, Herr Philipp Bachmann und Herr Johann Steinhauer. Sie haben zum einen sehr zur guten Atmosphäre hier beigetragen, zum anderen haben sie auch die Messzeiten am Synchrotron erst möglich gemacht. Synchrotron ist Teamarbeit. Dies merkt man sehr deutlich in dieser Arbeitsgruppe. Ohne dieses Team wäre ich sicherlich nicht im Stande gewesen solch eine Menge an Messdaten zu erhalten. Hier gilt es auch nochmals Herrn PD. Dr. Papp zu danken, der die Anträge für die Messzeiten geschrieben hat und mir hier somit den Rücken frei hielt. Herrn Dr. Wei Zhao, da er mich hier einlernte und Herrn Fabian Düll für das Anfertigen seiner Masterarbeit sind hier noch im speziellen zu danken.

Auch ein Dank gilt denen Leuten, die nur kurz Unterstützung am Synchrotron leisten durften oder die ich nur kurz unterstützen durfte. Hier im speziellen Herr Dr. Roland Koch und Herr Christian Raidel, die mich ein wenig mit ARPES vertraut gemacht haben.

Weiterer Dank gilt natürlich den Leuten die Unterstützung leisten wenn etwas kaputt geht oder neues ausprobiert werden soll. Hier möchte ich Herrn Hans-Peter Bäumler für die Hilfe mit bei sämtlichen Problemen, die die Elektronik betrafen, danken. Im speziellen für das NEXAFS-Setup. Herrn Bernd Kreß für die Hilfe mit allen UHV Komponenten und der Werkstatt des Lehrstuhls für das Anfertigen neuer Teile und den ausgezeichnetem Rat, der immer eingeholt werden konnte. Hier ist im speziellen Herr Friedhold Wölfel zu nennen.
Letztlich muss ich auch noch allen Mitarbeitern des Lehrstuhls für die wunderbaren Jahre hier danken.

Ein persönlicher Dank gebührt meiner Familie und meinen Freunden für die Unterstützung während meiner, doch recht langen, Ausbildung.

Lebenslauf

Persönliche Angaben

Name	**Späth**
Vorname	**Florian**
Geburtsdatum	**14.07.1988**
Geburtsort	**Furth im Wald**
Nationalität	**Deutsch**
Familienstand	**Ledig**

Promotion

	Lehrstuhl für Physikalische Chemie II
1.1.2014-1.6.2018	**Universität Erlangen-Nürnberg**

Abschlüsse

11.2011	**Bachelor of Science**
10.2013	**Master of Science**
06.2008	**Abitur**

Studium

09.2008-10.2011	**Bachelor Studium an der Universität Erlangen-Nürnberg**
10.2011-10.2013	**Master Studium an der Universität Erlangen-Nürnberg**

Schule

1999-2008	**Benedikt-Stattler Gymnasium Bad Kötzting**
1995-1999	**Grundschule Bad Kötzting**